

Informazioni essenziali da indicare per la tesi, l'impostazione grafica è a discrezione.



UNIVERSITÀ
DEGLI STUDI
DI BRESCIA

DOTTORATO DI RICERCA IN TECHNOLOGY FOR HEALTH

FIS/01

XXXIV CICLO

EXTREME EVENTS IN QUADRATIC MEDIA: APPLICATION TO NONLINEAR IMAGING

JAUBERTEAU Raphaël

NOME DEL RELATORE

WABNITZ Stefan – Sapienza Università di Roma
COUDERC Vincent – Université de Limoges

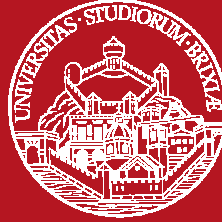
NOTE:

Le tesi devono riportare sul **frontespizio** il Settore Scientifico Disciplinare di appartenenza, come richiesto dal MIUR, Prot. 1581 del 26/07/2005.

In caso di più settori disciplinari interessati, deve essere indicato quello preminente nella trattazione della tesi. Elenco completo è reperibile al seguente indirizzo:

<http://attiministeriali.miur.it/UserFiles/115.htm>

Ph.D. Thesis



Université de Limoges

ED 610 - Sciences et Ingénierie des Systèmes, Mathématiques, Informatique (SISMI)

XLIM

Università degli studi di Brescia

Technology for Health

Dipartimento di Ingegneria dell' Informazione

To achieve the following titles:

Docteur de l'Université de Limoges

Electronique des Hautes Fréquences, Photonique et Systèmes

Dottore all'Università degli studi di Brescia

Technology for Health

Raphaël JAUBERTEAU

On December 14, 2021

Extreme events in quadratic media: application to nonlinear imaging

Thesis supervised by Vincent COUDERC and Stefan WABNITZ

President of jury

M. Christophe FINOT, professeur, ICB, Université de Bourgogne

Referees

M. Stefan TRILLO, professore ordinario, Dipartimento di Ingegneria, Università di Ferrara

M. Philippe GRELU, professeur, ICB, Université de Bourgogne

Examiners

M. Vincent COUDERC, directeur de recherche CNRS, XLIM, Université de Limoges

M. Stefan WABNITZ, professore ordinario, DIET, Sapienza università di Roma

M. Alejandro B. ACEVES, professor, Department of Mathematics, Southern Methodist University

M. Christophe FINOT, professeur, ICB, Université de Bourgogne

Invited

M. Alessandro TONELLO, maître de conférences, XLIM, Université de Limoges



This creation is available under a Creative Commons contract:
« Attribution-Non Commercial-No Derivatives 4.0 International »
online at <https://creativecommons.org/licenses/by-nc-nd/4.0/>



...,et si le souffle de Satan crée les tempêtes qui soulèvent tes eaux salées jusqu'aux nuages. Il faut que tu me le dises, parce que je me réjouirais de savoir l'enfer si près de l'homme.

Comte de Lautréamont



For my family, for my friends

Table of Contents

TABLE OF CONTENTS	5
LIST OF FIGURES	7
LIST OF TABLES	12
LIST OF ACRONYMS	13
GENERAL INTRODUCTION	14
BIBLIOGRAPHY – INTRODUCTION	18
CHAPTER I. SOLITONS IN OPTICS	19
I.1. HISTORY OF SOLITONS	19
<i>I.1.1. First observation in hydrodynamic systems</i>	19
<i>I.1.2. Solitons in optical systems</i>	20
I.1.2.1. The solitons, in all dimensions	20
I.1.2.2. Variety of the solitons	22
I.1.2.3. Some special soliton dynamics	28
I.2. NONLINEAR SCHRÖDINGER EQUATION	30
<i>I.2.1. From the Maxwell equations to the nonlinear Schrödinger equation</i>	30
<i>I.2.2. Introducing modulation instability in the nonlinear Schrödinger equation</i>	34
<i>I.2.3. Solitons generated by modulation instability</i>	35
I.2.3.1. Akhmediev breathers	35
I.2.3.2. Peregrine solitons	36
I.2.3.3. Kuznetsov-Ma breathers	37
I.3. SILICA FIBERS AS A PERFECT PHYSICAL ENVIRONMENT TO OBSERVE SOLITONS	39
<i>I.3.1. Linear effects in silica fiber</i>	40
I.3.1.1. Attenuation	40
I.3.1.2. Dispersion	41
<i>I.3.2. Nonlinear effects in silica fiber</i>	43
I.3.2.1. Raman effect	43
I.3.2.2. Kerr effect	44
CONCLUSION – CHAPTER I	45
BIBLIOGRAPHY – CHAPTER I	46
CHAPTER II. SOLITONS IN QUADRATIC MEDIA	52
II.1. LIGHT PROPAGATION AND THREE-WAVE MIXING IN QUADRATIC MEDIUM	52
II.2. IMPORTANCE OF THE PHASE MATCHING ON THE THREE-WAVE MIXING PROCESS	55
<i>II.2.1. Birefringence phase matching</i>	57
<i>II.2.2. Quasi-phase-matching</i>	59
II.3. SOLITONS GENERATION IN QUADRATIC MEDIA	61
<i>II.3.1. The history of quadratic solitons</i>	61
<i>II.3.2. The cascading effect</i>	63
<i>II.3.3. Modulation instability and non-zero background solitons in quadratic media</i>	65
<i>II.3.4. Walk-off compensation</i>	66
CONCLUSION – CHAPTER II	68
BIBLIOGRAPHY – CHAPTER II	69
CHAPTER III. QUADRATIC SPATIAL EXTREME EVENT	73

III.1. EXPERIMENTAL SETUP AND CRYSTAL PHASE MATCHING CONDITIONS	73
III.1.1. <i>Measurements setup</i>	73
III.1.2. <i>Crystal phase matching</i>	75
III.2. 2D SPATIAL EXTREME EVENT OBSERVATION IN KTP CRYSTAL	76
III.2.1. <i>Evolution of the self-trapped beam versus the input peak power: transient rogue dynamics</i>	79
III.2.2. <i>Evolution of the self-trapped beam versus the input polarization orientation</i>	82
III.2.3. <i>Evolution of the self-trapped beam versus the phase mismatch</i>	85
III.2.4. <i>Evolution of the output temporal profile of the self-trapped beam</i>	86
III.2.5. <i>Spectral broadening and distortion of the self-trapped beam spectrum</i>	90
III.3. DISCUSSION AND ANALYSIS ABOUT THE NONLINEAR DYNAMICS	92
III.4. SIMILARITY AND DIFFERENCES WITH RESPECT OF THE PEREGRINE SOLITON	95
III.5. 2D EXTREME EVENT IN PPLN CRYSTAL	97
CONCLUSION – CHAPTER III	100
BIBLIOGRAPHY – CHAPTER III	101
CHAPTER IV. ANALYSIS OF THE SPATIAL INSTABILITIES AT THE SECOND HARMONIC	103
IV.1. CONTEXT	103
IV.2. SETUP	103
IV.3. ANALYZE OF THE SPECKLE IN KTP CRYSTAL	103
IV.4. SPATIAL SPECKLE RESHAPING IN PPLN CRYSTAL	109
IV.5. DISCUSSION	112
CONCLUSION – CHAPTER IV	113
BIBLIOGRAPHY – CHAPTER IV	114
CHAPTER V. GENERATION OF MULTIPLE SPATIAL QUADRATIC SOLITONS	115
V.1. SPONTANEOUS EMISSION OF MULTIPLE QUADRATIC SOLITONS	115
V.2. APPEARANCE OF MULTIPLE QUADRATIC SOLITONS BY MEANS OF A SPATIALLY MODULATED INPUT BEAM	118
V.3. DISCUSSION	122
CONCLUSION – CHAPTER V	123
BIBLIOGRAPHY – CHAPTER V	124
CHAPTER VI. APPLICATIONS	125
VI.1. ULTRAFAST PULSE RESHAPING BY USING THE 2D TRANSIENT SOLITON	125
VI.1.1. <i>Emulation of the temporal filtering</i>	125
VI.1.2. <i>Pulse reshaping setup</i>	127
VI.1.3. <i>Pulse reshaping observations</i>	128
VI.2. PPLN GENERATED SUPERCONTINUUM FOR A DELAY LINE FREE M-CARS	130
VI.2.1. <i>Context</i>	130
VI.2.2. <i>Setup</i>	132
VI.2.3. <i>Delay line free M-CARS microscopy: experimental imaging</i>	134
VI.2.3.1. M-CARS image of polystyrene beads	134
VI.2.3.2. M-CARS image of cellulose fibers	134
CONCLUSION – CHAPTER VI	135
BIBLIOGRAPHY – CHAPTER VI	136
GENERAL CONCLUSION	138
PUBLICATIONS	140

List of Figures

Figure 1: The <i>solitary wave</i> re-created at the same place where JS Russell observed it in 1834. The picture was shot in 1995 and comes from: http://www.ma.hw.ac.uk/solitons/press.html	20
Figure 2: First temporal soliton recorded by Mollenauer <i>et al.</i> [9]. For various fiber input powers, the figure illustrates the spectrum and temporal traces of the output fiber beam (the temporal traces are from an autocorrelation and the curves are normalized). The box shows the input laser characteristics.....	21
Figure 3: Bright and dark solitons envelope, function of space (X) [18]. (a) -Bright soliton. (b) -Black dark soliton. (c) -Gray dark soliton.....	23
Figure 4: Experimental domain wall dark soliton [28].	24
Figure 5: Experimental photorefractive soliton formation in LiNbO ₃ material [42]. (a) -Input beam shape. (b-j) -Output beam shape at different light exposure times. A and C vectors are relative to the optical polarization field, while E ₀ vector is relative to the electrical field around the material. The light illumination remains constant during all the process time.....	26
Figure 6: Raman Stokes soliton generation in a fiber cavity [47].....	26
Figure 7: Numerical simulation of a supercontinuum generation in an optical fiber, due to N = 3 soliton fission [62]. Left -The resulting supercontinuum of light. Right -Time shift of the high-energy solitons while propagating in the fiber, after fission of the injected (Distance = 0) soliton.	29
Figure 8: MI evolution in a nonlinear medium [78].	34
Figure 9: Example of Akhmediev breather, for $a = 0.25$	36
Figure 10: Example of Peregrine soliton, for $a = 0.5$	37
Figure 11: Example of Kuznetsov-Ma breather, for $a = 0.95$	38
Figure 12: Simulated isolated spatial frequencies at the output face of a multimode fiber [88].....	40
Figure 13: Light attenuation in silica optical fiber, in function of the wavelength. This figure comes from Fibercore website.	41
Figure 14: Example of a microstructured hollow-core fiber, drawn by F. Delahaye at XLIM laboratory [93]. Left -Side cut of the fiber, Right -Zoom on the fiber core.	42
Figure 15: Raman Stokes and anti-Stokes energetic level. $h\nu_0$ is the incident photon energy, and $h\nu_{vib}$ the energy transmitted to the molecule.	43
Figure 16: Three-wave mixing process in a quadratic nonlinear medium with $\chi^{(2)}$ susceptibility.....	52
Figure 17: (a) -Second harmonic generation versus the nonlinear medium length and the phase mismatch between the waves involved in the process. (b) -Phase mismatch representation. Where \mathbf{k}_1 and \mathbf{k}_2 are the propagating vectors of the depleted waves, and \mathbf{k}_3 is the propagating vector of the generated wave.....	56
Figure 18: Waves polarization orientations for the two types of phase matching in birefringent crystals.....	57

Figure 19: (a) -Example of type I phase matching propagating waves. k_1 and k_2 are the propagating vectors of the incident waves, and k_3 is the propagating vector of the converted wave. (b) -Example of type II phase matching propagating waves. (c) -Normalized generated wave intensity along the birefringent crystal (type I and type II). Black curve is in the case of phase mismatch, and orange curve in the case of phase matching.	58
Figure 20: (a) -Poled crystal with $\Lambda = 2L_c$ period. (b) -Normalized intensity of the generated third wave along the crystal. Black curve is in the case of phase mismatch, and orange curve in the case of	60
Figure 21: Quadratic soliton observation made by Torruellas [28]. (a) -The input beam. (b) -The output beam at low input light intensity. (c) -The output beam at high input intensity (more than 10 GW/cm ²). All of these images are at the fundamental frequency.....	62
Figure 22: Quadratic soliton propagation in a KNbO ₃ crystal. The dashed lines are the simulation of the beam diffraction at low intensity [35] [36] [37].....	62
Figure 23: Two colors quadratic solitons, for weak Δk (left) and large Δk (right), from [43].	64
Figure 24: 2D MI observed by M. Delqué <i>et al.</i> [57]. (a) -Experimental results (10 MW peak power) and (b) -Corresponding spatial spectrum. (c) -Simulation (10 MW peak power) and (d) -Corresponding spatial spectrum.....	66
Figure 25: Soliton spatial switching obtained by Torruellas <i>et al.</i> [63]. They launched a 20 GW/cm ² pump into a 1 cm KTP crystal. The solid curve shows the output light transmission at the fundamental frequency through a 30 μ m aperture (numerical analysis), function of the imbalance between e and o crystal neutral axes. The dashed curve shows the output SH position.....	67
Figure 26: A quadratic spatial walking soliton by Torner <i>et al.</i> [40]. (a) -Without injection tilt. (b) -With injection tilt.	67
Figure 27: Schematic of the experimental setup for beam spatial studies.....	73
Figure 28: Phase matching curve for: (a) -KTP crystal within horizontal (θ) and vertical (Φ) axis orientation, (b) -PPLN, by modifying the crystal temperature.	76
Figure 29: Beams representation at the output face of the type II KTP crystal for a nonlinear propagation regime.....	77
Figure 30: Output spatial beam self-trapping in KTP, for an injected pump intensity of 0.5 GW/cm ² . (a) -3D view of FF beam, and transverse beam profile of the FF (red inset). (b) -2D representation of the FF and SH beams (SOP set close to 45°, $\Delta k = 0$). The round inset image has the same scale than the square image.....	78
Figure 31: Appearance and disappearance of the FF self-trapped beam versus the injected pump intensity. (a) -2D output beam evolution. (b) -Output profiles of the FF beam. (c) -Ratio of the local peak energy between the FF trapped beam and the remaining energy. Phase matching conditions, linear input SOP set close to 45°.	79
Figure 32: 2D representation of the SH beam evolution versus the input intensity. Phase matching conditions, linear input SOP set close to 45°. Images from (a) to (j) are for different input pump intensities.	80

Figure 33: FF wave section evolution in function of the input intensity I_0 . Simulation along a nonlinear material propagation of 30 mm. Works realized by Fabio Baronio from the University of Brescia (phase matching conditions).	81
Figure 34: Position of the self-trapped beam versus the linear input SOP (input pump intensity: 0.66 GW/cm ² and phase matching conditions). (a) -2D images of the output beam, for three different values of SOP.	83
Figure 35: Power ratio between the energy in the confined beam area and the total beam energy, versus the linear input SOP. The input pump intensity is 0.66 GW/cm ² . All these results have been obtained at phase matching conditions.	84
Figure 36: Polarization content of the self-trapped beam versus the linear input SOP. (a) -Schematic representation of the system used to realize the experiment; (b-d) -2D spatial output images for three different polarization states and for both FF (top) and SH (bottom) beams (Intensity: 0.66 GW/cm ² , phase matching conditions).	85
Figure 37: Output images of the FF beam versus the vertical angle $\Delta\Phi$ of the KTP crystal. (top) -SHG curve versus vertical crystal angle of the KTP, (bottom) -2D output spatial image of the beam at the end face of the crystal (input pump intensity = 0.3 GW/cm ² , linear input SOP set close to 45°).	86
Figure 38: Experimental results of the spatial trapping influence on the temporal domain. Autocorrelation traces of the trapped beam versus the input intensity for $\Delta kL = 0$ (phase matching) 88	88
Figure 39: Experimental results of the spatial trapping impact on the temporal domain. Autocorrelation traces of the trapped beam versus the input intensity for $\Delta kL = 5\pi$ and a linear input SOP = 63°.	89
Figure 40: Experimental results of the spatial trapping impact on the temporal domain. Autocorrelation traces of the trapped beam versus the input intensity for $\Delta kL = -9\pi$ and a linear input SOP = 63°.	90
Figure 41: Output spectrum of the trapped beam versus the pump intensity, for a linear input SOP of 69°. (a) - $\Delta kL = 0$. (b) - $\Delta kL = 9\pi$. (c) - $\Delta kL = -9\pi$	91
Figure 42: Spatial evolution of the SH beam versus the input intensity. The vertical axis reports the elementary spot diameter constituting it ($\Delta kL = 2\pi$ and linear input SOP $\sim 45^\circ$).	94
Figure 43: (a) -Temporal Peregrine soliton observation by Kibler <i>et al.</i> [15] in optical fibers. (b) -My observation of the spatial FF soliton. (c) -My observation of the SH trapped beam. In both (b) and (c) , the round insets are the images of the corresponding beams, out of the KTP, and the dashed line in those insets shows the sense of cut for the profile plotting. Phase matching conditions, linear input SOP = 53° and input pump intensity = 0.3 GW/cm ²	96
Figure 44: Left -Schematic of a PPLN crystal. Right -Spatial output soliton after propagation in the PPLN, excited by a collimated beam (positive phase mismatch i. e. crystal temperature = 21.5 °C), and input pump intensity = 0.85 GW/cm ²). The linear input SOP is set parallel to the crystal extraordinary axis. The round inset image has the same scale than the square image.	97
Figure 45: (a) -2D output beam images of the FF and SH beams at the end face of the PPLN versus the input pump intensity (the round inset images have the same scale than the square images). (b) -1D	

output profiles evolution of the FF beams versus the input pump intensity. The linear input SOP is set parallel to the crystal extraordinary axis. Positive phase mismatch configuration (21.5 °C). 99

Figure 46: Image of the SH beam, after propagation in the KTP, versus the FF pump intensity. $\Delta k_L = 2\pi$ and linear input SOP of 47° 104

Figure 47: SH beams intensity levels, PDFs, obtained in KTP crystal at different input pump intensities. On those histograms, I normalized the intensity axis of the beams at the SH, according to the maximum allowed level of the 8-bit camera device (I_{SHG} / I_N). I avoided camera saturation by reducing the crystal output light intensity with a variable attenuator. For each value of pump intensity **(a-d)**, the attenuation was modified in front of the camera. $\Delta k_L = 2\pi$, input linear SOP = 47° 106

Figure 48: SH beam intensity level (average data of a set of 10000 laser shot), PDF, obtained in KTP crystal for a pump intensity of 3.6 GW/cm^2 . On the histogram, I normalized the intensity axis of the average data beam at the SH frequency, according to the maximum allowed level of the 8-bit camera device. I avoided camera saturation by reducing crystal output light intensity with variable attenuator. Due to the important light density between the spots, a background compensation was used for PDF calculation. The linear input SOP remains unchanged, $\Delta k_L = 3\pi$ 107

Figure 49: **(a)**-Intensity correlations C_i of the near-field SH images. **(b)**-Comparison of each intensity correlation spatial profiles, cut on x or on y transverse axes. $\Delta k_L = 2\pi$ and linear input SOP of 47° . 108

Figure 50: **(a)**-Near-field images of the PPLN output SH beam, for different values of pump intensity. Near and far fields of the SH for **(b)**-Pump intensity = 2.6 GW/cm^2 , **(c)**-Pump intensity = 51 GW/cm^2 . Such experimental results are at the phase matching conditions. The linear input SOP is set parallel to the crystal extraordinary axis. 109

Figure 51: **(a-d)**-SH beams spectral evolution, for different pump intensity values. **(e)**-SH beam spectrum for an input pump intensity of 51 GW/cm^2 and corresponding beam images. Both insets are the far-field beam images at 500 nm **(left)** and 550 nm **(right)**, respectively. Such experimental results are at the phase matching conditions. The linear input SOP is set parallel to the crystal extraordinary axis. 110

Figure 52: Spectral broadening evolution versus pump intensity, around the FF. Such experimental results are at the phase matching conditions. The linear input SOP is set parallel to the crystal extraordinary axis. 110

Figure 53: Numerical simulation of the spectral evolution along the propagation length of a PPLN crystal. L and R are respectively the anti-Stokes and the Stokes waves. Phase mismatch conditions ($\Delta k_L = -3\pi$), and pump intensity = 1 GW/cm^2 . This figure is extracted from Ref [10]. 111

Figure 54: Beam spectral evolution, function of crystal temperature i. e. Δk_L . The pump intensity is of 24.4 GW/cm^2 . The linear input SOP is set parallel to the crystal extraordinary axis. 111

Figure 55: Profile of the output FF and SH beams versus the phase mismatch and for an input linear SOP of 47° and an input pump intensity of 0.05 GW/cm^2 . **(a)**- $\Delta\Phi = -1.67^\circ$ ($\Delta k_L = -9\pi$); **(b)**- $\Delta\Phi = -0.33^\circ$, ($\Delta k_L = -2\pi$); **(c)**- $\Delta\Phi = 0^\circ$ ($\Delta k_L = 0$); **(d)**- $\Delta\Phi = 0.33^\circ$, ($\Delta k_L = 2\pi$); **(e)**- $\Delta\Phi = 1.67^\circ$ ($\Delta k_L = 9\pi$); **(f)**-Normalized SHG curve versus $\Delta\theta$; **(g)**-Normalized SHG curve versus $\Delta\Phi$ 116

Figure 56: Multiple quadratic solitons observation. Images of the output FF and SH beams for three different input intensities, $\Delta k_L = 9\pi$, input linear SOP at 47° . **(a)**-Evolution of the pump intensity from 0.1 to 0.66 GW/cm^2 . **(b)**-Pump intensity = 1.1 GW/cm^2 117

Figure 57: (a) -S. Carrasco experimental observations [3] at the output face of a bulk crystal (spatial 2D transverse material - 1064 nm). The input peak intensity is 23 GW/cm ² (b) -S. Carrasco SH profiles simulations [3].	118
Figure 58: (a) -Experimental setup used to convert one beam in two with perpendicular polarization directions. (b) -Two different excitations of the crystal leading to spatial interferences and no interferences. (c) -Images of the output pattern for different linear input SOP orientation. Phase matching conditions and input pump intensity = 0.01 GW/cm ² .	119
Figure 59: Soliton on a modulated pump. The FF and SH beams images are for an input pump intensity of 0.66 GW/cm ² . Phase matching conditions and linear input SOP = 45°.	120
Figure 60: Solitons evolution, on a modulated pump, function of the pump intensity. (a) -FF beams images. (b) - Output profiles of the FF beam (I cut the lobe with the highest contrast between the pump and the soliton, see round inset). Phase matching conditions and linear input SOP = 59°.	121
Figure 61: Solitons at the SH for a pump intensity of 0.53 GW/cm ² . (a) -Phase matching and linear input SOP = 45°. (b) -Phase matching and linear input SOP = 59°. (c) -High positive phase mismatch and linear input SOP = 59°.	122
Figure 62: (a) -Nonlinear transmission curve obtained by filtering the self-trapped beam with a hole of 40 μm of diameter. (b) -(Left curve) temporal pulse profiles before and after the temporal filtering; (Right curve) corresponding autocorrelation traces of the two pulses. The figures are obtained at phase matching conditions, with a linear input SOP of 47°.	126
Figure 63: Experimental module used to shape the incident pulse.	127
Figure 64: Pulse reshaping observation, by spatially filtering the soliton with a hole (diameter at 1/e ² = 80 μm). Calculated pulse profiles from the recorded autocorrelation traces. The pump intensity is equal to 0.7 GW/cm ² , the linear input SOP is 53° and the crystal is at phase matching conditions.	128
Figure 65: Analyze of the pulse reshaping effect for different input pump intensities and phase mismatch conditions. The input linear SOP is 53°. Black curves: input pulses, Red curves: output pulses. (a) -Pulse reshaping evolution, versus the pump intensity and at phase matching conditions. (b) -Pulse reshaping evolution, versus the phase mismatch ($\Delta kL = +9\pi$ and $\Delta kL = -9\pi$) or phase matching conditions ($\Delta kL = 0$) for an input pump intensity of 0.7 GW/cm ² .	129
Figure 66: M-CARS experimental setup, with a PPLN and without delay line, realized by S. Wehbi <i>et al.</i> at XLIM laboratory [19]. $\lambda/2$: half-wave plate, BS : polarizing beam splitter, L : lens, M : mirror, SP1000 : short-pass filter (<1000 nm), LP1000 : long-pass filter (>1000 nm).	132
Figure 67: Spectrum of the Stokes beam (PPLN supercontinuum + long-pass filter at 1000 nm) before injection in the sample.	133
Figure 68: M-CARS images of polystyrene beads by S. Wehbi <i>et al.</i> [19]. (a) -Bright field image. (b) -M-CARS image for a Raman shift of 3055 cm ⁻¹ , extracted of M-CARS data.	134
Figure 69: M-CARS images of cellulose fibers by S. Wehbi <i>et al.</i> [19]. (a) -Bright field image. (b) -M-CARS image for a Raman shift of 2896 cm ⁻¹ , extracted of M-CARS data.	134

List of Tables

Table 1: Quadratic nonlinear processes.....	53
---	----

List of Acronyms

MI	Modulation Instability
NLSE	Nonlinear Schrödinger Equation
CARS	Coherent Anti-Stokes Raman Scattering
M-CARS	Multiplex Coherent Anti-Stokes Raman Scattering
NIR	Near Infrared
ZDW	Zero Dispersion Wavelength
SHG	Second Harmonic Generation
FF	Fundamental Frequency
SH	Second Harmonic
SOP	State Of Polarization
FWHMI	Full Width Half Maximum in Intensity
PDF	Probability Density Function
PCF	Photonic Crystal Fiber

General Introduction

For years, humankind has sought with interest to understand the world around it. Phenomena that could not be explained in the past, due to limitations of scientific knowledge, were generally attributed to mystical or divine manifestations. This is notably the case of so-called "extreme" phenomena such as, for example, the appearance of volcanic eruptions, earthquakes, eclipses, tornadoes, hurricanes or giant waves on the surface of the oceans.

In each civilization, we find a deity whose irascibility is generally associated with the formation of such phenomena. For example, in Mesoamerica, Tlaloc was the God responsible of tropical cyclones, common extreme phenomena in this part of the world [1]. Mariners had their own myths, even if not related to specific religions, around these terrible waves named *rogue waves*, appearing and disappearing suddenly, far from the coast [2].

Many of these events have attracted the attention of scientists for more than 2000 years in order to rationally explain the appearance of such events, and it is worth noting that historically, optics has been at the center of the concerns of intellectuals and researchers.

Nowadays, the majority of these extreme phenomena can be studied with a scientific approach. The predictability of many extreme phenomena in nature are subject to the knowledge of the mechanisms, as well as of the initial conditions leading to their formation (tropical cyclones can be anticipated by meteorological analysis). Moreover, the nature that surrounds us is still intrinsically unstable and in perpetual mutation. Also, such manifestations mix periodic and chaotic dynamics: In particular, in chaos dynamics, small incertitude in the initial conditions may cause drastic differences. Any long-term prediction would require then the knowledge of all the initial conditions with a precision well above the reasonable values obtained from experimental measurements.

In optics, many advances have been made over the last century, both from a theoretical and technological point of view. It is now the 61th anniversary of the invention of the laser by Theodore H. Maiman [3], which in the 1960s brought a new wind to fundamental optics research, but also gave rise to numerous inventions that are now used on a daily basis. Indeed, the use of the laser as a stable and coherent optical source permitted the study of the linear and nonlinear interaction between light and matter.

In the last few years, nonlinear Modulation Instability (MI) in optics has become an interesting field of study. Since the early studies on MI in optics, it was pointed out the intriguing links with many other physical systems such as deep-water hydrodynamics. More recently, MI has also been studied as a nonlinear mechanism at the origin of extreme events.

In some nonlinear systems, continuous wave may be unstable upon certain modulation frequencies. It leads to the exponential growth of sidebands in frequency domain and can cause the wave to break into a train of pulses. Rogue waves, which are strong spatial phenomena with very short lifetime and a very high and destructive energy, are likely to appear on MI [2] [4].

Studies on mathematical waveforms such as Akhmediev breathers, Kuznetsov-Ma breathers and Peregrine solitons have flourished in the last years, to understand the formation and propagation of the rogue waves [5] [6] [7]. Those mathematical waveforms are results of differential equations used to describe natural phenomena, and the most used of those equations is the NonLinear Schrödinger Equation (NLSE). However, exact solutions can be found out of this equation only for some specific conditions. The NLSE solutions are well known for a propagation in a nonlinear medium with one transverse spatial dimension or in temporal domain (1D), in presence of constant group velocity dispersion. When there are two transverse spatial dimensions (2D), the mathematical study of the 2D-NLSE is significantly more complicated. However, this fact does not necessarily mean that ephemeral waves of extreme amplitude do not exist in 2D. It is then probably necessary to find another way to solve the differential equations, by using for example realistic approximations. It is also interesting to underline that the term soliton is given to a solution of a nonlinear propagation equation. If we strictly follow this definition, no 2D soliton may exist because of the non-integrability of the nonlinear equation from a mathematical point of view. In the present manuscript, the term soliton will be not restricted to a rigorous solution of an integrable system.

The first soliton propagation was observed more than one hundred and fifty years ago by John Scott Russell in a water channel. In optics, solitons were first studied in centrosymmetric media with cubic nonlinearity [8]. It was not until 1974 to see the first theoretical prediction of solitons in media with quadratic nonlinearity [9]. The experimental observation of a quadratic soliton dates back to the end of the last century (more precisely in 1995 [10]). Also,

the existence of purely 2D MI has been experimentally proven in materials with quadratic nonlinearity in 2011 [11].

My thesis deals with the study of self-trapped extreme events in quadratic media, which have the potentiality to appear and disappear with respect to the propagation conditions or by self-destruction of their own environment.

Chapter I will list the most salient types of solitons reported in optical systems. I will recall some basics of nonlinear optics and how one can reach solitonic solutions, starting from an analytic study, from Maxwell equations to the particular solution of solitons on MI: the Akhmediev breathers, the Kuznetsov-Ma breathers and the Peregrine solitons. By the end of the chapter, I will focus on a particular optical system: the silica fiber. Indeed, these waveguides have been historically the preferred choice of experiments with optical solitons.

Chapter II will describe the nonlinear mechanisms in quadratic crystals, which are a different type of optical system. Supported by the analysis made on the first chapter, this chapter will focus on the history of bicolor solitons, analytic solitonic results developed for quadratic systems, as well as on MI observation in quadratic crystals.

On **chapter III**, I will illustrate my results on spatial, temporal and spectral studies of a new type of spatial self-trapped beam, generated through the propagation of an infrared collimated pump beam in nonlinear crystals. In such materials, a part of the optical beam experienced a highly self-focusing effect. Moreover, such focused energy remained confined along the crystal length but surprisingly disappeared when the input power was increased further.

In order to have a better knowledge of the causes of the spatial soliton disappearance, a complete analysis of the speckled pattern at the second harmonic, generated in parallel to the disappearance of the self-confined event, will be discussed on **chapter IV**. In the same chapter,

I will show a reorganization of this speckled beam at high light intensities, and the corresponding impressive spectrum broadening generated during such reorganization.

Chapter V will report on particular cases of spatial multi-solitons generation in quadratic crystal. Such events were initiated in two ways: either spontaneously, or by means of a periodical input pump, generated by interferences. As for the case of single self-trapped event seen on **chapter III**, the extreme events observed on **chapter V** disappeared when increasing further the pump power.

In **chapter VI**, I will conclude this thesis by showing an application of ultrafast temporal pulse reshaping, using such newly discovered soliton. The pulse reshaping was obtained by spatially filtering the quadratic soliton from the input pump, and was annihilated at high power, as the soliton disappeared.

In order to demonstrate the applicability of the multicolor beams at the output of a quadratic crystal, in a biomedical imaging system, I collaborated with Sahar Wehbi to realize a first demonstration of Multiplex Coherent Anti-Stokes Raman Scattering (M-CARS) images. In particular, again in **chapter VI**, I will show our results of M-CARS images, obtained in the context of S. Wehbi thesis, using a supercontinuum generated in the quadratic crystal as a broadband Stokes wave. The synchronism between pump and such supercontinuum permitted to create a vibrational spectromicroscopy system in absence of delay lines.

Bibliography – Introduction

- [1] Klein, C. F. (1980). Who Was Tlaloc (A God of Rain, Lightning, and Storms). *Journal of Latin American Lore*, 6(2), 155-204.
- [2] Müller, P., Garrett, C., & Osborne, A. (2005). Rogue waves. *Oceanography*, 18(3), 66.
- [3] Maiman, T. H. (1960). Stimulated optical radiation in ruby.
- [4] Solli, D. R., Ropers, C., Koonath, P., & Jalali, B. (2007). Optical rogue waves. *Nature*, 450(7172), 1054-1057.
- [5] Kuznetsov, E. A. (1977). Solitons in a parametrically unstable plasma. *DoSSR*, 236, 575-577.
- [6] Ma, Y. C. (1979). The perturbed plane-wave solutions of the cubic Schrödinger equation. *Studies in Applied Mathematics*, 60(1), 43-58.
- [7] Peregrine, D. H. (1983). Water waves, nonlinear Schrödinger equations and their solutions. *The ANZIAM Journal*, 25(1), 16-43.
- [8] McCall, S. L., & Hahn, E. L. (1967). Self-induced transparency by pulsed coherent light. *Physical Review Letters*, 18(21), 908.
- [9] Karamzin, Y. N., & Sukhorukov, A. P. (1974). Nonlinear interaction of diffracted light beams in a medium with quadratic nonlinearity: mutual focusing of beams and limitation on the efficiency of optical frequency converters. *ZhETF Pisma Redaktsiiu*, 20, 734.
- [10] Torruellas, W. E., Wang, Z., Hagan, D. J., VanStryland, E. W., Stegeman, G. I., Torner, L., & Menyuk, C. R. (1995). Observation of two-dimensional spatial solitary waves in a quadratic medium. *Physical review letters*, 74(25), 5036.
- [11] Delqué, M., Fanjoux, G., Gorza, S. P., & Haelterman, M. (2011). Spontaneous 2D modulation instability in second harmonic generation process. *Optics Communications*, 284(5), 1401-1404.

Chapter I. Solitons in optics

I.1. History of solitons

Solitons are self-sustained waves, propagating without any deformation, through a nonlinear medium, whether in spatial, temporal, or spectral domains. For example, temporal solitons are created through the equilibrium of dispersion and nonlinearities of the medium. Since solitons are wave packets propagating like a particle, without losing its shape, they are popular in quantum physics for wave/particle studies [1]. The first soliton ever observed was in hydrodynamics.

I.1.1. First observation in hydrodynamic systems

The first solitary wave ever observed was created by the motion of a boat. This wave was propagating through 1 or 2 km along a channel without loss or deformation. Scott Russel discovered this singular wave in 1834 and reported the phenomenon as a *wave of translation* and then *solitary wave* [2].

“I was observing the motion of a boat which was rapidly drawn along a narrow channel by a pair of horses, when the boat suddenly stopped—not so the mass of water in the channel which it had put in motion; it accumulated round the prow of the vessel in a state of violent agitation, then suddenly leaving it behind, rolled forward with great velocity, assuming the form of a large solitary elevation, a rounded, smooth and well-defined heap of water, which continued its course along the channel apparently without change of form or diminution of speed. I followed it on horseback, and overtook it still rolling on at a rate of some eight or nine miles an hour [14 km/h], preserving its original figure some thirty feet [9 m] long and a foot to a foot and a half [30–45 cm] in height. Its height gradually diminished, and after a chase of one or two miles [2–3 km] I lost it in the windings of the channel. Such, in the month of August 1834, was my first chance interview with that singular and beautiful phenomenon which I have called the Wave of Translation.”

J.S. Russel



Figure 1: The *solitary wave* re-created at the same place where JS Russell observed it in 1834. The picture was shot in 1995 and comes from: <http://www.ma.hw.ac.uk/solitons/press.html>.

A first theoretical explanation of such phenomenon was brought by Joseph Boussinesq [3] and Lord Rayleigh [4] in the 1870s. In 1895, Diederik Korteweg and Gustav de Vries provided the first equation giving solitary waves similar solutions [5].

Nowadays, scientists experimentally observe solitons in many fields of physics and in a lot of different propagation media. The most famous ones are wave tanks in hydrodynamics or fibers in optics.

I.1.2. Solitons in optical systems

I.1.2.1. The solitons, in all dimensions

One has to wait the invention of laser emission in 1960 [6] in order to observe solitons in optical medium, since only lasers can provide an optical power large enough to induce a nonlinear response for the light propagation. Optical solitons have been observed in temporal, spatial or spectral domains.

Temporal solitons:

The first optical temporal soliton was experimentally studied by McCall *et al.* in a nonlinear medium with self-transparency induced by the laser beam in 1967 [7]. In that publication, the phenomenon was interpreted as a "hole-burning" effect in which the absorption line is simply saturated by the leading edge of the pulse.

Six years later, a theoretical work led by Akira Hasegawa and Fred Tappert of Bell labs [8] showed that some optical pulses were able to propagate with a constant envelope along an optical fiber in anomalous regime. Later, a first soliton observation in optical fiber was reported in 1980 by Mollenauer *et al.* [9].

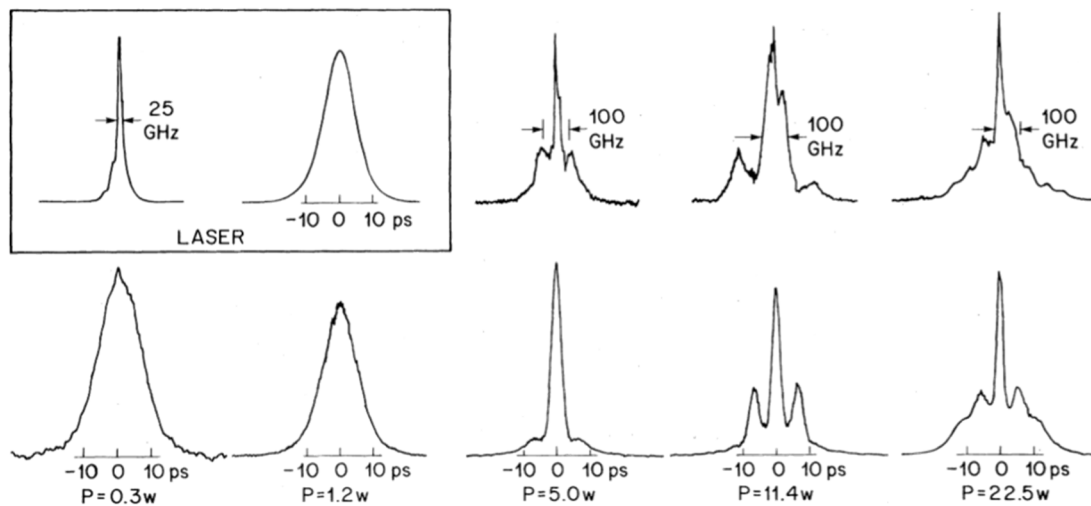


Figure 2: First temporal soliton recorded by Mollenauer *et al.* [9]. For various fiber input powers, the figure illustrates the spectrum and temporal traces of the output fiber beam (the temporal traces are from an autocorrelation and the curves are normalized). The box shows the input laser characteristics.

On Figure 2, we can see how the soliton loses its shape for a fiber input average power above 5 Watts. In those cases the dispersion was not enough to compensate nonlinear effects. After such observations, the potential of optical solitons for long distance propagations, especially for telecommunications, was clear. Many research activities were developed in this topic [10] [11].

Spatial solitons:

These solitons keep their transversal spatial shape unchanged while propagating in the nonlinear medium. They were firstly predicted in 1964 by launching a continuous wave laser beam into a massive Kerr nonlinearity optical medium [12]. Moreover, these self-trapped beams were not firstly related as spatial solitons, due to the unstable nature of these observations. One has to wait until 1985 to see the first observation of stable spatial Kerr soliton in Limoges [13]. In these experiments, the soliton was set stable by limiting the diffraction to only one spatial dimension, using interference fringes (1D transverse spatial soliton).

Spectral solitons:

Talking about solitons in spatial and temporal dimensions, I need to conclude with the less known (but yet very interesting) case of spectral solitons. These kind of solitons have been reported recently by A. Picozzi *et al.* in 2008 [14]. The particularity of these solitons is due to their spectral incoherence: these waves are not confined in space or time domain, but they shift their frequency while propagating in the nonlinear medium, without any spectral broadening.

I.1.2.2. Variety of the solitons

The solitons I described in the previous paragraphs are Kerr solitons. In the simplest case, the temporal soliton is a 1D wave propagating with a constant temporal envelope along a dispersive media [15] [16]. Thus, for each propagating laser pulse, the Kerr medium nonlinearity counterbalances the linear dispersion, allowing propagation without deformation. For the case of spatial soliton, the diffraction effect is compensated, in one or two transverse dimensions, by a self-focusing effect [17]. In these cases, the laser pulse is spatially self-guided by an ephemeral waveguide only existing during the pulse duration.

Besides the positive envelope (also known as *bright*) Kerr solitons, other types of solitons can exist. By tuning the input conditions, or by changing the main nonlinear effect involved in the creation of such waveform, one can expect numerous other types of solitons, and I will list some of them in the following paragraphs.

Dark solitons:

Dark solitons, contrary to bright solitons, are “holes” on a background composed of a continuous wave.

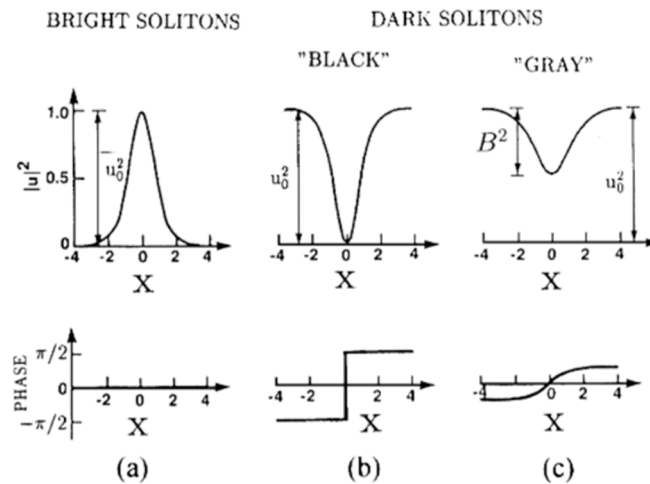


Figure 3: Bright and dark solitons envelope, function of space (X) [18]. (a)-Bright soliton. (b)-Black dark soliton. (c)-Gray dark soliton.

First anticipated in 1973 [19], the dark soliton was experimentally observed in the optical fiber in 1988 for the first time [20]. In this experimental study, the dark soliton was obtained with a pre-shaped initial beam, injected in the fiber. The dark solitons can be divided in two categories [21]: the *black* and the *gray* dark soliton (see Figure 3). The *black* soliton has a minimal value equal to zero, while the *gray* soliton has a minimal value greater than zero, but still lower than the continuous wave background level.

Vectors solitons:

Vectors solitons are composed of multiple coupled components, dependant on polarization. Under this denomination, one can find several types of *hybrid* solitons such as the dark-dark soliton, the dark-bright soliton and the bright-bright soliton [22]. Experimentally, such waveforms can be obtained by coupling multiple properties in a nonlinear material [23] [24] (an optical fiber cavity with weak birefringence for example).

Domain wall solitons:

Domain walls are a type of topological defect, usually related to a brutal symmetry break of the wave phase transition. Because of their similarity with the mathematical kink solution of the Sine-Gordon equation, domain walls solitons are also called kink solitons, and a single kink soliton solution has been found in 1982 [25]. S. Wabnitz *et al.* predicted the optical domain wall soliton through the switch of polarization in fibers [26]. Five years later, this theory was experimentally validated by S. Pitois *et al.* [27].

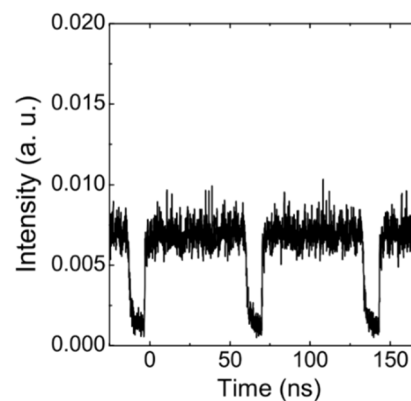


Figure 4: Experimental domain wall dark soliton [28].

Multimode solitons:

The solitons discussed previously can be single mode solitons, meaning that the solitonic waveform appears through only one spatial frequency. Moreover, in 1980, light confinement has been predicted in multimode fibers (where more than one light mode propagates through it) by A. Hasegawa [29]. In such context, a potential multimode soliton solution has been studied few years later [30] [31]. Moreover, one must wait more than two decades for the first experimental observation of multimode solitons in a multimode fiber [32]. In these experiments, Renninger *et al.* used a medium with a relatively small intermodal dispersion to increase nonlinear effects among the different modes. Moreover, the higher order modes total energy was low compared to the fundamental one, and the soliton was very similar to a single mode one. An experimental study by L.G. Wright *et al.* [33] confirmed the theory by showing, through simulations and experiments, a multimode soliton appearance, followed by solitonic fission for higher power values.

Kerr-like solitons:

Some materials, like photorefractive or liquid crystals, can have a nonlinear response competitive to that of Kerr media, and they can allow then the generation of spatial solitons thanks to their unique molecular structure.

Photorefractive effect was firstly observed in Bell laboratory by Ashkin *et al.* in 1966 [34]. This effect causes a change of the material refractive index, induced by light illumination. The spatial variations of light intensity induce the index change. Several processes are mixed to create the photorefractive effect: the illumination induces a photo excitation of charges in the material, and their migration from the bright to the dark areas generates a space charge field producing then a modulation of the refractive index by the Pockels effect (linear modification of the refractive index according to the local electric field). Crystals can be used as photorefractive materials, under the double condition of being photoconductive and having an electro-optical effect. Firstly associated to laser-induced optical damages, photorefractive effect was understood few years later by F.S. Chen [35] [36], opening the way to holographic recordings using photorefractive materials [37]. Already used for data storage, and real-time processing because of its reversibility, M. Segev demonstrated in 1992 that this effect could also be used to focus an optical beam, making possible the generation of 2D spatial solitons [38]. The experimental demonstration was made the following year [39]. Figure 5 shows the slow (non-instantaneous response of the matter) 2D photorefractive soliton generation process.

The same 2D spatial solitons can be obtained in liquid crystals, where the refractive index modification is due to thermal effect or molecular reorganization [40]. In regards of photorefractive material, liquid crystals exhibit a shorter refractive index reconfiguration time, allowing all-optical fast switching applications [41]. However, beam confinement is more efficient in photorefractive media. Photorefractive and liquid crystals solitons are not considered as “real” solitons since the medium remains altered by the electromagnetic field even after the extinction of this last one.

Another type of *Kerr-like* soliton is generated in crystals with the quadratic nonlinearity, with, this time, an instantaneous nonlinear response. My thesis experiments are oriented to explore such quadratic spatial solitons. For this reason, a complete study of such type of interesting phenomenon is given in the next chapter.

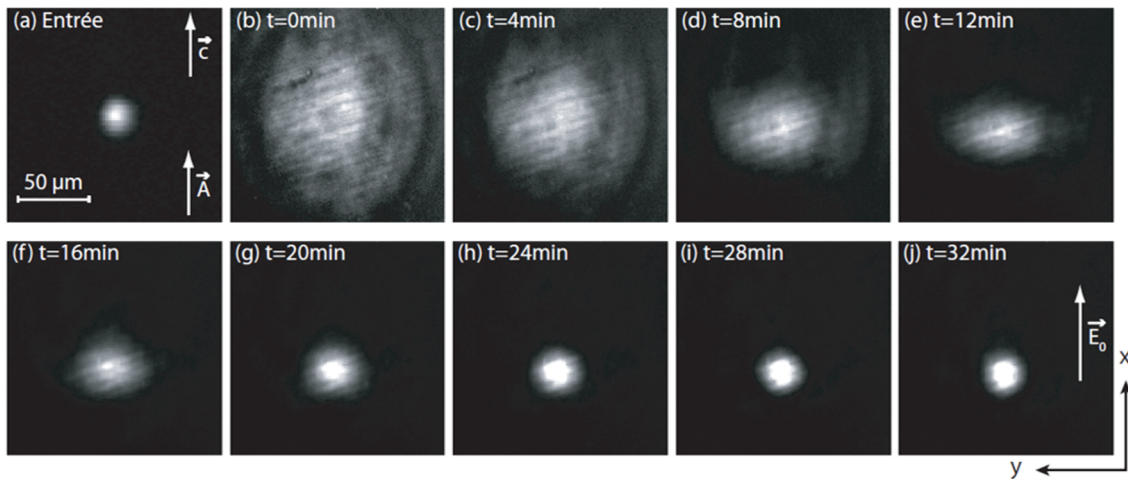


Figure 5: Experimental photorefractive soliton formation in LiNbO_3 material [42]. **(a)**-Input beam shape. **(b-j)**- Output beam shape at different light exposure times. A and C vectors are relative to the optical polarization field, while E_0 vector is relative to the electrical field around the material. The light illumination remains constant during all the process time.

Raman solitons:

Solitons, instead of being generated by Kerr nonlinearity, can be generated by Raman nonlinearity [15]. Raman solitons are formed into a fiber cavity. They were experimentally observed in 1984 [43] and a theory of such process was made one year later [44]. It has been shown later that Raman gain could be used to generate solitons in such fiber ring setup [45] [46]. An example of Raman soliton fiber cavity is shown in Figure 6 where a Raman pump is used to generate a soliton on its Stokes wavelength.

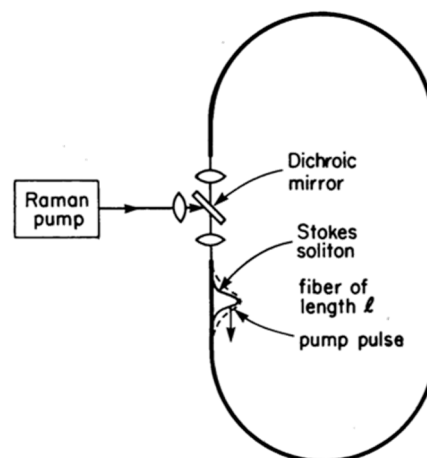


Figure 6: Raman Stokes soliton generation in a fiber cavity [47].

Light bullets:

Light bullets are spatial and temporal domains solitons. They are the ultimate research goal on optical solitons [48]. They can be obtained by trapping the beam both spatially (in the two transverse dimensions) and temporally ((3+1)D configuration), to prevent diffraction and dispersion from occurring simultaneously. In 1990, Silberberg [49] suggested that a space-time compression in a Kerr medium would be unstable, since the propagation would be (2+1)D. However, by including terms such as multiphoton absorption or stimulated Raman scattering, the propagation can be stabilized. A spatiotemporal self-focusing has been demonstrated in a Kerr medium for planar configuration [50], however, stabilizing a (3+1)D propagation in a Kerr medium is not yet possible. Other media are considered, notably quadratic media which can also propagate temporal solitons [51]. The first demonstration of a space-time soliton in a quadratic medium was made by Liu *et al.* [52] [53], again in a planar configuration. In these experiments, the need to have tilted wavefronts at the crystal entrance for phase tuning makes the propagation less stable and prevents any (3+1)D propagation. New theoretical investigations are carried out [54] [55] [56] but the light bullets have not been obtained yet.

Dissipative solitons:

Dissipative solitons, introduced in 1991 by Picholle *et al.* [57], are localized formations that in the presence of nonlinearity, dispersion and/or diffraction, maintain their equilibrium through an exchange of energy with the external environment.

The existence and stability of the dissipative soliton depend on a continuous supply of energy to the system (as in the case of laser cavity). When this energy supply ceases, or when the parameters of the system no longer coincide with those allowing the formation of the soliton, the dissipative solitons disappear [58]. The formation of a dissipative soliton in a cavity involves a variety of stabilization mechanisms, depending on the nature of the cavity. These mechanisms have a common characteristic: they involve a compensation process between the intra-cavity losses and a gain of energy provided by the environment.

Some properties of dissipative solitons make them very attractive for research. First, their intensity profile, amplitude and velocity remain fixed, and are defined by the parameters of

the system [59] rather than by the initial conditions. Secondly, they can exist indefinitely in time as long as an energy is provided to the system (or as long as the required parameters are present in the system, allowing dissipative soliton existence).

Solitons on continuous-wave background:

Such waveforms are of particular interest for my thesis. Such interest is not related to the fact that these waves propagate on a continuous background, but on the fact that these waves may appear and disappear without leaving a trace when the nonlinearity increases. In short, my thesis deals with ephemeral appearance of 2D extreme waves, whose dynamics mimics, in a quadratic crystal, the behavior of soliton propagating on continuous background. In this way, the reader can find a detailed study of these solitons in the following parts of this chapter (see paragraph I.2.3), after a short presentation of the NLSE.

I.1.2.3. Some special soliton dynamics

I will complete this short review on solitons in optical systems by briefly mentioning some unconventional dynamics when solitons propagate under special conditions. Indeed, as described before, the soliton is typically propagating alone, in one propagation direction, and his envelope is not modified by its environment. However, there are circumstances allowing solitonic fission, fusion, repulsion, spiraling and walking solitons.

Soliton fission and self-frequency shift:

When a soliton of order $N > 1$ (which means that the nonlinearity is higher than the dispersion) propagates in a medium in the presence of weak perturbations (like third order dispersion), the pulse can break into multiple solitons of lower order, until reaching the first order. Such process is used in supercontinuum generation [60] [61] [62] (see Figure 7): the initial soliton fission leads to multiple solitons generation, each one propagating through the medium with a different wavelength, due to self-frequency shift.

Soliton self-frequency shift was first experimentally discovered by Mitschke and Mollenauer in 1986 [63], then a theory was developed the same year by Gordon [64]. Self-frequency shift

of the soliton is due to the Raman effect occurring while light propagates through the nonlinear medium, forcing the shift of the soliton through lower-frequency parts. The mixing of the soliton self-frequency shift with other nonlinear effects (which cause spectral broadening) leads to the generation of large supercontinuum.

Figure 7 shows, on right, a time shift of high-energy solitons during the propagation in the fiber. This time shift is due to soliton self-frequency shift, after fission of the initial soliton, leading to a delay between each solitons because of the material chromatic dispersion.

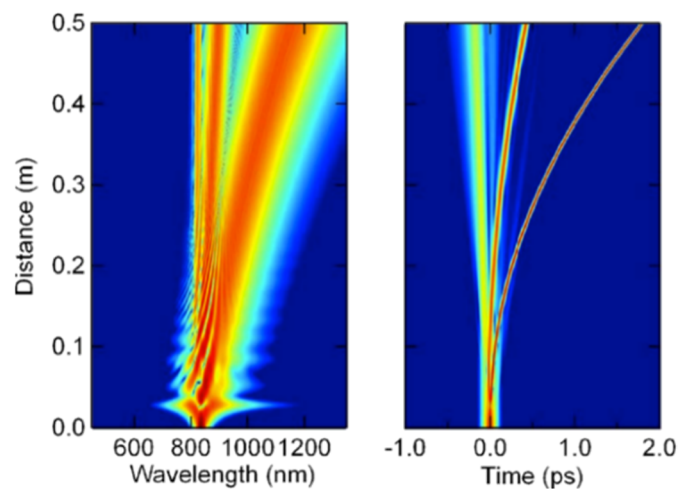


Figure 7: Numerical simulation of a supercontinuum generation in an optical fiber, due to $N = 3$ soliton fission [62]. **Left**-The resulting supercontinuum of light. **Right**-Time shift of the high-energy solitons while propagating in the fiber, after fission of the injected (Distance = 0) soliton.

Solitons collision:

When two or more solitons propagate with different group velocities along a nonlinear dispersive medium, collisions may occur between two of them. In materials with quasi-instantaneous nonlinear response (Kerr or quadratic materials), solitons can attract or repel each other, depending on their relative phases [65] [66]. Repulsive collision mechanisms can find applications in all-optical demultiplexing for example, where a phase-controlled soliton will change the direction of another soliton in a pulse train [67]. Moreover, the phase sensitivity of such process can be thwarted by changing the soliton polarization [68] or the soliton spectrum [69] for example.

Walking soliton:

Solitons can see their temporal or spatial group velocity accelerated or slowed down by the material: such solutions are named *walking solitons*. It has been observed in birefringent materials, such as quadratic crystals [70] or special optical fibers [71], and experimental results were then quickly obtained [72]. In 1996, W. E. Torruellas and L. Torner [73] simulated a game of billiards, involving all the solitonic waveforms generated by the quadratic nonlinear process, using the walking properties of these soliton components.

I.2. Nonlinear Schrödinger equation

The NLSE allows the mathematical description of nonlinear phenomena in optics by adding, in a single equation, nonlinear and linear terms as diffraction and/or dispersion. One can then calculate the spatial and temporal evolution of electromagnetic wave envelope propagating in a nonlinear dispersive medium. It is necessary to start from Maxwell equations to understand the origin of the NLSE.

I.2.1. From the Maxwell equations to the nonlinear Schrödinger equation

Maxwell equations are differential coupled equations, giving the evolution of an electromagnetic field in time and space:

$$\begin{aligned}\nabla \times \vec{E} &= -\frac{\partial \vec{B}}{\partial t} \\ \nabla \times \vec{H} &= \vec{J} + \frac{\partial \vec{D}}{\partial t} \\ \nabla \cdot \vec{D} &= \rho_f \\ \nabla \cdot \vec{B} &= 0\end{aligned}\tag{1.1}$$

Where \vec{H} and \vec{E} are the magnetic and electric field, \vec{J} is the current density vector, \vec{B} and \vec{D} are the magnetic and electric flux density, and ρ_f is the free electric charge density. The studied optical medium here is dielectric so there are no free charges. In these conditions, $\vec{J} = 0$ and $\rho_f = 0$. The flux density is relative to the field while propagating in the medium and the following equation gives the relation between them:

$$\begin{aligned}\vec{D} &= \epsilon_0 \vec{E} + \vec{P} \\ \vec{B} &= \mu_0 \vec{H} + \vec{M}\end{aligned}\quad (1.2)$$

\vec{M} and \vec{P} are respectively the magnetic and electric polarization vector induced by the oscillation of the electrons in the medium when an electromagnetic wave is transmitted through it, and μ_0, ϵ_0 are the vacuum permeability and the permittivity. In nonmagnetic mediums, such as optical silica fiber: $\vec{M} = 0$. A single equation can be developed from the previous coupled equations:

$$\nabla \times \nabla \times \vec{E} = -\frac{\partial(\nabla \times \vec{B})}{\partial t} = -\mu_0 \frac{\partial(\nabla \times \vec{H})}{\partial t} = -\mu_0 \frac{\partial^2 \vec{D}}{\partial t^2} \quad (1.3)$$

Knowing the relation: $\mu_0 \epsilon_0 = \frac{1}{c^2}$, the last equation leads to a simpler time propagation equation, dependent on the electric and polarization fields:

$$\nabla \times \nabla \times \vec{E} = -\frac{1}{c^2} \frac{\partial^2 \vec{E}}{\partial t^2} - \mu_0 \frac{\partial^2 \vec{P}}{\partial t^2} \quad (1.4)$$

In dielectric medium where $\nabla \cdot \vec{D} = 0$, it is now possible to simplify $\nabla \times \nabla \times \vec{E}$ with the following equation:

$$\nabla \times \nabla \times \vec{E} = \nabla(\nabla \cdot \vec{E}) - \Delta \vec{E} = -\Delta \vec{E} \quad (1.5)$$

\vec{P} is directly dependent of the electric field:

$$\vec{P} = \epsilon_0 \chi^{(1)} \vec{E} + \epsilon_0 \chi^{(2)} \vec{E}^2 + \epsilon_0 \chi^{(3)} \vec{E}^3 + \dots = \vec{P}_L + \vec{P}_{NL} \quad (1.6)$$

With $\chi^{(1)}$ the linear susceptibility of the medium and $\chi^{(2)}, \chi^{(3)}, \dots$ the quadratic and cubic susceptibilities respectively.

A part of the electric polarization is linear (\vec{P}_L): the molecular displacement, and then the electron oscillation in the material, is proportional to the electric field intensity. Another part of the electric polarization is nonlinear (\vec{P}_{NL}): when the electric field is above a certain amplitude threshold, the molecule affected by this field is subject to saturation, distension, dissymmetry or to other effects changing the electron oscillation behavior under the external strong electromagnetic field. This oscillation modification will affect the total polarization of

the medium and then the external electric field propagation. The following relations can be considered:

$$\begin{aligned}\vec{P}_L &= \varepsilon_0 \chi^{(1)} \vec{E} \\ \vec{P}_{NL} &= \varepsilon_0 \chi^{(2)} \vec{E}^2 + \varepsilon_0 \chi^{(3)} \vec{E}^3 + \dots\end{aligned}\quad (1.7)$$

The electric field propagation equation can now be written as:

$$\Delta \vec{E} - \frac{1}{c^2} \frac{\partial^2 \vec{E}}{\partial t^2} = \mu_0 \frac{\partial^2 \vec{P}_L}{\partial t^2} + \mu_0 \frac{\partial^2 \vec{P}_{NL}}{\partial t^2}\quad (1.8)$$

Since the optical fiber is the main observation medium for solitons, we will consider, in the following parts of this chapter, the nonlinear medium as amorphous silica. In order to simplify the following equations, we will consider the electromagnetic waves as a single mode beam propagating in a silica fiber with only $\chi^{(3)}$ susceptibility. The wave propagation direction is \vec{z} and its linear polarization direction is on \vec{x} . The electric field \vec{E} and the polarization field \vec{P} can be decomposed as follows [15]:

$$\begin{aligned}\vec{E}(\vec{r}, t) &= \frac{1}{2} \vec{x} \{ F(x, y) \Psi(z, t) e^{i(\beta_0 z - \omega_0 t)} + c.c. \} \\ \vec{P}(\vec{r}, t) &= \frac{1}{2} \vec{x} \{ F(x, y) P(z, t) e^{i(\beta_0 z - \omega_0 t)} + c.c. \}\end{aligned}\quad (1.9)$$

Where $F(x, y)$ is the transverse envelope of the wave, $\Psi(z, t)$ and $P(z, t)$ are respectively the electric and polarization propagating envelope, β_0 is the propagating constant of the wave, with pulsation at ω_0 , and $c.c.$ is the complex conjugate term. The envelope is slowly varying in comparison to the optical carried frequency, so we can consider $|\Psi(z, t)|^2$ as the instantaneous power. From the equation (1.7) and (1.9), we can now calculate the linear and nonlinear polarizations:

$$\begin{aligned}P_L(z, t) &= \varepsilon_0 \chi^{(1)} \Psi(z, t) \\ P_{NL}(z, t) &= \frac{3}{4} \varepsilon_0 \chi^{(3)} |\Psi(z, t)|^2 \Psi(z, t) = \varepsilon_0 \varepsilon_{NL} \Psi(z, t)\end{aligned}\quad (1.10)$$

The total polarization is now the following, from (1.6):

$$P(z, t) = \varepsilon_0 (\chi^{(1)} + \varepsilon_{NL}) \Psi(z, t)\quad (1.11)$$

Where ε_{NL} is the nonlinear component of the frequency dependent relative permittivity $\varepsilon_r(\omega)$ which gives use, for a given frequency, the total refractive index n :

$$\begin{aligned} n^2 &= \varepsilon_r(\omega) = \varepsilon_L + \varepsilon_{NL} \\ n^2 &= 1 + \chi^{(1)} + \left(\frac{3}{4}\chi^{(3)}|\Psi(z,t)|^2\right) \end{aligned} \quad (1.12)$$

ε_L is the linear component of the frequency dependent relative permittivity. From the last equation, we can calculate the refractive index in function of the wave frequency, relative to ω , and the light intensity, relative to $|\Psi(z,t)|^2$:

$$n(\omega, |\Psi|^2) = n_L(\omega) + n_2 |\Psi|^2 \quad (1.13)$$

It is then possible to get the linear n_L and nonlinear n_2 parts of the refractive index, calculated from the real and imaginary parts of $\chi^{(1)}$ [74]:

$$\begin{aligned} n_L(\omega) &= 1 + \frac{1}{2} \text{Re}(\chi^{(1)}) \\ n_2 &= \frac{3}{8n_L(\omega)} \text{Re}(\chi^{(3)}) \end{aligned} \quad (1.14)$$

From equations (1.8), (1.9) and (1.10), one can obtain the following form of the NLSE [15] [74]:

$$\frac{\partial \Psi}{\partial z} + \beta_1 \frac{\partial \Psi}{\partial t} + i \frac{\beta_2}{2} \frac{\partial^2 \Psi}{\partial t^2} - i \gamma(\omega_0) |\Psi|^2 \Psi = 0 \quad (1.15)$$

With β_1 the inverse of group velocity, β_2 the group velocity dispersion (its physical origin is recalled in section I.3.1.2) and $\gamma(\omega_0)$ the nonlinear coefficient, relative to Kerr effect and developed in I.3.2.2 section.

By changing the referential into group impulse coordinates, $t = t - \beta_1 z$, it is now possible to obtain a simplified NLSE which takes the following form:

$$i \frac{\partial \Psi}{\partial z} - \frac{\beta_2}{2} \frac{\partial^2 \Psi}{\partial t^2} + \gamma |\Psi|^2 \Psi = 0 \quad (1.16)$$

Light propagation in optical fiber can be described with the integrable NLSE, allowing quick solutions with inverse scattering method [75]. Equation 1.15 can be solved by the split-step Fourier method [15]. This equation is now the most used one to predict solitons in optics, as we will see in the following parts of this chapter.

I.2.2. Introducing modulation instability in the nonlinear Schrödinger equation

In this paragraph, I will introduce instabilities in the Schrödinger nonlinear wave propagation equation. MI is characterized by the growing of a weak modulation of a continuous wave, in a nonlinear medium with anomalous dispersion or with the focusing NLSE. MI leads to the generation of large-amplitude periodical wave trains. In spatial domain, MI changes weakly modulated waves into periodical patterns (see Figure 8-top). We observe on this figure the evolution of the envelope amplitude during propagation, leading to the degradation of a continuous wave for a given propagation length (superior to z_1). In spectral domain, MI is characterized by the transfer of energy between a single component (ω) to multiple sidebands (see Figure 8-bottom). The spectral dynamics of MI is that of a degenerated Four-Wave Mixing effect [15].

In the hydrodynamic field, MI has been observed in deep water (analogous to the anomalous dispersion regime in optics). MI is seeded by the natural envelope amplitude modulation of water (caused by the wind for example). With dispersive and nonlinear effects, some of the modulation frequencies are favored and grow exponentially, leading in the strong conversion to catastrophic behaviors, such as rogue waves. These instabilities, studied in hydrodynamics, are called Benjamin-Feir instabilities [76] [77]. In optics, MI grows spontaneously when driven by noise, or can be induced by adding an intensity modulator [74]. The phenomenon of growing on modulation instability sidebands can be analytically described by using the NLSE, and this point is the subject of the next paragraph.

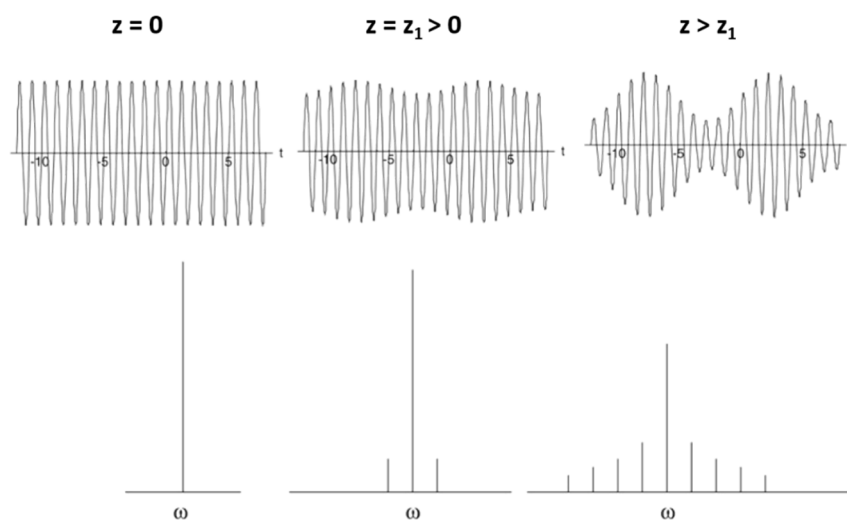


Figure 8: MI evolution in a nonlinear medium [78].

I.2.3. Solitons generated by modulation instability

Under MI, non-zero background solitons can exist and their existence have been predicted by Akhmediev [79], Peregrine [80], Kuznetsov [81] and Ma [82]. In order to observe such special solutions of the NLSE, it is preferable first to normalize the space and time propagation variables in equation (1.16):

$$\xi = \frac{z}{L_{NL}}; \tau = \frac{t}{\tau_0} \quad (1.17)$$

$L_{NL} = 1/(\gamma P)$ is the nonlinear length (with P the input power) and $\tau_0 = (\beta_2 L_{NL})^{1/2}$ is the period of the MI. With the new normalized parameters ξ and τ , the NLSE reads as:

$$i \frac{\partial \Psi}{\partial \xi} + \frac{1}{2} \frac{\partial^2 \Psi}{\partial \tau^2} + |\Psi|^2 \Psi = 0 \quad (1.18)$$

With this equation, it is now possible to calculate the soliton solution on a non-zero background, growing on MI.

I.2.3.1. Akhmediev breathers

This first analytic solution of the normalized NLSE is a low-frequency modulation envelope wave composed by high amplitude solitons. Akhmediev breathers are localized in propagation coordinates and periodic in time coordinates. To understand the behavior of such waveform, it is necessary to introduce a new parameter in the wave amplitude propagation: a .

The analytic Akhmediev breather solution is the following, for $0 < a < 0.5$:

$$\Psi(\xi, \tau) = e^{i\xi} \left[1 + \frac{2(1-2a)\cosh(b\xi) + ib\sinh(b\xi)}{\sqrt{2a\cos(\Omega\tau) - \cosh(b\xi)}} \right] \quad (1.19)$$

Where b determines the instability growth and Ω the modulation frequency [74] [83]:

$$b = [8a(1-2a)]^{\frac{1}{2}}; \quad \Omega = 2(1-2a)^{\frac{1}{2}} \quad (1.20)$$

When $a = 0$, the solution of the equation (1.19) is a continuous wave. It gains amplitude when a increases, but the number of solitons and the modulation envelope frequency decreases.

Figure 9 illustrate an example of Akhmediev breather for $a = 0.25$, the background is 3 times less important than the solitons amplitude, and minima appear around solitons, with a smaller amplitude value than the continuous background.

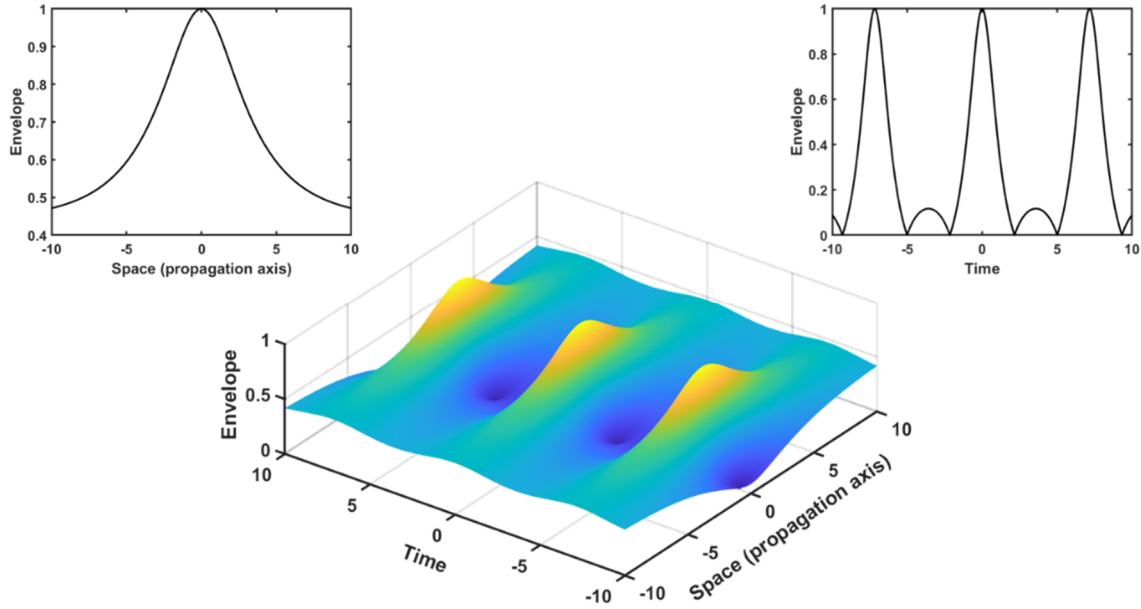


Figure 9: Example of Akhmediev breather, for $a = 0.25$.

The Akhmediev breathers periodicity disappears in time when the parameter a approaches 0.5, which is a limit value for the equation (1.19). In that case, the breathers periodicity tends to the infinite and the central soliton ($\xi = 0$ and $\tau = 0$) is the only one remaining. Peregrine made a derivation of the analytical model seen in equation (1.19) [80].

I.2.3.2. Peregrine solitons

For $a = 0.5$, the equation (1.19) can be reduced as follow:

$$\Psi(\xi, \tau) = e^{i\xi} \left[1 - \frac{4(1+2i\xi)}{1+4\tau^2+4\xi^2} \right] \quad (1.21)$$

In this solution, the periodicity parameters (1.19) disappear as the length between each peak event becomes infinite. This derivation allows to obtain a mathematical model for a localized (space (1D) or time (1D)) extreme event called the Peregrine soliton (see Figure 10).

Around a localized soliton in time or space, one can draw similar observation as for the case of Akhmediev breathers: a continuous background exists, and there are minima of energy close to the central high amplitude.

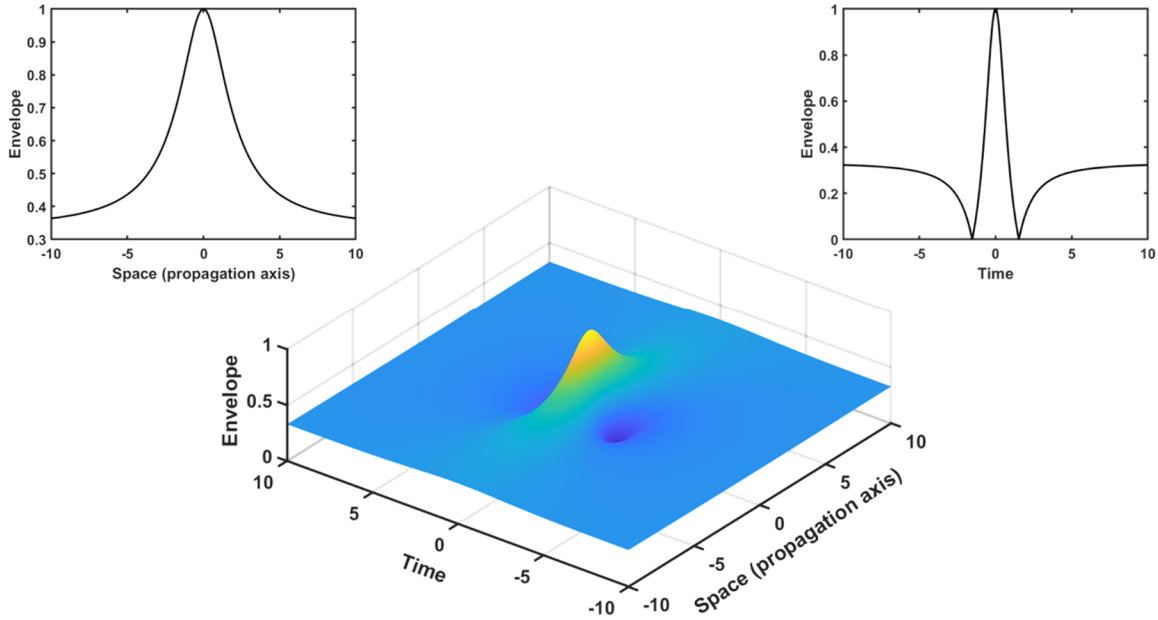


Figure 10: Example of Peregrine soliton, for $a = 0.5$.

I.2.3.3. Kuznetsov-Ma breathers

The Kuznetsov-Ma breathers are mathematical solutions of NLSE with continuous background when $a > 0.5$. For such range of values, b and Ω parameters become imaginary (equation (1.22)) and switch axis periodicity of the Akhmediev equation (1.19) to the other axis. The complete description of these breathers has been realized in 1979 [82] and gave a mathematical solution similar to the Akhmediev breathers but with a periodicity developed along the longitudinal propagating axis, and no longer on the temporal axis as for the case Akhmediev breathers (1.23).

$$b = i[8a(2a-1)]^{\frac{1}{2}} ; \Omega = 2i(2a-1)^{\frac{1}{2}} \quad (1.22)$$

$$\Psi(\xi, \tau) = e^{i\xi} \left[1 + \frac{2(1-2a)\cos(|b|\xi) + i|b|\sinh(|b|\xi)}{\sqrt{2a}\cos(|\Omega|\tau) - \cosh(|b|\xi)} \right] \quad (1.23)$$

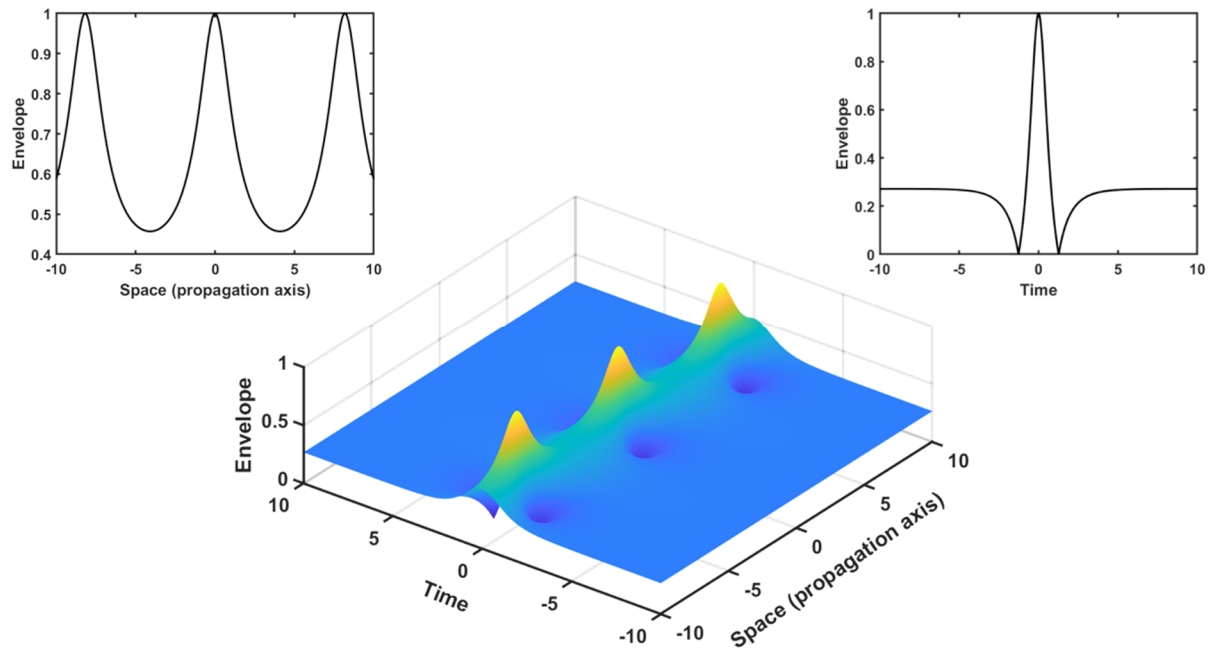


Figure 11: Example of Kuznetsov-Ma breather, for $a = 0.95$.

At some time and space values, we can observe minima of energy, below the continuous wave level, acting like a depletion around the solitons. Such behavior of the mathematical solution is very similar to what we can observe in hydrodynamics (water depletion before and after the high amplitude wave) and in optics [74].

Optical field of physics is the one we will study in the following lines, because it allows us to observe extreme events, such as non-zero background solitons, in a relatively small setup. For example, Chabchoub *et al.* used a wave tank with a length of 15 meters, for a width of 1.5 meter and a water depth of 1 meter as experimental setup for Akhmediev and Kuznetsov-Ma breathers experiments [84]. Similar results have been observed in optics by Kibler *et al.* [85] using few kilometers of optical fibers as a nonlinear medium.

Optical fibers are a good nonlinear medium since it allows soliton propagation studies along kilometers without significant loss and with the possibility to observe the light dynamic at any particular fiber length. Peregrine solitons have been observed in fibers by Kibler *et al.* in 2010 [86]. One year later, studies on MI spectral dynamic were carried out using the Akhmediev breather theory [87]. In 2012, the first results on Kuznetsov-Ma waveforms in optics were published [85].

I.3. Silica fibers as a perfect physical environment to observe solitons

The nonlinear silica fiber is a historical medium for optical soliton generation [56]. Fibers have been used since the 50s for endoscopic applications; flexible glass waveguides have been used for telecom applications ten years later, after the invention of the laser. Indeed, due to the important losses in the first samples of optical fibers, it was necessary to wait the invention of a high-intensity light source in order to observe the light guidance along kilometers of propagation. Progress were made in optical fiber fabrication, to reduce losses at specific laser wavelength (Near Infrared - NIR wavelengths are mostly used in telecom, due to the relative low attenuation and low dispersion of these frequencies while propagating in the fiber) and in parallel, lasers sources became more and more powerful, allowing the transmission of light to further and further distances. However, life always finds a way to bother the engineer, and nonlinearities appeared when the optical power was above a given energy threshold. These nonlinearities degraded, most of the time, the signal; however, under some circumstances, the fiber nonlinearity permitted to transmit undistorted ultrashort pulses over thousands of kilometers of fiber (thus, we can talk about solitons propagation). The first soliton in optical fiber was then observed in 1980 [9].

Silica fibers are dielectric waveguides for optical frequencies. They transmit light through the core by means of total internal reflection. In order to keep light in the center of the fiber, it is necessary to have a core refractive index higher than the refractive index of the cladding. In order to increase the refractive index of silica SiO_2 , the core can be doped with germanium dioxide GeO_2 , or aluminum oxide Al_2O_3 . It is also possible to dope the cladding part of the fiber for decreasing, this time, the refractive index (with boron dioxide B_2O_3 for example). The silica fiber is also coated with a polymer to avoid external deterioration and to improve mechanical properties when bending and crushing are applied.

Light propagates in optical fibers with specific spatial distributions called electromagnetic transverse modes (see Figure 12). In a standard step-index fiber, when the normalized spatial frequency V is lower or equal to 2.405, the optical fiber is considered as single mode, meaning only one spatial frequency, which can be approximated by a Gaussian, can propagate in the waveguide. For higher values of V , the fiber allows the propagation of several modes. The V coefficient is defined as follow:

$$V = \frac{2\pi a}{\lambda} \sqrt{n_c^2 - n_g^2} \quad (1.24)$$

Where a is the fiber core radius, λ is the propagating light wavelength, and n_c, n_g are the core and cladding refractive indexes.

Silica fibers are now the most used waveguides for light, since they are cheap, usable and easy to produce. However, several linear and nonlinear effects can affect the electromagnetic field propagation.

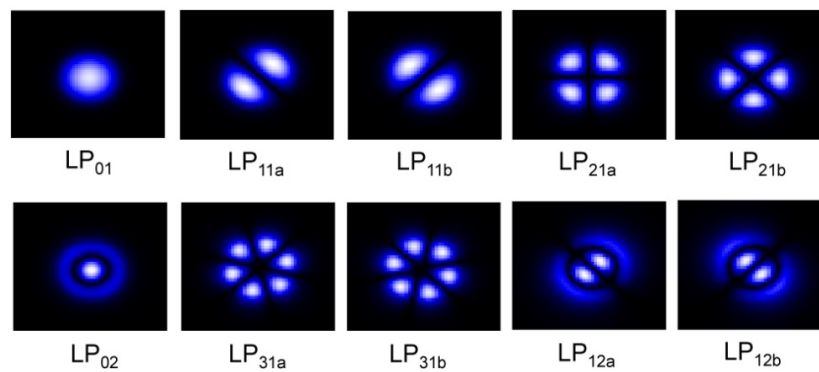


Figure 12: Simulated isolated spatial frequencies at the output face of a multimode fiber [88].

I.3.1. Linear effects in silica fiber

Several linear effects affect the spatial and temporal wave envelope independently to the electromagnetic field intensity. The most famous are the attenuation and dispersion effects.

I.3.1.1. Attenuation

Optical attenuation in fibers, also called transmission losses, is the first effect ever observed in this type of medium. Transmission losses can have many origins, such as mechanical torsions, imperfect junctions between the fiber core and cladding or molecular origins as linear scattering or material absorption mainly due to the hydroxyl OH^- ions occurring in particular at 1380 nm. Impurities inside silica can also be at the origin of significant losses [89].

The main scattering process in optical fibers is due to Rayleigh effect, dependent on the wave frequency. Rayleigh scattering is a limit case of Mie scattering where all of the optical wavelengths are affected due to big particles presence on the optical path [90].

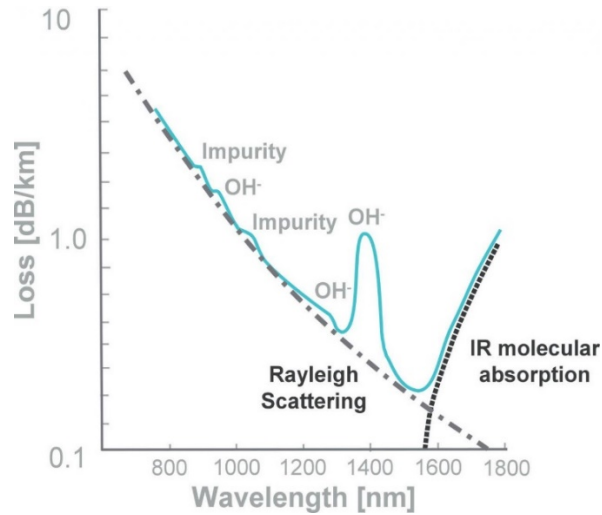


Figure 13: Light attenuation in silica optical fiber, in function of the wavelength. This figure comes from Fibercore website.

The attenuation α is usually expressed in dB/km and given by the following equation:

$$\alpha_{dB} = -\frac{10}{L} \log\left(\frac{P_o}{P_i}\right) \quad (1.25)$$

With L the propagation length, P_i and P_o respectively the input and output power of light in silica fiber.

I.3.1.2. Dispersion

The dispersion (D) of the optical fiber is the combination of two contributions, one of the material and one of the waveguide. When an electromagnetic wave propagates in a dielectric medium (a fiber in our case), this wave will interact with the electrons of the dielectric material.

The dispersion of the material results in a dependence of the refractive index with the wavelengths so that each wavelength will travel with different speeds in the waveguide. The dispersion of the waveguide will depend on the fiber design: the core radius and the index difference between the core and the cladding. Light speed will depend on the light transverse location in the fiber, hence the appearance of optical delays after propagation in the fiber [74].

D , expressed in $\text{ps}\cdot\text{nm}^{-1}\cdot\text{km}^{-1}$, is directly linked to β_2 and depends on the wavelength λ :

$$D = -\frac{2\pi c}{\lambda^2} \beta_2 \quad (1.26)$$

In standard single-mode fibers, the Zero Dispersion Wavelength (ZDW) is the wavelength at which waveguide dispersion and material dispersion cancel each other, and the total dispersion (D) is equal to 0. For telecom applications, the fiber is doped to shift the ZDW toward 1550 nm (ZDW is at 1310 nm in all-silica fiber), in order to minimize the propagation losses (see Figure 13).

In the same standard single-mode fibers, when the light wavelength is shorter than the fiber ZDW, the dispersion is called normal ($D < 0$) thus, shorter wavelengths will propagate faster than longer ones (positive frequency chirp). On the contrary, for longer wavelengths, the dispersion is called anomalous ($D > 0$) and shorter wavelengths will propagate slower than larger wavelengths (negative frequency chirp). Solitons appear mainly in anomalous dispersion regime, where Kerr nonlinearity counterbalances dispersion. However, some examples of soliton propagation can be found in normal dispersive regime in particular conditions [91]. Dispersion versus wavelengths evolves with the fibers geometry or composition. For example, the hollow-core fiber [92] exhibits anomalous dispersion regime for any chosen guided wavelength (see Figure 14 for an example of hollow-core fiber).

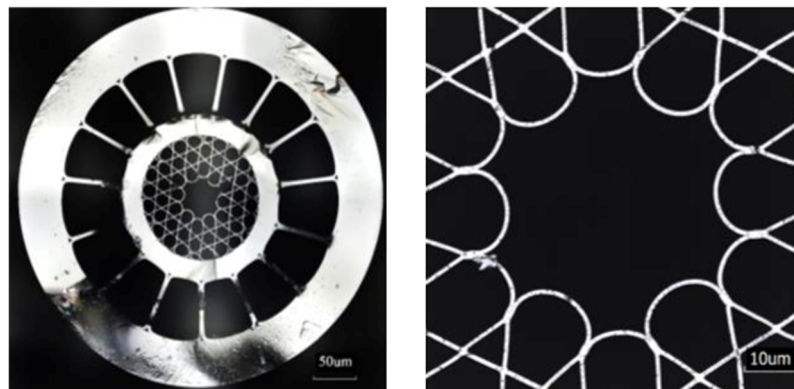


Figure 14: Example of a microstructured hollow-core fiber, drawn by F. Delahaye at XLIM laboratory [93].

Left-Side cut of the fiber, **Right**-Zoom on the fiber core.

I.3.2. Nonlinear effects in silica fiber

Nonlinear effects taking place in optical fibers can seriously affect spatial and temporal wave envelopes and distort the initial structure of the light pulses, because of the anharmonic molecular and atomic responses of the medium under strong beam intensity. Thus, significant pump depletion, frequency conversion, pulse breaking, anomalous absorption due to multiphoton process, etc., can exist.

I.3.2.1. Raman effect

When an electromagnetic wave propagates in a dielectric medium, inelastic scattering may occur. This non-instantaneous process comes with kinetic energy losses due to collision between corpuscles (photons and atoms), leading to a frequency shift between the incident and the scattered lights. The lost energy is transferred toward phonons, which propagate in the matter. Thus, we spontaneously obtain a Stokes line at higher wavelength (we can talk about spontaneous Raman effect). Stimulated Raman process is also possible when the light propagates through an excited molecule. In that case, the energy stored by the molecule can be released to the initial beam by creating an anti-Stokes line at a shorter wavelength. Thus, stimulated Raman is understood as a resonant four-wave mixing process. The Raman shift depends on the molecular structure i. e. the medium nature. In silica fiber, Raman shift is close to 13.2 THz and can be modified by doping the glass.

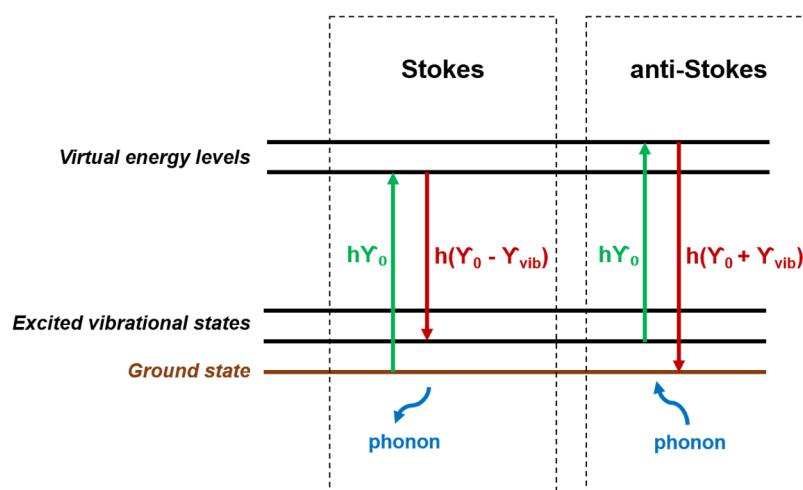


Figure 15: Raman Stokes and anti-Stokes energetic level. $h\gamma_0$ is the incident photon energy, and $h\gamma_{vib}$ the energy transmitted to the molecule.

I.3.2.2. Kerr effect

Kerr effect is an instantaneous nonlinear process, well known in optical fibers, which induces a modification of the refractive index of the medium, proportional to the intensity of an optical beam (see equation (1.13) for more information). This effect is mathematically implemented in the NLSE (1.16) in the term: $\gamma |\Psi|^2 \Psi$. The Kerr effect depends on the field envelope Ψ but also on the nonlinear coefficient γ , which contains the nonlinear response of the medium and the surface covered by the incident beam:

$$\gamma = \frac{\omega_0 n_2}{c A_{eff}} \quad (1.27)$$

Where ω_0 is the center frequency of the wave packet and A_{eff} the effective area of the injected light beam. Kerr effect leads to several processes, such as self and cross-phase modulations, four-wave mixing,...

Self-phase modulation effect, in particular, is responsible of the soliton formation. As the refractive index becomes dependent of the field intensity $I = |\Psi|^2$ for a single center frequency, $n(I) = n_1 + n_2 I$ will produce an instantaneous phase shift ϕ of the wave packet, centered on the wavelength λ_0 while propagating in the nonlinear medium of length L [15]:

$$\phi(t) = \omega_0 t - \frac{2\pi L}{\lambda_0} n(I) \quad (1.28)$$

This instantaneous phase shift compensates the linear phase shift, introduced in anomalous dispersion, with an opposite chirp, allowing the generation of solitons in such configurations [94].

Conclusion – Chapter I

In this first chapter, I briefly recalled some historical perspectives on solitons and their observations mainly in optical materials. I pointed out how solitons can exist in several dimensions and I gave examples of basic interactions between them. I introduced the NLSE and described some of its solutions of solitary waves propagating on MI non-zero background. These solitons seem to be more appropriate to explain extreme rogue events observed in nature, which appear and disappear without leaving trace. At the end of this chapter, I focused more my attention to linear and nonlinear effects in fibers, responsible of the generation of solitons in those materials.

Even if my work is not directly centered in third-order susceptibility silica materials, the phenomena that I observed exhibit several similarities with solitary waves obtained in 1D in optical fibers and I was inspired by these results to explain my observations that will be discussed in the next chapters.

Bibliography – Chapter I

- [1] Rybakov, Y. P., & Saha, B. (1995). Soliton model of atom. *Foundations of Physics*, 25(12), 1723-1731.
- [2] Russell, J. S. (1845). Report on Waves: Made to the Meetings of the British Association in 1842-43.
- [3] Boussinesq, J. (1871). Théorie de l'intumescence liquide appelée onde solitaire ou de translation se propageant dans un canal rectangulaire. *CR Acad. Sci. Paris*, 72(755-759), 1871.
- [4] Rayleigh, L. (1876). On waves. *Phil. Mag.*, 1, 257-259.
- [5] Korteweg, D. J., & De Vries, G. (1895). XLI. On the change of form of long waves advancing in a rectangular canal, and on a new type of long stationary waves. *The London, Edinburgh, and Dublin Philosophical Magazine and Journal of Science*, 39(240), 422-443.
- [6] Maiman, T. H. (1960). Stimulated optical radiation in ruby. *Nature*, 187(4736), 493-494.
- [7] McCall, S. L., & Hahn, E. L. (1967). Self-induced transparency by pulsed coherent light. *Physical Review Letters*, 18(21), 908.
- [8] Hasegawa, A., & Tappert, F. (1973). Transmission of stationary nonlinear optical pulses in dispersive dielectric fibers. I. Anomalous dispersion. *Applied Physics Letters*, 23(3), 142-144.
- [9] Mollenauer, L. F., Stolen, R. H., & Gordon, J. P. (1980). Experimental observation of picosecond pulse narrowing and solitons in optical fibers. *Physical Review Letters*, 45(13), 1095.
- [10] Hasegawa, A., & Kodama, Y. (1995). *Solitons in optical communications* (No. 7). Oxford University Press on Demand.
- [11] Haus, H. A., & Wong, W. S. (1996). Solitons in optical communications. *Reviews of modern physics*, 68(2), 423.
- [12] Chiao, R. Y., Garmire, E., & Townes, C. H. (1964). Self-trapping of optical beams. *Physical review letters*, 13(15), 479.
- [13] Barthelemy, A., Maneuf, S., & Froehly, C. (1985). Propagation soliton et auto-confinement de faisceaux laser par non linearité optique de Kerr. *Optics communications*, 55(3), 201-206.
- [14] Picozzi, A., Pitois, S., & Millot, G. (2008). Spectral incoherent solitons: a localized soliton behavior in the frequency domain. *Physical review letters*, 101(9), 093901.
- [15] Agrawal, G. P. (2000). Nonlinear fiber optics. In *Nonlinear Science at the Dawn of the 21st Century* (pp. 195-211). Springer, Berlin, Heidelberg.
- [16] Hasegawa, A. (1989). Optical solitons in fibers. In *Optical Solitons in Fibers* (pp. 1-74). Springer, Berlin, Heidelberg.
- [17] Trillo, S., & Torruellas, W. (Eds.). (2013). *Spatial solitons* (Vol. 82). Springer.
- [18] Tomlinson, W. J., Hawkins, R. J., Weiner, A. M., Heritage, J. P., & Thurston, R. N. (1989). Dark optical solitons with finite-width background pulses. *JOSA B*, 6(3), 329-334.

- [19] Zakharov, V. E., & Shabat, A. B. (1973). Interaction between solitons in a stable medium. *Sov. Phys. JETP*, 37(5), 823-828.
- [20] Weiner, A. M., Heritage, J. P., Hawkins, R. J., Thurston, R. N., Kirschner, E. M., Leaird, D. E., & Tomlinson, W. J. (1988). Experimental observation of the fundamental dark soliton in optical fibers. *Physical review letters*, 61(21), 2445.
- [21] Kivshar, Y. S., & Luther-Davies, B. (1998). Dark optical solitons: physics and applications. *Physics reports*, 298(2-3), 81-197.
- [22] Song, Y., Shi, X., Wu, C., Tang, D., & Zhang, H. (2019). Recent progress of study on optical solitons in fiber lasers. *Applied Physics Reviews*, 6(2), 021313.
- [23] De Angelis, C., Santagiustina, M., & Wabnitz, S. (1995). Stability of vector solitons in fiber laser and transmission systems. *Optics communications*, 122(1-3), 23-27.
- [24] Wang, H. Y., Xu, W. C., Cao, W. J., Wang, L. Y., & Dong, J. L. (2012). Experimental observation of bright-dark pulse emitting in an all-fiber ring cavity laser. *Laser Physics*, 22(1), 282-285.
- [25] Boiti, M., Laddomada, C., & Pempinelli, F. (1982). Nonlinear Schrödinger equation, potential nonlinear Schrödinger equation and soliton solutions. *Il Nuovo Cimento A (1965-1970)*, 68(3), 236-248.
- [26] Wabnitz, S., & Daino, B. (1993). Polarization domains and instabilities in nonlinear optical fibers. *Physics Letters A*, 182(2-3), 289-293.
- [27] Pitois, S., Millot, G., & Wabnitz, S. (1998). Polarization domain wall solitons with counterpropagating laser beams. *Physical review letters*, 81(7), 1409.
- [28] Lecaplain, C., Grelu, P., & Wabnitz, S. (2013). Polarization-domain-wall complexes in fiber lasers. *JOSA B*, 30(1), 211-218.
- [29] Hasegawa, A. (1980). Self-confinement of multimode optical pulse in a glass fiber. *Optics letters*, 5(10), 416-417.
- [30] Crosignani, B., & Di Porto, P. (1981). Soliton propagation in multimode optical fibers. *Optics letters*, 6(7), 329-330.
- [31] Crosignani, B., Cutolo, A., & Di Porto, P. (1982). Coupled-mode theory of nonlinear propagation in multimode and single-mode fibers: envelope solitons and self-confinement. *JOSA*, 72(9), 1136-1141.
- [32] Renninger, W. H., & Wise, F. W. (2013). Optical solitons in graded-index multimode fibres. *Nature communications*, 4(1), 1-6.
- [33] Wright, L. G., Renninger, W. H., Christodoulides, D. N., & Wise, F. W. (2015). Spatiotemporal dynamics of multimode optical solitons. *Optics express*, 23(3), 3492-3506.
- [34] Ashkin, A., Boyd, G. D., Dziedzic, J. I., Smith, R. G., Ballman, A. A., Levinstein, J. J., & Nassau, K. (1966). Optically-induced refractive index inhomogeneities in LiNbO₃ and LiTaO₃. *Applied Physics Letters*, 9(1), 72-74.

- [35]Chen, F. S., LaMacchia, J. T., & Fraser, D. B. (1995). Holographic storage in lithium niobate. In *Landmark Papers on Photorefractive Nonlinear Optics* (pp. 33-35).
- [36]Chen, F. S. (1969). Optically induced change of refractive indices in LiNbO₃ and LiTaO₃. *Journal of applied physics*, 40(8), 3389-3396.
- [37]Yeh, P. (1993). *Introduction to photorefractive nonlinear optics* (Vol. 14). Wiley-Interscience.
- [38]Segev, M., Crosignani, B., Yariv, A., & Fischer, B. (1992). Spatial solitons in photorefractive media. *Physical Review Letters*, 68(7), 923.
- [39]Duree Jr, G. C., Shultz, J. L., Salamo, G. J., Segev, M., Yariv, A., Crosignani, B., ... & Neurgaonkar, R. R. (1993). Observation of self-trapping of an optical beam due to the photorefractive effect. *Physical review letters*, 71(4), 533.
- [40]Assanto, G., Peccianti, M., & Conti, C. (2003). Nematicons: optical spatial solitons in nematic liquid crystals. *Optics and photonics news*, 14(2), 44-48.
- [41]Peccianti, M., Conti, C., Assanto, G., De Luca, A., & Umeton, C. (2002). All-optical switching and logic gating with spatial solitons in liquid crystals. *Applied Physics Letters*, 81(18), 3335-3337.
- [42]Coda, V. (2006). *Solitons optiques spatiaux Kerr et photoréfractifs: propriétés fondamentales et application à l'adressage optique* (Doctoral dissertation, Université de Franche-Comté).
- [43]Mollenauer, L. F., & Stolen, R. H. (1984). The soliton laser. *Optics letters*, 9(1), 13-15.
- [44]Haus, H., & Islam, M. (1985). Theory of the soliton laser. *IEEE journal of quantum electronics*, 21(8), 1172-1188.
- [45]Stolen, R. H., Lin, C., & Jain, R. K. (1977). A time-dispersion-tuned fiber Raman oscillator. *Applied Physics Letters*, 30(7), 340-342.
- [46]Lin, C., Stolen, R. H., & Cohen, L. G. (1977). A tunable 1.1- μ m fiber Raman oscillator. *Applied Physics Letters*, 31(2), 97-99.
- [47]Haus, H. A., & Nakazawa, M. (1987). Theory of the fiber Raman soliton laser. *JOSA B*, 4(5), 652-660.
- [48]McLeod, R., Wagner, K., & Blair, S. (1995). (3+ 1)-dimensional optical soliton dragging logic. *Physical Review A*, 52(4), 3254.
- [49]Silberberg, Y. (1990). Collapse of optical pulses. *Optics letters*, 15(22), 1282-1284.
- [50]Eisenberg, H. S., Morandotti, R., Silberberg, Y., Bar-Ad, S., Ross, D., & Aitchison, J. S. (2001). Kerr spatiotemporal self-focusing in a planar glass waveguide. *Physical review letters*, 87(4), 043902.
- [51]Di Trapani, P., Caironi, D., Valiulis, G., Dubietis, A., Danielius, R., & Piskarskas, A. (1998). Observation of temporal solitons in second-harmonic generation with tilted pulses. *Physical review letters*, 81(3), 570.
- [52]Liu, X., Qian, L. J., & Wise, F. W. (1999). Generation of optical spatiotemporal solitons. *Physical review letters*, 82(23), 4631.

- [53]Liu, X., Beckwitt, K., & Wise, F. (2000). Two-dimensional optical spatiotemporal solitons in quadratic media. *Physical Review E*, 62(1), 1328.
- [54]Wise, F., & Di Trapani, P. (2002). The hunt for light bullets-spatiotemporal solitons. *Opt. Photon. News*, 13(2), 28-32.
- [55]Malomed, B. A., Mihalache, D., Wise, F., & Torner, L. (2005). Spatiotemporal optical solitons. *Journal of Optics B: Quantum and Semiclassical Optics*, 7(5), R53.
- [56]Kivshar, Y. S., & Agrawal, G. P. (2003). *Optical solitons: from fibers to photonic crystals*. Academic press.
- [57]Picholle, E., Montes, C., Leycuras, C., Legrand, O., & Botineau, J. (1991). Observation of dissipative superluminous solitons in a Brillouin fiber ring laser. *Physical review letters*, 66(11), 1454.
- [58]Akhmediev, N., & Ankiewicz, A. (2005). Dissipative solitons in the complex Ginzburg-Landau and Swift-Hohenberg equations. In *Dissipative solitons* (pp. 1-17). Springer, Berlin, Heidelberg.
- [59]Akhmediev, N. N., & Ankiewicz, A. (2002). Solitons around us: integrable, Hamiltonian and dissipative systems. In *Optical solitons* (pp. 105-126). Springer, Berlin, Heidelberg.
- [60]Husakou, A. V., & Herrmann, J. (2001). Supercontinuum generation of higher-order solitons by fission in photonic crystal fibers. *Physical Review Letters*, 87(20), 203901.
- [61]Yin, L., Lin, Q., & Agrawal, G. P. (2007). Soliton fission and supercontinuum generation in silicon waveguides. *Optics letters*, 32(4), 391-393.
- [62]Dudley, J. M., Genty, G., & Coen, S. (2006). Supercontinuum generation in photonic crystal fiber. *Reviews of modern physics*, 78(4), 1135.
- [63]Mitschke, F. M., & Mollenauer, L. F. (1986). Discovery of the soliton self-frequency shift. *Optics letters*, 11(10), 659-661.
- [64]Gordon, J. P. (1986). Theory of the soliton self-frequency shift. *Optics letters*, 11(10), 662-664.
- [65]Papacharalampous, I. E., Kevrekidis, P. G., Malomed, B. A., & Frantzeskakis, D. J. (2003). Soliton collisions in the discrete nonlinear Schrödinger equation. *Physical Review E*, 68(4), 046604.
- [66]Stegeman, G. I., & Segev, M. (1999). Optical spatial solitons and their interactions: universality and diversity. *Science*, 286(5444), 1518-1523.
- [67]Shalaby, M., & Barthelemy, A. (1991). Experimental spatial soliton trapping and switching. *Optics letters*, 16(19), 1472-1474.
- [68]Cao, X. D., & Meyerhofer, D. D. (1994). All-optical switching by means of collisions of spatial vector solitons. *Optics letters*, 19(21), 1711-1713.
- [69]Lefort, L., & Barthelemy, A. (1997). All-optical demultiplexing of a signal using collision and waveguiding of spatial solitons. *IEEE Photonics Technology Letters*, 9(10), 1364-1366.
- [70]Torner, L., Mazilu, D., & Mihalache, D. (1996). Walking solitons in quadratic nonlinear media. *Physical review letters*, 77(12), 2455.

- [71]Torner, L., Mihalache, D., Mazilu, D., & Akhmediev, N. N. (1997). Walking vector solitons. *Optics communications*, 138(1-3), 105-108.
- [72]Schiek, R., Baek, Y., Stegeman, G. I., & Sohler, W. (1999). One-dimensional quadratic walking solitons. *Optics letters*, 24(2), 83-85.
- [73]Torruellas, W. E., & Torner, L. (1996). A Game of Billiards with Spatial-solitary Waves in KTP. *Optics and Photonics News*, 7(3), 34.
- [74]Frisquet, B. (2016). Ondes scélérates complexes dans les fibres optiques (Doctoral dissertation, Dijon).
- [75]Shabat, A., & Zakharov, V. (1972). Exact theory of two-dimensional self-focusing and one-dimensional self-modulation of waves in nonlinear media. *Soviet physics JETP*, 34(1), 62.
- [76]Benjamin, T. B., & Feir, J. E. (1967). The disintegration of wave trains on deep-water. *J. Fluid mech*, 27(3), 417-430.
- [77]Benjamin, T. B. (1967). Instability of periodic wavetrains in nonlinear dispersive systems. *Proceedings of the Royal Society of London. Series A. Mathematical and Physical Sciences*, 299(1456), 59-76.
- [78]Zakharov, V. E., & Ostrovsky, L. A. (2009). Modulation instability: the beginning. *Physica D: Nonlinear Phenomena*, 238(5), 540-548.
- [79]Akhmediev, N. N., & Korneev, V. I. (1986). Modulation instability and periodic solutions of the nonlinear Schrödinger equation. *Theoretical and Mathematical Physics*, 69(2), 1089-1093.
- [80]Peregrine, D. H. (1983). Water waves, nonlinear Schrödinger equations and their solutions. *The ANZIAM Journal*, 25(1), 16-43.
- [81]Kuznetsov, E. A. (1977). Solitons in a parametrically unstable plasma. *DoSSR*, 236, 575-577.
- [82]Ma, Y. C. (1979). The perturbed plane-wave solutions of the cubic Schrödinger equation. *Studies in Applied Mathematics*, 60(1), 43-58.
- [83]Baronio, F. (2017). Akhmediev breathers and Peregrine solitary waves in a quadratic medium. *Optics Letters*, 42(9), 1756-1759.
- [84]Chabchoub, A., Kibler, B., Dudley, J. M., & Akhmediev, N. (2014). Hydrodynamics of periodic breathers. *Philosophical Transactions of the Royal Society A: Mathematical, Physical and Engineering Sciences*, 372(2027), 20140005.
- [85]Kibler, B., Fatome, J., Finot, C., Millot, G., Genty, G., Wetzels, B., ... & Dudley, J. M. (2012). Observation of Kuznetsov-Ma soliton dynamics in optical fibre. *Scientific reports*, 2, 463.
- [86]Kibler, B., Fatome, J., Finot, C., Millot, G., Dias, F., Genty, G., ... & Dudley, J. M. (2010). The Peregrine soliton in nonlinear fibre optics. *Nature Physics*, 6(10), 790-795.
- [87]Hammani, K., Wetzels, B., Kibler, B., Fatome, J., Finot, C., Millot, G., ... & Dudley, J. M. (2011). Spectral dynamics of modulation instability described using Akhmediev breather theory. *Optics letters*, 36(11), 2140-2142.

- [88]Igarashi, K., Souma, D., Tsuritani, T., & Morita, I. (2014). Performance evaluation of selective mode conversion based on phase plates for a 10-mode fiber. *Optics express*, 22(17), 20881-20893.
- [89]Lemaire, P. J. (1993, September). Hydrogen-induced losses and their effects on optical fiber reliability. In *Fiber Optics Reliability and Testing: A Critical Review* (Vol. 10272, p. 1027207). International Society for Optics and Photonics.
- [90]Ohashi, M., Shiraki, K., & Tajima, K. (1992). Optical loss property of silica-based single-mode fibers. *Journal of Lightwave Technology*, 10(5), 539-543.
- [91]Liu, W. J., Tian, B., Xu, T., Sun, K., & Jiang, Y. (2010). Bright and dark solitons in the normal dispersion regime of inhomogeneous optical fibers: Soliton interaction and soliton control. *Annals of Physics*, 325(8), 1633-1643.
- [92]Birks, T. A., Knight, J. C., & Russell, P. S. J. (1997). Endlessly single-mode photonic crystal fiber. *Optics letters*, 22(13), 961-963.
- [93]Delahaye, F., Maurel, M., Chafer, M., Amrani, F., Debord, B., Gérôme, F., & Benabid, F. (2018, May). Double-clad hypocycloid core-contour Kagome hollow-core photonic crystal fiber. In *CLEO: Applications and Technology* (pp. JTh2A-97). Optical Society of America.
- [94]Song, Y., Shi, X., Wu, C., Tang, D., & Zhang, H. (2019). Recent progress of study on optical solitons in fiber lasers. *Applied Physics Reviews*, 6(2), 021313.

Chapter II. Solitons in quadratic media

II.1. Light propagation and three-wave mixing in quadratic medium

In this chapter, I will focus my attention to quadratic media such as type II nonlinear bulk Potassium Titanyl Phosphate (KTP) crystals or periodically poled lithium niobate (PPLN) [1]. One can see the quadratic nonlinear material, with $\chi^{(2)}$ susceptibility, as a frequency mixer, where an idler wave at a pulsation ω_3 can be generated by a signal and pump at ω_1 and ω_2 .

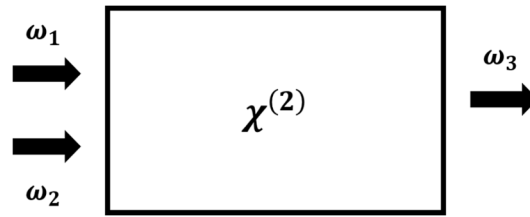


Figure 16: Three-wave mixing process in a quadratic nonlinear medium with $\chi^{(2)}$ susceptibility.

The nonlinearity of that medium (which provides a relatively high susceptibility) comes mainly from its molecular crystal lattice arrangement and from the nature of the involved atoms. In this way, only the second order nonlinear susceptibility is usually considered, thus, the nonlinear polarization $\overline{P_{NL}}$ from equation (1.8) can be simplified as:

$$\overline{P_{NL}} = \epsilon_0 \chi^{(2)} \overline{E}^2 \quad (2.1)$$

Nevertheless, quadratic media can also support a high third order nonlinearity, which can counterbalance or increase the effects of the second order one. In some particular cases, as in high phase-mismatch and high input peak power, the Kerr nonlinearity can play a significant role and drastically disturb the $\chi^{(2)}$ process [2] [3].

From the equation seen in the previous chapter, we can calculate the nonlinear polarization for a pure quadratic nonlinear media, considering the monochromatic field: $E(t) = E_0 \cos(\omega t)$.

E_0 and ω are respectively the amplitude of the electric field and its pulsation:

$$P_{NL}(t) = \frac{1}{2} \epsilon_0 \chi^{(2)} E_0 \cos(2\omega t) + \frac{1}{2} \epsilon_0 \chi^{(2)} E_0 \quad (2.2)$$

For simplicity, I consider the real values of $E(t)$ and $P_{NL}(t)$ in the equations (2.2) - (2.4). The others equations will be instead referred to complex envelopes as in Chapter I.

In the non-degenerated case, two different injected optical frequencies, with pulsations ω_1 and ω_2 ($\omega_1 \neq \omega_2$), are considered:

$$E(t) = E_1 \cos(\omega_1 t) + E_2 \cos(\omega_2 t) \quad (2.3)$$

Leading to the following nonlinear polarization:

$$P_{NL}(t) = \epsilon_0 \chi^{(2)} (E_1 \cos(\omega_1 t) + E_2 \cos(\omega_2 t))^2 \quad (2.4)$$

By developing the equation (2.4), it is possible to extract nonlinear processes from the solutions terms. They are listed in the following table:

Nonlinear polarization terms	Nonlinear processes
$\frac{1}{2} \epsilon_0 \chi^{(2)} (E_1^2 + E_2^2)$	Optical Rectification
$\frac{1}{2} \epsilon_0 \chi^{(2)} (E_1^2 \cos(2\omega_1 t) + E_2^2 \cos(2\omega_2 t))$	Second Harmonic Generation $2\omega_1$ or $2\omega_2$
$\epsilon_0 \chi^{(2)} E_1 E_2 \cos[(\omega_1 + \omega_2)t]$	Sum Frequency Generation $\omega_1 + \omega_2$
$\epsilon_0 \chi^{(2)} E_1 E_2 \cos(\omega_1 - \omega_2 t)$	Difference Frequency Generation $ \omega_1 - \omega_2 $

Table 1: Quadratic nonlinear processes.

Equation (2.2) is composed by two parts. The first one oscillates at the pulsation 2ω that is twice the frequency of the fundamental wave. This part is physically at the base of *Second Harmonic Generation* (SHG). A first observation of optical SHG was made in quartz material by P.A. Franken *et al.* in 1961 [4]. The next year, additional experimental demonstrations in other materials like potassium dihydrogen phosphate [5] [6] or triglycine sulfate [7] were reported.

These observations quickly led to the publication of theoretical papers on the SHG in 1962, written by N. Bloembergen *et al.* [8] and J.A. Armstrong *et al.* [9]. Seven years later, in 1969, G. S. Agrawal made a quantum approach of the SHG phenomenon [10].

Surprisingly, the SHG can also be observed in glass. The most used method for SHG in glass is called poling process. It consists in creating or inducing a $\chi^{(2)}$ susceptibility in a glass, by local modification of its molecular structure (using the light itself or a static electric field). Thus, frequency doubling was performed, in 1986, in glass fibers [11], and then in oxide glasses almost a decade later [12] [13] [14] and in non-oxide glasses, in 2001 [15]. Poling was also used by C. Fiorini *et al.* to observe SHG in polymer, in 1997 [16].

A nonlinear process, visible on Table 1, is independent from the pulsation ω . It is well known as *optical rectification*, firstly discovered by M. Bass *et al.* in 1962 [17]. The optical electromagnetic wave is then converted into a DC electric current similar to the electro-optical effect. Based on that process, one can create terahertz radiation by using femtosecond laser pulses [18] [19].

In a quadratic nonlinear medium, three waves can interact. These three waves are nonlinearly coupled one each other. From the equations (1.10) and (2.1), it is now possible to write the coupled evolution equations for the three waves involved in the mixing [1]:

$$\begin{aligned}\frac{\partial \Psi_1}{\partial z} &= i \frac{\omega_1}{n_1 c} d_{eff} \Psi_3 \Psi_2^* e^{i\Delta k z} \\ \frac{\partial \Psi_2}{\partial z} &= i \frac{\omega_2}{n_2 c} d_{eff} \Psi_3 \Psi_1^* e^{i\Delta k z} \\ \frac{\partial \Psi_3}{\partial z} &= i \frac{\omega_3}{n_3 c} d_{eff} \Psi_1 \Psi_2 e^{-i\Delta k z}\end{aligned}\tag{2.5}$$

n_1 , n_2 and n_3 are respectively the effective refractive index of the three mixed waves in the quadratic nonlinear process.

k_1 , k_2 and k_3 are the wave vectors. $\Delta k = k_3 - k_1 - k_2$ is the phase mismatch among these waves. d_{eff} is the effective nonlinearity tensor, calculated from the second-order susceptibility.

The $\chi^{(2)}$ susceptibility is a third rank tensor with 27 terms (3x3x3) because three waves are involved in the quadratic nonlinear process, and each wave interacts with the others [1]:

$$\chi^{(2)} = \begin{bmatrix} \chi_{xxx} & \chi_{xyy} & \chi_{xzz} & \chi_{xyz} & \chi_{xxz} & \chi_{xxy} & \chi_{xzy} & \chi_{xzx} & \chi_{xyx} \\ \chi_{yxx} & \chi_{yyy} & \chi_{yzz} & \chi_{yyz} & \chi_{yxz} & \chi_{yyx} & \chi_{yzy} & \chi_{yzx} & \chi_{yyx} \\ \chi_{zxx} & \chi_{zyy} & \chi_{zzz} & \chi_{zyz} & \chi_{zxx} & \chi_{zxy} & \chi_{zzy} & \chi_{zzx} & \chi_{zyx} \end{bmatrix} \quad (2.6)$$

The optical frequencies used in this thesis are far from the material resonance, so no energy is stored in the molecular structure, and the response between the optical field and the molecular polarization is quasi-instantaneous. It is then possible to permute frequencies if the associated polarizations are also permuted [1]. The tensor is then reduced to 18 terms:

$$\chi^{(2)} = \begin{bmatrix} \chi_{xxx} & \chi_{xyy} & \chi_{xzz} & \chi_{xyz} & \chi_{xxz} & \chi_{xxy} \\ \chi_{yxx} & \chi_{yyy} & \chi_{yzz} & \chi_{yyz} & \chi_{yxz} & \chi_{yyx} \\ \chi_{zxx} & \chi_{zyy} & \chi_{zzz} & \chi_{zyz} & \chi_{zxx} & \chi_{zxy} \end{bmatrix} \quad (2.7)$$

From the following tensor, it is now possible to calculate d_{eff} :

$$d_{eff} = e_3 \cdot \frac{1}{2} \chi^{(2)} \cdot e_1 e_2 \quad (2.8)$$

Where e_1 , e_2 and e_3 are the unit polarization vectors of the three coupled waves respectively. With the Kleinman approximation [1], it is possible to reduce further the number of terms in the effective nonlinearity tensor if the quadratic material is, for example, isotropic, uniaxial, biaxial.

II.2. Importance of the phase matching on the three-wave mixing process

In order to get energy exchange between the three waves, one must respect the phase relation among each wave. A proper way to mathematically represent it is to consider the phase mismatch factor (Δk) reported in the equation (2.5). When the phase mismatch is equal to zero (phase matching), the nonlinear mixing process i. e. the frequency conversion reaches the maximum efficiency.

By integrating $\frac{\partial \Psi_3}{\partial z}$ on the total length L of our nonlinear material, we obtain:

$$I_3(L) \propto I_1(0)I_2(0) \text{sinc}^2\left(\frac{\Delta k L}{2}\right); \text{sinc}(x) = \frac{\sin(x)}{x} \quad (2.9)$$

This equation is relevant for the weak conversion regime, meaning that the generated intensity I_3 is relatively low in regards to the injected intensities I_1 and I_2 , thus, the generated wave does not significantly deplete the incident wave.

In a degenerated case, the equation (2.9) is simplified: $I_1(0) = I_2(0)$ and can be plotted as in the following Figure 17, giving us a Second Harmonic (SH) conversion function of the phase matching in nonlinear quadratic medium. The width of the central peak and the position of the zeros are determined by $\frac{\Delta kL}{2}$, and in order to characterize the phase detuning regardless of the value of L, it is usual to express this quantity as multiple of π .

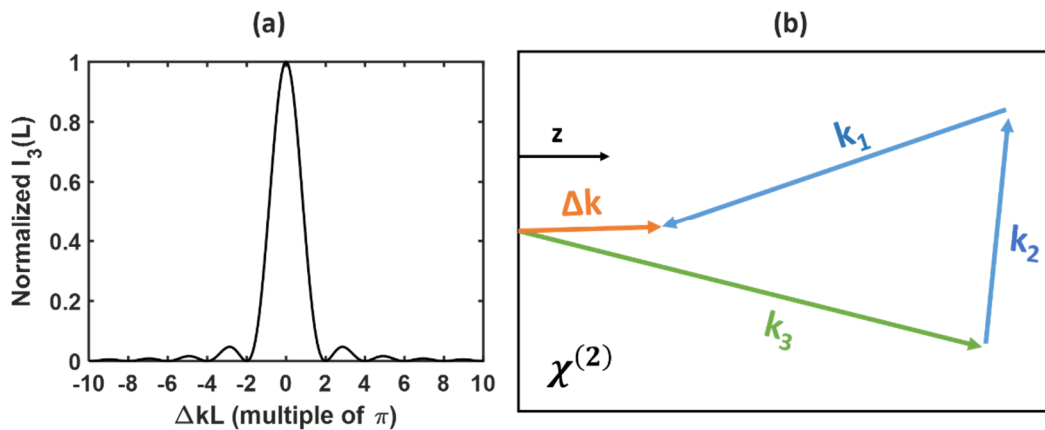


Figure 17: **(a)**-Second harmonic generation versus the nonlinear medium length and the phase mismatch between the waves involved in the process. **(b)**-Phase mismatch representation. Where k_1 and k_2 are the propagating vectors of the depleted waves, and k_3 is the propagating vector of the generated wave.

The Figure 17-(b) shows that in order to get a perfect phase matching, it is necessary to respect the momentum conservation principle: $k_3 = k_1 + k_2$ which goes in pair with the energy conservation principle: $\omega_3 = \omega_1 + \omega_2$.

There are many ways to obtain the phase matching conditions, depending on the crystal type and chemical structure. In isotropic media, chromatic and polarization dispersion make the phase matching process impossible. Therefore, anisotropic media can be used, and crystal orientation or temperature can be managed to control the phase matching conditions.

II.2.1. Birefringence phase matching

Birefringence phase matching is the oldest method to tune SHG efficiency in crystals, and it is well described in many nonlinear optics books [20] [21]. birefringent crystals possess two principal axes, one ordinary (**o**) and one extraordinary (**e**). These principal axes depend on the crystal molecular mesh orientation.

In the case of birefringent crystals, there are two different types of phase matching, **type I** and **type II**.

In **type I** phase matching, the linear polarization directions of ω_1 and ω_2 are parallel to each other, and the linear polarization of ω_3 is orthogonal to the two others.

In **type II** phase matching, the linear polarization directions of ω_1 and ω_2 are orthogonal to each other, and the linear polarization of ω_3 is parallel to one of the two incident waves.

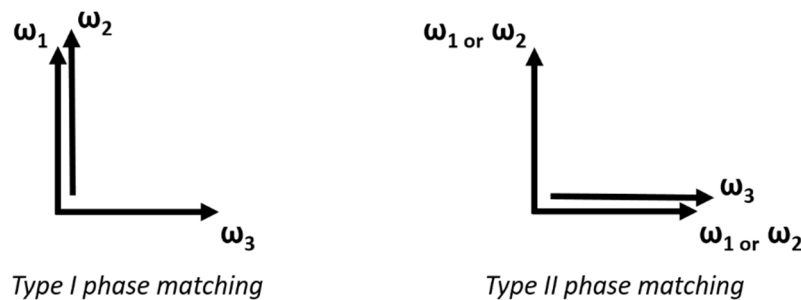


Figure 18: Waves polarization orientations for the two types of phase matching in birefringent crystals.

When waves with a given linear polarization direction are propagating along a birefringent crystal, the polarization state can be separated into two linear polarization components, each one along the principal axes (extraordinary) **e** and (ordinary) **o** of the crystal. This fact may lead to spatial and temporal walk-offs: the beam at the output of the crystal will drift away from the wave vector direction in the spatial case, and delays between waves will occur in temporal domain.

In **type II** phase matching, the incident wave has polarization components along the two principal axes **e** and **o**. Thus, the waves travel along two different optical paths i. e. with two different directions. This spatial walk-off can drastically limit the nonlinear conversion and introduce spatial distortion on the converted wave.

In **type I** phase matching, the incident waves are polarized along an unique principal axis (it can either be **e** or **o**). The waves travel then along one optical path. No spatial walk-off occurs between the incident waves; the generated third wave will propagate through a different optical path since its polarization orientation will be orthogonal to those of the incident waves. Waves propagation, in both types of crystals, is illustrated in the following Figure 19. In all cases, temporal walk-off occurs and the waves can lose the temporal overlap while propagating in the crystal.

An example of **type I** crystal is the Beta Barium Borate (or BBO) [22], an example of **type II** crystal is the KTP [23]. Despite of the spatial walk-off between both incident waves, the nonlinear coefficient of KTP crystals is generally higher than the coefficient of **type I** BBO [24].

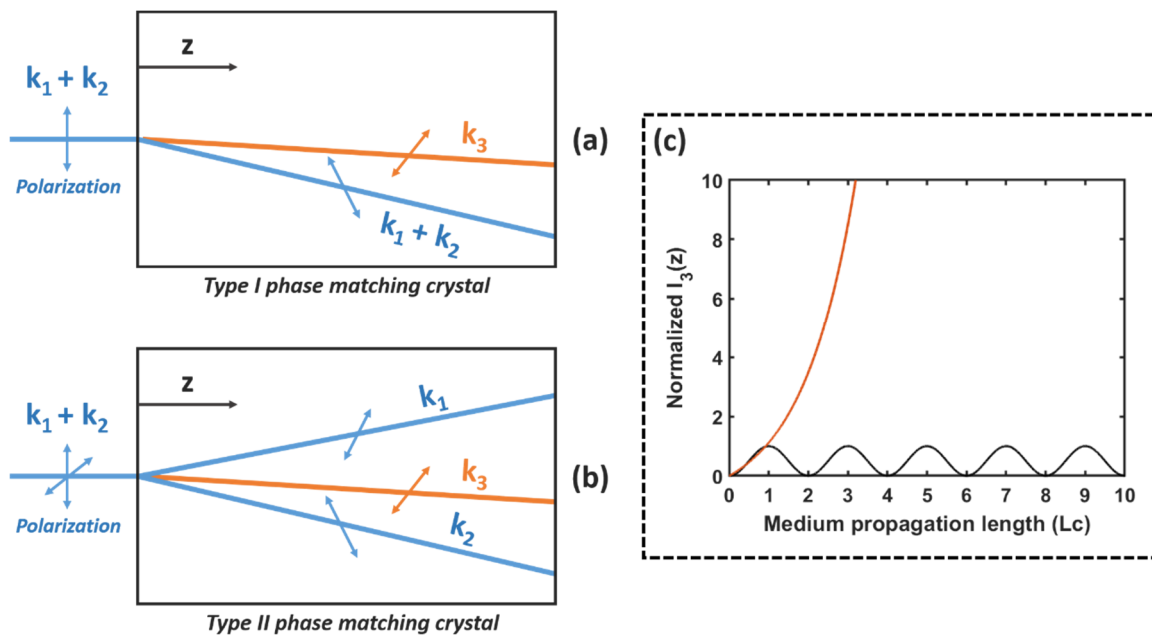


Figure 19: (a)-Example of **type I** phase matching propagating waves. k_1 and k_2 are the propagating vectors of the incident waves, and k_3 is the propagating vector of the converted wave. (b)-Example of **type II** phase matching propagating waves. (c)-Normalized generated wave intensity along the birefringent crystal (**type I** and **type II**). Black curve is in the case of phase mismatch, and orange curve in the case of phase matching.

In Figure 19-(c), we introduce L_c , the coherence length, equal to the propagation length for one of the degenerated incident waves to get a phase displacement of π with respect to the generated third wave.

$$L_c = \frac{\pi}{\Delta k} \quad (2.10)$$

Without birefringence, each time the propagation length reaches L_c , there is an inversion of the energy exchange between the incident waves and the converted wave. As shown in Figure 19-(c) (black curve), if the phase matching condition were not respected in birefringent crystal, the light conversion process would regularly be inverted, and the conversion rate would be very weak after propagation in the crystal.

II.2.2. Quasi-phase-matching

In birefringent crystals, the nonlinear coefficient is orientation dependent. Thus, to exploit the higher nonlinear coefficient, the input pump waves (ω_1 and ω_2) have to follow given directions of propagation. In some cases, no solution can be found, forbidding then the exploitation of that nonlinearity. In order to overcome this difficulty, the quasi-phase-matching technique has been introduced.

Quasi-phase-matching consists in periodically changing the sign of the d tensor every L_c , when the phase difference between the incident and the generated frequencies is equal to π , in order to optimize the energy transfer in the three-wave mixing process. d parameter is a nonlinear coefficient relative to d_{eff} calculated in equation (2.8) [9].

This periodical evolution of the nonlinearity introduces an additional term in the phase matching equation and the new phase matching equation becomes:

$$k_1 + k_2 - k_3 = \frac{\pi}{2\Lambda} \quad (2.11)$$

Λ is the poling period of the PPLN, tunable in temperature (see Figure 20-(a)).

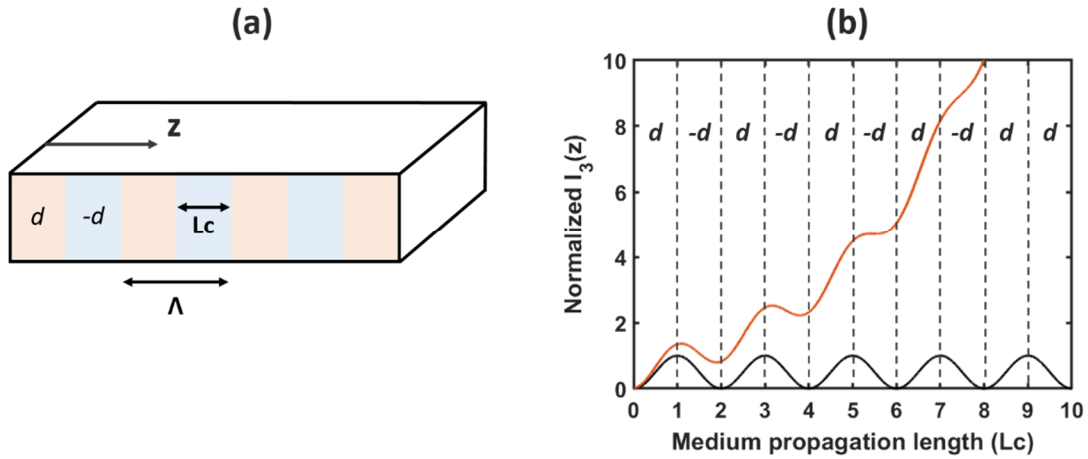


Figure 20: **(a)**-Poled crystal with $\Lambda = 2L_c$ period. **(b)**-Normalized intensity of the generated third wave along the crystal. Black curve is in the case of phase mismatch, and orange curve in the case of quasi-phase-matching.

Comparing the Figure 19-(c) and Figure 20-(b), the third wave intensity generation is higher in the case of pure birefringent phase matching than in quasi-phase-matching process. Nevertheless, quasi-phase-matching allows the use of materials with a higher nonlinear coefficient, leading to a larger nonlinear wave conversion efficiency.

It is also important to note that the incident fundamental radiation is polarized along the extraordinary axis like the generated wave. This case is generally referred as type 0 phase matching process. In that configuration no spatial walk-off between waves exists which contributes to increase the conversion efficiency.

The quasi-phase-matching technique was developed by Armstrong *et al.* in 1962 [9] but the realization was delayed by two decades, due to difficulties in the technological implementation [25].

In my thesis, I used a PPLN crystal designed for quasi-phase-matching at 1064 nm. Thus, the Λ periodicity length was close to $7 \mu\text{m}$ with a nonlinear coefficient d_{eff} of 15 pm/V which is four or five times higher than the one of the type II KTP crystal (3.5 pm/V).

II.3. Solitons generation in quadratic media

Mathematically, the soliton is a specific solution of an integrable model equation [20] [26], however, the term soliton is abusively extended to every case where a self-sustained wave is propagating without deformation, the diffraction or the dispersion being perfectly compensated by the nonlinearity, as in quadratic media.

II.3.1. The history of quadratic solitons

Quadratic solitons are solitonic waveforms generated in $\chi^{(2)}$ materials and composed by two different wavelengths, thus, these solitons are also named bicolor solitons. Karamzin and Sukhorukov theoretically predicted the quadratic soliton existence in 1974 [27], but it took more than two decades to obtain a first experimental demonstration [28] [29]. As we can see in Figure 21, Torruellas *et al.* [28] observed a quadratic spatial soliton at the Fundamental Frequency (FF). He launched a 20 μm -waist infrared beam (see Figure 21-(a)) in a 1 cm-long KTP. At low input light intensity, the diffraction was dominant, leading to the broadening of the beam at the output of the crystal (see Figure 21-(b)). When the nonlinear length compensated the diffraction length (for an input intensity value higher than 10 GW/cm^2), the 12.5 μm -waist soliton was generated and visible at the output of the KTP crystal (see Figure 21-(c)). This 2D spatial soliton was observed on phase matching and small phase mismatch (positive or negative) conditions. Thus, solitons are able to keep their spatial shape unchanged while propagating along multiple diffraction lengths (see Figure 22).

1D quadratic solitons were also observed in a planar LiNbO_3 crystal waveguide by R. Schiek *et al.* [29]. Soliton collisions in quadratic nonlinear materials were studied later in 1D spatial domain [30] [31] and 2D spatial domain [32]. 2D quadratic spatiotemporal soliton collision was also investigated in 2000 by Liu *et al.* [33]. Liu's works come in parallel to their researches on light bullets generation.

The first SHG soliton, generated by using quasi-phase-matching technic, was reported in 1999 by B. Bourliaguet *et al.* in a PPLN [34]. This spatial 2D soliton was generated with an input pump intensity of 1 GW/cm^2 , ten times lower than the soliton generation intensity threshold in Torruellas experiments, using birefringent media [28] (see Figure 21).

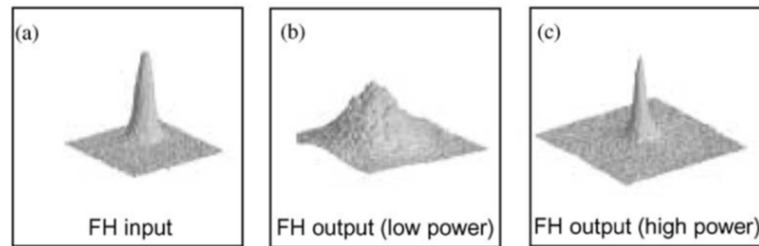


Figure 21: Quadratic soliton observation made by Torruellas [28]. **(a)**-The input beam. **(b)**-The output beam at low input light intensity. **(c)**-The output beam at high input intensity (more than 10 GW/cm^2). All of these images are at the fundamental frequency.

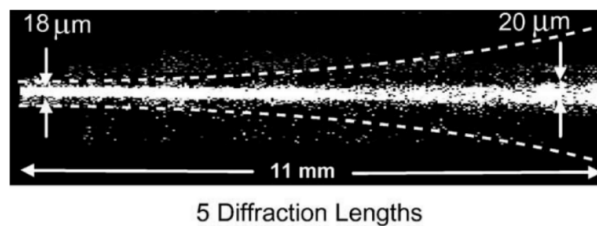


Figure 22: Quadratic soliton propagation in a KNbO_3 crystal. The dashed lines are the simulation of the beam diffraction at low intensity [35] [36] [37].

Beyond the simple observation of a quadratic spatial soliton propagation, interactions between these two colors solitons allowed the demonstration of multiple solitons-like waveforms generation [38], spatial collision between those waveforms [39], walking soliton [40], spatial steering [41], and spiraling [42], which are interesting behaviors for biomedical imaging and all-optical computing for example.

II.3.2. The cascading effect

In order to get a mathematical model of the soliton propagation, while propagating in $\chi^{(2)}$ susceptibility material, one can consider phase mismatch condition, where regular energy exchange between the FF and the SH waves occurs and creates a nonlinear phase shift, which in turn compensates the linear one generated through the propagation. This process is called cascading effect.

Thus, an analytical explanation of the cascading effect can be given, from the following dimensionless equations, for bright spatial solitons generation in slab (1D) type I waveguide (see A. V. Buryak and Y. S. Kivshar article [43] for more details):

$$i\frac{\partial\Psi_{FF}}{\partial z} + \frac{\partial^2\Psi_{FF}}{\partial x^2} - \Psi_{FF} + \Psi_{SH}\Psi_{FF}^* = 0 \quad (2.12)$$

$$i\sigma\frac{\partial\Psi_{SH}}{\partial z} - i\delta\frac{\partial\Psi_{SH}}{\partial x} + \frac{\partial^2\Psi_{SH}}{\partial x^2} - \alpha\Psi_{SH} + \frac{1}{2}\Psi_{FF}^2 = 0 \quad (2.13)$$

With: $\alpha \equiv \sigma(2 + \frac{\Delta k L_d}{\beta})$.

In these equations, Ψ_{FF} is the envelope of the waves at the FF (degenerate case), and Ψ_{SH} is the envelope of the wave at the SH. σ is the modal diffraction ratio, L_d is the diffraction length of the material, β is proportional to the phase velocity shift, induced by nonlinearity, and δ is proportional to the walk-off in the material. z is the propagation coordinate, normalized by L_d .

For a large positive Δk , $\alpha \gg 1$ and the wave equation from (2.13) is reduced to:

$$\Psi_{SH} \approx \frac{\Psi_{FF}^2}{2\alpha} \quad (2.14)$$

In this way, equation (2.12) becomes the following spatial NLSE [44]:

$$i\frac{\partial\Psi_{FF}}{\partial z} + \frac{\partial^2\Psi_{FF}}{\partial x^2} - \Psi_{FF} + \frac{1}{2\alpha}|\Psi_{FF}|^2\Psi_{FF} = 0 \quad (2.15)$$

When the diffraction is limited to one transverse dimension only, this equation is integrable and admits then precise soliton solutions as in Kerr medium.

In these newly stable generated two-color solitons, the SH will have a lower amplitude than the FF, in this cascading limit. Moreover, even for a weak Δk and α , quadratic solitons may exist, but this time the FF will have an amplitude comparable to that of the SH (see Figure 23 for comparison), and the soliton may be unstable [45] [46].

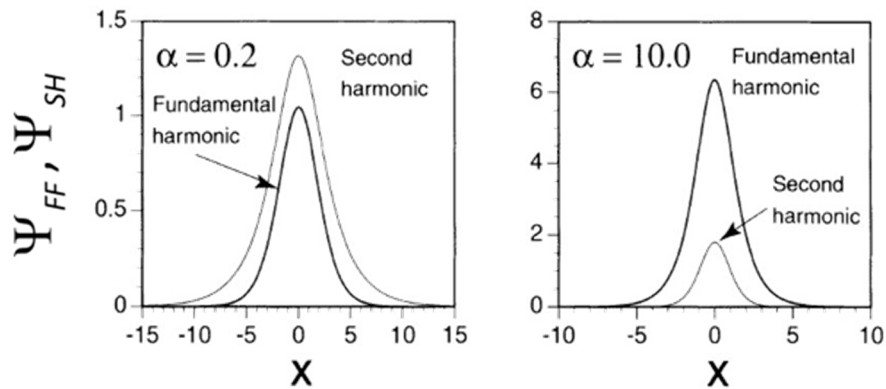


Figure 23: Two colors quadratic solitons, for weak Δk (left) and large Δk (right), from [43].

These analytic solutions assume that the FF and the SH are both present from the beginning of the propagation. Moreover, numerical analysis led by S. Carrasco *et al.* [47] showed that it was possible to observe stable solitons by injecting only the FF in the crystal.

And what happens close to phase matching?

It is important to note that a periodical energy exchange between the FF and the SH is only theoretically possible for $\Delta k \neq 0$.

Moreover, the notion of perfect phase matching can be defined rigorously only for a non-diffractive monochromatic plane wave. The use of short pulses (broad spectrum) with finite spatial dimensions (i. e. with a diffraction length of the beam lower than the crystal length) does not allow to rigorously obtain perfect phase matching. Some wavelengths, present in the pulse spectrum, are then slightly out of phase, when the initial beam starts to diffract.

Thus, we could consider that the case of strict phase matching condition is never respected in the experiments and that quadratic soliton is always obtained, for a weak or large Δk .

Additionally to these informations, in exact phase matching conditions, an analytical solution of a 1+1D soliton in quadratic media was given in [27], for a single value of a global parameter.

II.3.3. Modulation instability and non-zero background solitons in quadratic media

As we saw before, MI is a periodical deformation of wave trains initialized by a weak modulation on a continuous wave propagating in a nonlinear medium. In 1967, Benjamin and Feir wrote a full theory on MI in deep water [48]. Optical MI was mostly studied in $\chi^{(3)}$ susceptibility materials as the silica optical fibers [49], and used to generate spatiotemporal light bullet [50] or optical vortex [51].

Quadratic MI was theoretically predicted and studied by P. Ferro & S. Trillo in 1995 [52] [53] as a phase modulation effect. The proper calculation of MI on top of FF and SH exchanging energy has been solved in 1997 by S. Trillo and S. Wabnitz [54]. The same year [55], Fuerst *et al.* launched an elliptic pump beam through a crystal; while the ellipticity ratio was of 1:8 (1D configuration), they observed a perfectly round soliton at the output of the nonlinear material. The same year, they observed that, while increasing further the pump power, the single soliton split into a regular range of solitons, and their number increased with the pump power [38]. This multiple solitons generation was analyzed further and Fuerst *et al.* [38] made the following conclusion: the spatial solitons array analyzed in the previous paper were the result of a spatial MI, generated by noise in a quadratic nonlinearity material. In this way, Fuerst *et al.* [38] experimentally observed for the first time 1D MI in $\chi^{(2)}$ susceptibility materials. All of these 1D experiments were realized in bulk crystals, and one must wait 2001 to see the MI experiments in quasi-phase-matching conditions, led by J.F. Corney and O. Bang [56].

The first MI in both transverse dimensions (2D MI) was experimentally observed by M. Delqué *et al.* in 2011 [57]. In order to obtain such results, they launched a 500 μm -wide large collimated beam into a KTP crystal, and observed at high power the beam breakup into an important number of self-focused light spots after propagation in the crystal (Figure 24-(a,c)). They analyzed the spatial spectrum of this light pattern, and observed in Fourier domain a sum of symmetrical rings at low frequencies, with a symmetry disappearance at higher frequencies (Figure 24-(b,d)). This particular spectral behavior confirmed that the beam breakup into a solitons pattern observed in both transversal dimensions was initiated by 2D MI.

It is also important to note that F. Baronio predicted the existence of the Peregrine soliton and the Akhmediev breathers in quadratic materials on MI background [58]. Two years later, R.

Schiek and F. Baronio showed experimental spatial 1D Akhmediev breathers in $\chi^{(2)}$ media [59].

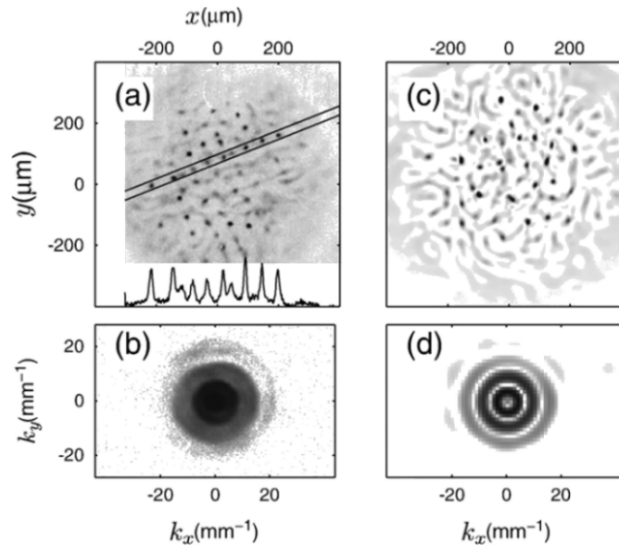


Figure 24: 2D MI observed by M. Delqué *et al.* [57]. **(a)**-Experimental results (10 MW peak power) and **(b)**- Corresponding spatial spectrum. **(c)**-Simulation (10 MW peak power) and **(d)**-Corresponding spatial spectrum.

II.3.4. Walk-off compensation

Since the very early experiments on quadratic soliton, led by Torner *et al.* in 1995 [60], it is well known that spatial walk-off occurring in birefringent crystals has an important impact on these types of solitons.

The walk-off effect was compensated in 1995 by Torruellas *et al.* [28], using soliton generation. Later, the same author observed a soliton switching at the output face of a KTP type II crystal, by controlling the imbalance of the pump components, between the e and o axes (see Figure 25) [63]. In 1998, Schiek *et al.* [31] showed how the spatial walk-off varies upon the input angles and material temperature, in a 1D spatial soliton experiment. This soliton displacement came in parallel to the SH displacement when the FF pump energy balance between the crystal neutral axes was inverted.

L. Torner *et al.* proved the existence of walking solitons [61], by demonstrating that special solutions of stationary solitons could exist with walk-off or group velocity difference between all the waves involved in cascading effect. By controlling these parameters, they managed to cancel the mutual trapping effect between SH and FF waves in cascading effect process, for

some specific propagation length values, allowing the transversal displacement, or the time delay of the stationary solitons after propagating in the quadratic nonlinearity material. Figure 26 shows the spatial walking soliton results by L. Torner *et al.* [40]. In these experiments, light was injected in the crystal with specific tilt values to control the trapping between the FF (ω) and the SH (2ω) waves. Torner's research on quadratic walking solitons followed previous works led by J.M. Soto-Crespo *et al.* [62] on walking solitons in highly birefringent optical fibers.

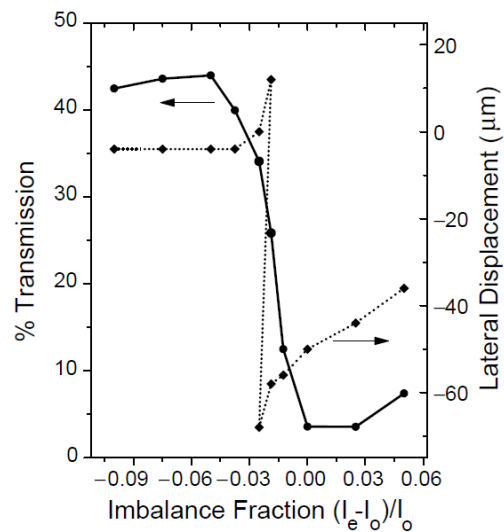


Figure 25: Soliton spatial switching obtained by Torruellas *et al.* [63]. They launched a 20 GW/cm² pump into a 1 cm KTP crystal. The solid curve shows the output light transmission at the fundamental frequency through a 30 μm aperture (numerical analysis), function of the imbalance between e and o crystal neutral axes. The dashed curve shows the output SH position.

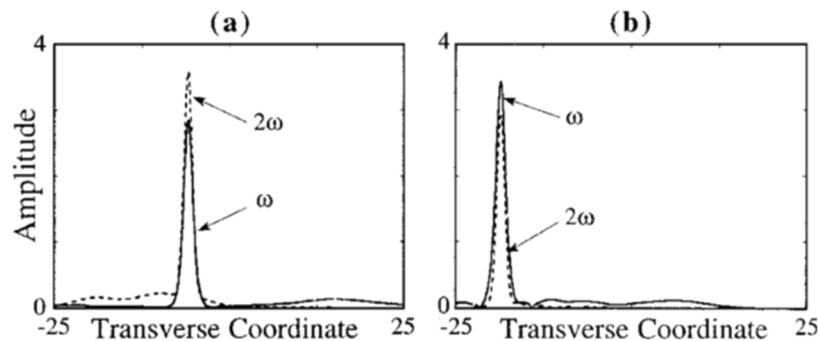


Figure 26: A quadratic spatial walking soliton by Torner *et al.* [40]. **(a)**-Without injection tilt. **(b)**-With injection tilt.

Conclusion – Chapter II

In this chapter, I illustrated the process of three-wave mixing in quadratic crystals, and the different methods to optimize SHG by using type I, type II, or type 0 phase matching processes.

I also summarized some of the most salient experiments on quadratic solitons and explained the mechanism of self-trapped beam in the case of cascading regime, which occurs at phase mismatch conditions. I summarized the results published on quadratic MI and underlined the spatial walk-off compensation in bicolor soliton experiments.

In the following part of the manuscript, I present some examples of ephemeral 2D self-trapping in KTP crystal, which leads to the appearance and disappearance of a 2D quadratic soliton.

Bibliography – Chapter II

- [1] Smith, A. V. (2018). Crystal nonlinear optics: with SNLO examples. AS-Photonics.
- [2] Liu, X., Qian, L. J., & Wise, F. W. (1999). Generation of optical spatiotemporal solitons. *Physical review letters*, 82(23), 4631.
- [3] Krupa, K., Baronio, F., Conforti, M., Trillo, S., Tonello, A., & Couderc, V. (2014). Zero focusing via competing nonlinearities in beta-barium-borate crystals. *Optics letters*, 39(4), 925-928.
- [4] Franken, E. P., Hill, A. E., Peters, C. W., & Weinreich, G. (1961). Generation of optical harmonics. *Physical Review Letters*, 7(4), 118.
- [5] Giordmaine, J. A. (1962). Mixing of light beams in crystals. *Physical Review Letters*, 8(1), 19.
- [6] Maker, P. D., Terhune, R. W., Nisenoff, M., & Savage, C. M. (1962). Effects of dispersion and focusing on the production of optical harmonics. *Physical review letters*, 8(1), 21.
- [7] Bass, M., Franken, P. A., Hill, A. E., Peters, C. W., & Weinreich, G. (1962). Optical mixing. *Physical Review Letters*, 8(1), 18.
- [8] Bloembergen, N., & Pershan, P. S. (1962). Light waves at the boundary of nonlinear media. *Physical review*, 128(2), 606.
- [9] Armstrong, J. A., Bloembergen, N., Ducuing, J., & Pershan, P. S. (1962). Interactions between light waves in a nonlinear dielectric. *Physical review*, 127(6), 1918.
- [10] Agarwal, G. S. (1969). Quantum theory of second harmonic generation. *Optics Communications*, 1(3), 132-134.
- [11] Österberg, U., & Margulis, W. (1986). Dye laser pumped by Nd: YAG laser pulses frequency doubled in a glass optical fiber. *Optics letters*, 11(8), 516-518.
- [12] Driscoll, T. J., & Lawandy, N. M. (1994). Optically encoded second harmonic generation in bulk silica-based glasses. *JOSA B*, 11(2), 355-371.
- [13] Nageno, Y., Kyung, J. H., & Lawandy, N. M. (1995). Compositional dependence of optically encoded second harmonic generation in pure binary lead-silicate and ternary barium borosilicate glasses. *Optics letters*, 20(21), 2180-2182.
- [14] Si, J., Kitaoka, K., Qiu, J., Mitsuyu, T., & Hirao, K. (1999). Optically encoded second harmonic generation in germanosilicate glass by a femtosecond laser. *Optics letters*, 24(13), 911-913.
- [15] Lopez-Lago, E., Couderc, V., Griscom, L., Smektala, F., & Barthélémy, A. (2001). All-optical poling of a chalcogenide glass. *Optical Materials*, 16(4), 413-416.
- [16] Fiorini, C., Charra, F., Nunzi, J. M., & Raimond, P. (1997). Quasi-permanent all-optical encoding of noncentrosymmetry in azo-dye polymers. *JOSA B*, 14(8), 1984-2003.
- [17] Bass, M., Franken, P. A., Ward, J. F., & Weinreich, G. (1962). Optical rectification. *Physical Review Letters*, 9(11), 446.

- [18]Yang, K. H., Richards, P. L., & Shen, Y. R. (1971). Generation of far-infrared radiation by picosecond light pulses in LiNbO₃. *Applied Physics Letters*, 19(9), 320-323.
- [19]Lee, Y. S., Meade, T., Perlin, V., Winful, H., Norris, T. B., & Galvanauskas, A. (2000). Generation of narrow-band terahertz radiation via optical rectification of femtosecond pulses in periodically poled lithium niobate. *Applied Physics Letters*, 76(18), 2505-2507.
- [20]Shen, Y. R. (1984). *The principles of nonlinear optics*. New York.
- [21]Dmitriev, V.G., Gurzadyan, G.G., Nikogosyan, D.N., 1999. *Handbook of Nonlinear Optics*, 3rd Edition. Springer, Berlin.
- [22]Nikogosyan, D. N. (1991). Beta barium borate (BBO). *Applied Physics A*, 52(6), 359-368.
- [23]Gagarskiy, S., Grechin, S., Druzhinin, P., Kato, K., Kochiev, D., Nikolaev, P., & Umemura, N. (2018). Frequency conversion in KTP crystal and its isomorphs. *Crystals*, 8(10), 386.
- [24]Armstrong, D. J., Alford, W. J., Raymond, T. D., & Smith, A. V. (1996). Absolute measurement of the effective nonlinearities of KTP and BBO crystals by optical parametric amplification. *Applied optics*, 35(12), 2032-2040.
- [25]Fejer, M. M., Magel, G. A., Jundt, D. H., & Byer, R. L. (1992). Quasi-phase-matched second harmonic generation: tuning and tolerances. *IEEE Journal of quantum electronics*, 28(11), 2631-2654.
- [26]Agrawal, G. P. (2000). *Nonlinear fiber optics*. In *Nonlinear Science at the Dawn of the 21st Century* (pp. 195-211). Springer, Berlin, Heidelberg.
- [27]Karamzin, Y. N., & Sukhorukov, A. P. (1974). Nonlinear interaction of diffracted light beams in a medium with quadratic nonlinearity: mutual focusing of beams and limitation on the efficiency of optical frequency converters. *ZhETF Pisma Redaktsiiu*, 20, 734.
- [28]Torruellas, W. E., Wang, Z., Hagan, D. J., VanStryland, E. W., Stegeman, G. I., Torner, L., & Menyuk, C. R. (1995). Observation of two-dimensional spatial solitary waves in a quadratic medium. *Physical review letters*, 74(25), 5036.
- [29]Schiek, R., Baek, Y., & Stegeman, G. I. (1996). One-dimensional spatial solitary waves due to cascaded second-order nonlinearities in planar waveguides. *Physical Review E*, 53(1), 1138.
- [30]Baek, Y., Schiek, R., Stegeman, G. I., Baumann, I., & Sohler, W. (1997). Interactions between one-dimensional quadratic solitons. *Optics letters*, 22(20), 1550-1552.
- [31]Schiek, R., Baek, Y., Stegeman, G., & Sohler, W. (1998). Interactions between one-dimensional quadratic soliton-like beams. *Optical and quantum electronics*, 30(7), 861-879.
- [32]Costantini, B., De Angelis, C., Barthélemy, A., Bourliaguet, B., & Kermene, V. (1998). Collisions between type II two-dimensional quadratic solitons. *Optics letters*, 23(6), 424-426.
- [33]Liu, X., Beckwitt, K., & Wise, F. (2000). Noncollinear generation of optical spatiotemporal solitons and application to ultrafast digital logic. *Physical Review E*, 61(5), R4722.

- [34] Bourliaguet, B., Couderc, V., Barthélémy, A., Ross, G. W., Smith, P. G. R., Hanna, D. C., & De Angelis, C. (1999). Observation of quadratic spatial solitons in periodically poled lithium niobate. *Optics letters*, 24(20), 1410-1412.
- [35] Torner, L., & Stegeman, G. I. (2001). Multicolor solitons. *Optics and Photonics News*, 12(6), 36-39.
- [36] Kivshar, Y. S., & Stegeman, G. I. (2002). Spatial optical solitons. *Optics and Photonics News*, 13(2), 59-63.
- [37] Malendevich, R., Jankovic, L., Polyakov, S., Fuerst, R., Stegeman, G., Bosshard, C., & Gunter, P. (2002). Two-dimensional type I quadratic spatial solitons in KNbO₃ near noncritical phase matching. *Optics letters*, 27(8), 631-633.
- [38] Fuerst, R. A., Baboiu, D. M., Lawrence, B., Torruellas, W. E., Stegeman, G. I., Trillo, S., & Wabnitz, S. (1997). Spatial modulational instability and multisoliton like generation in a quadratically nonlinear optical medium. *Physical review letters*, 78(14), 2756.
- [39] Costantini, B., De Angelis, C., Barthelemy, A., Palma, A. L., & Assanto, G. (1997). Polarization-multiplexed χ (2) solitary-wave interactions. *Optics letters*, 22(18), 1376-1378.
- [40] Torner, L., Mihalache, D., Mazilu, D., Santos, M. C., & Akhmediev, N. N. (1998). Spatial walking solitons in quadratic nonlinear crystals. *JOSA B*, 15(5), 1476-1487.
- [41] Couderc, V., Lago, E. L., Simos, C., & Barthelemy, A. (2001). Experiments in quadratic spatial soliton generation and steering in a noncollinear geometry. *Optics letters*, 26(12), 905-907.
- [42] Simos, C., Couderc, V., Barthélémy, A., & Buryak, A. V. (2003). Phase-dependent interactions between three-wave spatial solitons in bulk quadratic media. *JOSA B*, 20(10), 2133-2141.
- [43] Buryak, A. V., & Kivshar, Y. S. (1995). Solitons due to second harmonic generation. *Physics Letters A*, 197(5-6), 407-412.
- [44] Trillo, S., & Torruellas, W. (Eds.). (2013). *Spatial solitons* (Vol. 82). Springer.
- [45] Pelinovsky, D. E., Buryak, A. V., & Kivshar, Y. S. (1995). Instability of solitons governed by quadratic nonlinearities. *Physical review letters*, 75(4), 591.
- [46] Torner, L., Mihalache, D., Mazilu, D., & Akhmediev, N. N. (1995). Stability of spatial solitary waves in quadratic media. *Optics letters*, 20(21), 2183-2185.
- [47] Carrasco, S., Torner, L., Torres, J. P., Artigas, D., López-Lago, E., Couderc, V., & Barthélémy, A. (2002). Quadratic solitons: Existence versus excitation. *IEEE Journal of selected topics in quantum electronics*, 8(3), 497-505.
- [48] Benjamin, T. B., & Feir, J. E. (1967). The disintegration of wave trains on deep water Part 1. Theory. *Journal of Fluid Mechanics*, 27(3), 417-430.
- [49] Tai, K., Hasegawa, A., & Tomita, A. (1986). Observation of modulational instability in optical fibers. *Physical review letters*, 56(2), 135.
- [50] Liu, X., Beckwitt, K., & Wise, F. (2000). Transverse instability of optical spatiotemporal solitons in quadratic media. *Physical review letters*, 85(9), 1871.

- [51]Kivshar, Y. S., Christou, J., Tikhonenko, V., Luther-Davies, B., & Pismen, L. M. (1998). Dynamics of optical vortex solitons. *Optics Communications*, 152(1-3), 198-206.
- [52]Ferro, P., & Trillo, S. (1995). Periodical waves, domain walls, and modulational instability in dispersive quadratic nonlinear media. *Physical Review E*, 51(5), 4994.
- [53]Trillo, S., & Ferro, P. (1995). Modulational instability in second harmonic generation. *Optics letters*, 20(5), 438-440.
- [54]Trillo, S., & Wabnitz, S. (1997). Dynamic spontaneous fluorescence in parametric wave coupling. *Physical Review E*, 55(5), R4897.
- [55]Fuerst, R. A., Lawrence, B. L., Torruellas, W. E., & Stegeman, G. I. (1997). Beam reshaping by use of spatial solitons in the quadratic nonlinear medium KTP. *Optics letters*, 22(1), 19-21.
- [56]Corney, J. F., & Bang, O. (2001). Modulational instability in periodic quadratic nonlinear materials. *Physical review letters*, 87(13), 133901.
- [57]Delqué, M., Fanjoux, G., Gorza, S. P., & Haelterman, M. (2011). Spontaneous 2D modulation instability in second harmonic generation process. *Optics Communications*, 284(5), 1401-1404.
- [58]Baronio, F. (2017). Akhmediev breathers and Peregrine solitary waves in a quadratic medium. *Optics letters*, 42(9), 1756-1759.
- [59]Schiek, R., & Baronio, F. (2019). Spatial Akhmediev breathers and modulation instability growth-decay cycles in a quadratic optical medium. *Physical Review Research*, 1(3), 032036.
- [60]Torner, L., Torruellas, W. E., Stegeman, G. I., & Menyuk, C. R. (1995). Beam steering by χ (2) trapping. *Optics letters*, 20(19), 1952-1954.
- [61]Torner, L., Mazilu, D., & Mihalache, D. (1996). Walking solitons in quadratic nonlinear media. *Physical review letters*, 77(12), 2455.
- [62]J. M. Soto-Crespo, N. Akhmediev, and A. Ankiewicz, *Phys. Rev. E* 51, 3547 (1995).
- [63]Torruellas, W. E., Assanto, G., Lawrence, B. L., Fuerst, R. A., & Stegeman, G. I. (1996). All-optical switching by spatial walk off compensation and solitary-wave locking. *Applied physics letters*, 68(11), 1449-1451.

Chapter III. Quadratic spatial extreme event

In this chapter, I will discuss the experimental observation of a transient spatiotemporal self-trapping in quadratic crystal that is able to generate several interesting effects such as the quadratic solitons, the beam breaking up to the formation of a nonlinearity induced speckle, and the spectral broadening to a supercontinuum generation.

To introduce some novelty with respect to the large literature already published in this field, I decided to excite the quadratic crystal with a large collimated beam, changing the input pump intensity and polarization, and the crystal phase mismatch. I also considered few different types of crystals in order to experiment with two different schemes to obtain SHG, known as type II and type 0.

III.1. Experimental setup and crystal phase matching conditions

III.1.1. Measurements setup

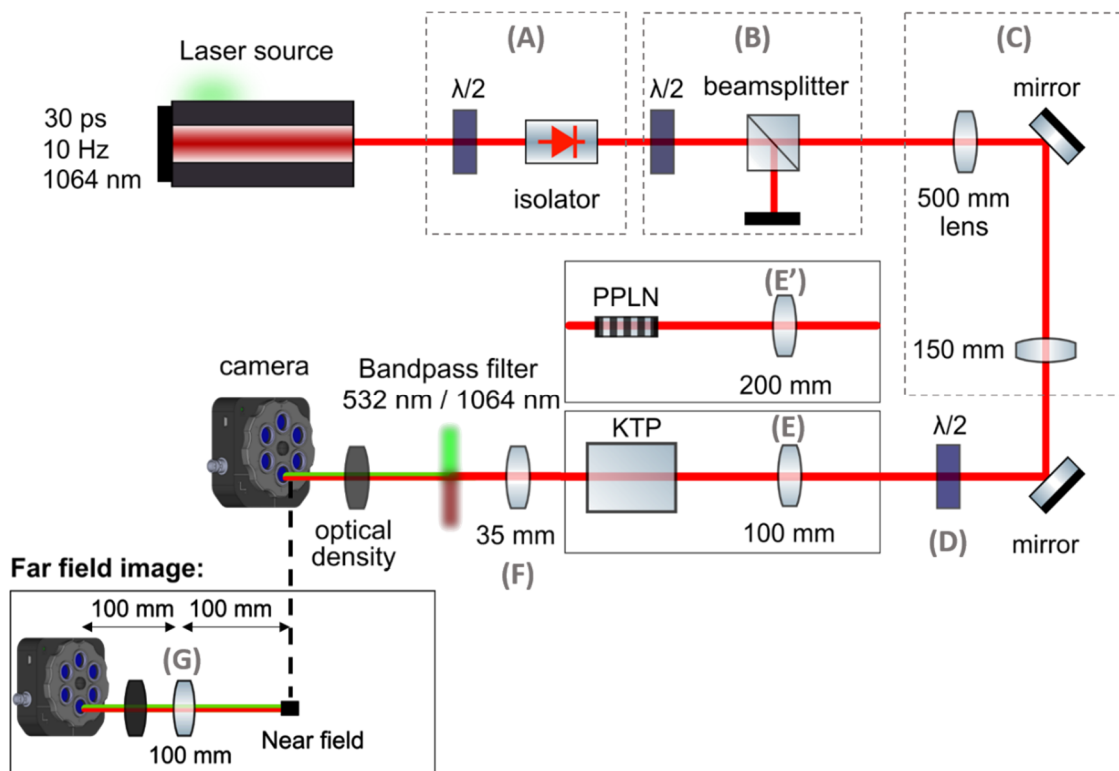


Figure 27: Schematic of the experimental setup for beam spatial studies.

In the following experiments, a Q-switched mode-locked Nd:YAG laser (EKSPLA PL2250 series), delivering 30 ps pulse at a central wavelength of 1064 nm and a 10 Hz repetition rate, has been used to excite some samples of quadratic crystals. The output of the laser was back-reflection protected by means of an isolator **(A)** and sent in a half-wave plate and a polarization beam splitter to control the light intensity **(B)**. I reduced the diameter of the initial Gaussian beam by using an afocal system composed by two lenses with 500 mm and 150 mm focal length respectively **(C)**. The orientation of the linear input State Of Polarization (SOP) of the infrared beam is controlled by a half-wave plate **(D)**. The beam is then injected in the nonlinear crystal. The beam shape at the output of the crystal is spatially characterized by using an infrared + visible camera. The near-field image of the beam at the KTP crystal output face is obtained by using a 35 mm converging lens **(F)**, and analyzed on a BC106N-VIS CCD Thorlabs camera, with a magnification of 4.6. I used the same setup to analyze the near-field image of the beam at the PPLN output face: in that case, the corresponding magnification was 8.4. To measure the far field, I introduced another converging lens **(G)** of 100 mm of focal length.

An autocorrelator and an optical spectrum analyzer can replace the infrared camera to allow the output beam characterization in the temporal and spectral domains.

I used two types of quadratic crystals. The first one is a type II phase matching KTP crystal, manufactured by CASTECH. The crystal was 30 mm long, 8 mm thick, and 8 mm wide. I controlled the phase matching conditions by rotating the crystal within two axes (one vertical and one horizontal) by using a Newport gimbal optic mount (maximum resolution of 0.05°). Thanks to the initial cut of the crystal ($\theta = 90^\circ$, $\Phi = 23.5^\circ$), the phase matching position ($\Delta kL = 0$) is obtained by coupling the beam perpendicularly to the input crystal face. The maximum of SHG is obtained for a SOP of 45° between ordinary and extraordinary neutral axes directions.

The nonlinear coefficient d_{eff} of the KTP is equal to 3.5 pm/V. The relative spatial walk-off between the waves, involved in the three-wave mixing process, is equal to 3.48 mrad between the e-polarized FF and the o-polarized FF, and equal to 4.88 mrad between the e-polarized SH and the o-polarized FF. These walk-off values are along one transverse axis (the vertical axis), the walk-off along the other axis is negligible.

The second crystal type was a PPLN ($d_{eff} = 15 \text{ pm/V}$), manufactured by HCP Photonics Corporation. The crystal dimensions are 15 mm long, 1 mm thick, and 2 mm wide. The periodic inversion of the ferroelectric domains has a period $\Lambda_{PPLN}=6.97 \text{ }\mu\text{m}$ (at $60 \text{ }^\circ\text{C}$). The phase matching conditions are controlled by heating the crystal in an oven. The exact phase matching is obtained at 60°C , with a beam polarization orientation parallel to the extraordinary axis of the PPLN.

Because of its short length (15 mm) and thickness (1 mm), the PPLN crystal is excited with a collimated beam of $200 \text{ }\mu\text{m}$ of diameter ($1/e^2$ in intensity) and by means of a 200 mm converging lens (**E'**). In these conditions, the Fresnel length associated to the incident beam is 6.5 cm, considering the linear refractive index of the crystal. For the KTP crystal, the input beam diameter is set at $400 \text{ }\mu\text{m}$ by using a converging lens with 100 mm of focal length (**E**). The Fresnel length was in that case close to 20 cm.

For the KTP and the PPLN crystals, the diffraction length at 1064 nm was much longer than the physical length of the crystal itself. Thus, no diffraction effect was obtained for a linear propagation along the crystal. These initial conditions are far from the ones commonly used to generate solitons, where the Fresnel length of the input beam is 2 to 6 times shorter than the crystal length [3].

After propagation in the crystal, the SH beam at 532 nm can be selected by means of band-pass filters with $\pm 3 \text{ nm}$ or $\pm 10 \text{ nm}$ of bandwidth.

III.1.2. Crystal phase matching

In order to properly analyze my results, it is important to know the efficiency of SHG upon the phase mismatch Δk , i. e. as a function of the crystal orientation for type II KTP and as a function of the temperature for PPLN. I obtained two curves for the KTP crystal, one for a crystal orientation in the horizontal plan and one within the vertical one (Figure 28-(a)). In the experiments, I always tuned the phase matching conditions by modifying the fastest axis (along the angle Φ). The maximum precision achievable to control the angle orientation (to manage the phase matching conditions) is 0.05° for the KTP and 0.4°C for the PPLN (according to the oven datasheet – a CHAUVIN ARNOUX STATOP-4849).

For the KTP crystal, a phase mismatch (ΔkL) of π is obtained for a $\Delta\Phi = 0.2^\circ$ (calculated between two zeros of the sinc shaped SHG curve). For the PPLN, the number of samples of SHG versus temperature is not enough to give a precise value of ΔkL . This fact is due to the poor precision of the oven temperature controller I used to heat the PPLN.

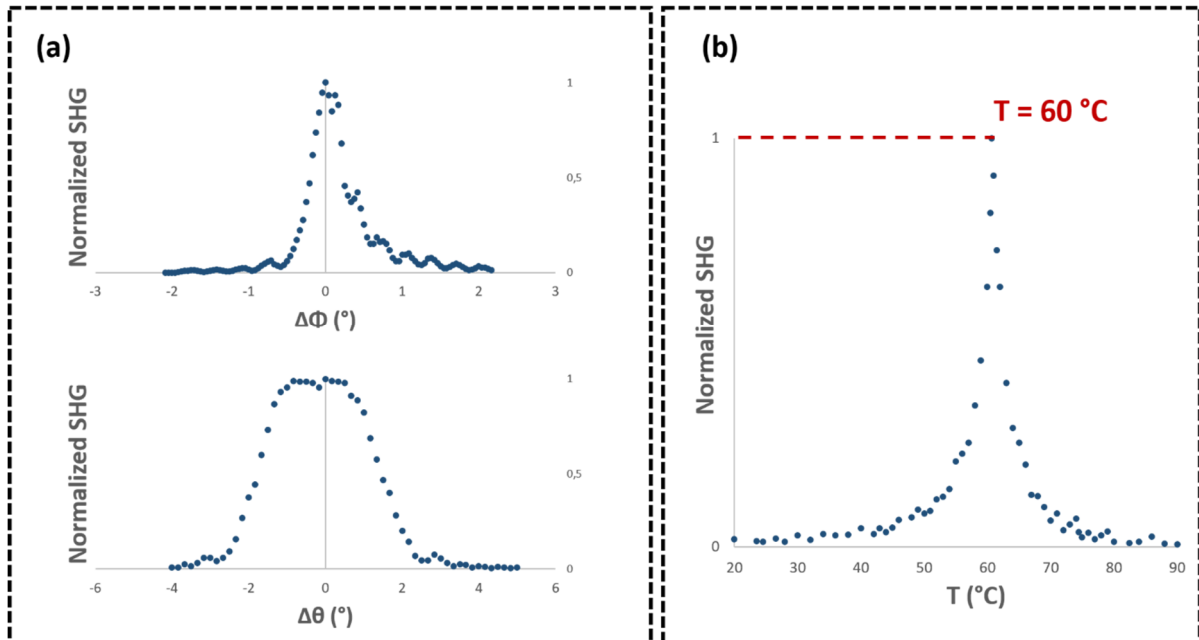


Figure 28: Phase matching curve for: **(a)**-KTP crystal within horizontal (θ) and vertical (Φ) axis orientation, **(b)**-PPLN, by modifying the crystal temperature.

III.2. 2D spatial extreme event observation in KTP crystal

In nonlinear optics, the demonstration of a particular propagation is strongly dependent of the initial excitation conditions. I remind you that the excitation of the KTP crystal is implemented with a linear polarized Gaussian beam with 400 μm of diameter (measured at $1/e^2$ in intensity). Thus, the incident beam remains collimated all along the propagation in the crystal for a linear regime of excitation i. e. with low input intensity.

For an excitation at $\sim 45^\circ$ with respect to the principal axes of the crystal, the initially FF beam is separated in two components (because of the birefringence) and one SH beam is generated because of the SHG.

Thus, spatial and temporal walk-offs occur in the crystal and each component (two FF, one SH) is progressively separated from each other in time and in space. I estimated that the

spatial separation along the y -axis is close to $100\ \mu\text{m}$ between the FF beams and $145\ \mu\text{m}$ between the SH beam and the FF ordinary component (see Figure 29). In the temporal domain, the maximum time delay is obtained for the SH with 4 ps, which is negligible in my case for an input pulse duration of 30 ps.

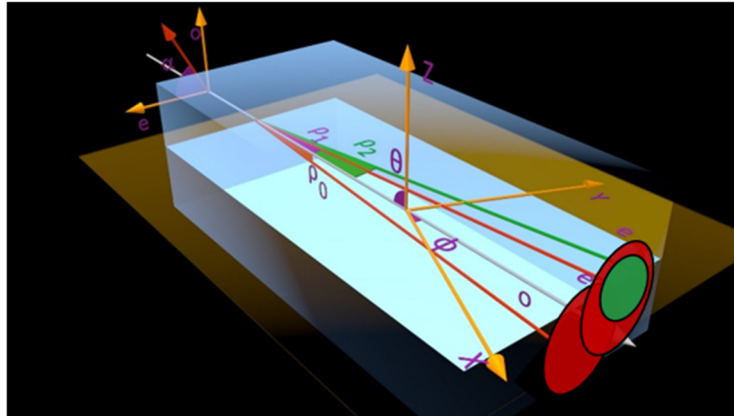


Figure 29: Beams representation at the output face of the type II KTP crystal for a nonlinear propagation regime.

In the nonlinear regime i. e. by increasing the input intensity up to $0.1\ \text{GW}/\text{cm}^2$ at exact phase matching, a first self-focusing effect is observed out of the crystal, at the FF, due to the nonlinear interactions between the three waves.

The beam diameter in intensity ($1/e^2$) of the self-trapped beam gets close to $50\ \mu\text{m}$, which is 8 times smaller than the injected FF beam. In the most favorable conditions, the energy located in this self-trapped beam is close to 3% of the total output energy. Its peak intensity is about 2.4 higher than the peak intensity of the unfocused output beam (see Figure 30-(a)).

Its output position is located on the SH beam position, off center with respect to the FF because of the spatial walk-off. It is also important to note that the trapped beam is composed by the three involved waves, i. e. of two FF beams and the SH, with walk-offs compensation because of the nonlinear trapping (see Figure 30-(b)).

Moreover, the SH beam exhibits several modulations beyond the self-trapped event (see Figure 32).

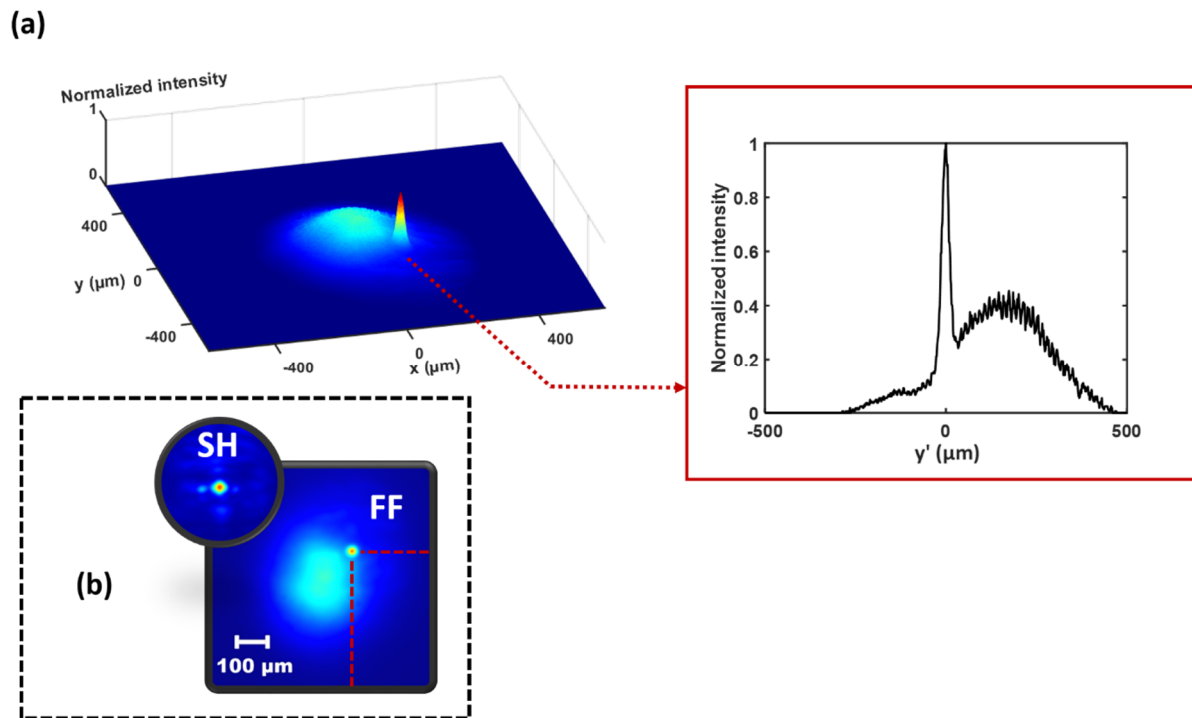


Figure 30: Output spatial beam self-trapping in KTP, for an injected pump intensity of 0.5 GW/cm^2 . **(a)**-3D view of FF beam, and transverse beam profile of the FF (red inset). **(b)**-2D representation of the FF and SH beams (SOP set close to 45° , $\Delta k = 0$). The round inset image has the same scale than the square image.

At this stage, this self-trapped beam seems to behave like a soliton even if the initial conditions were different from the ones used by Torruellas *et al.* in their experiment [3]. In my case, I first obtained a quadratic self-focusing process followed by a solitonic propagation, which maintains unchanged the shape along the nonlinear propagation (diffraction is affecting the newly focused beam due to its very small size, compared to the large unfocused pump).

We can also underline that, in 1997, R. A. Fuerst *et al.* [4] observed that spontaneous self-focusing could appear on a large beam in 1D only, giving birth to quadratic solitons. They explained this spontaneous appearance by an instability of modulation in quadratic media (see also quadratic MI observations by P. Pliszka in 1993 [5], S. Trillo in 1995 [6], J.F. Corney and O. Bang in 2001 [7] and R. Schiek in 2001 [8]). It is also important to note that in 2011 M. Delqué *et al.* [9] published the observation of spontaneous spatial 2D MI in SHG scheme, allowing the soliton excitation (for their results, see Figure 24 on paragraph II.3.3).

III.2.1. Evolution of the self-trapped beam versus the input peak power: transient rogue dynamics

In a second step, I varied the input peak power from 0.01 to 12 GW/cm² and I studied the spatial evolution of the output beam at the FF and at the SH. My results are shown on the Figure 31 for the FF beam and on Figure 32 for the SH beam.

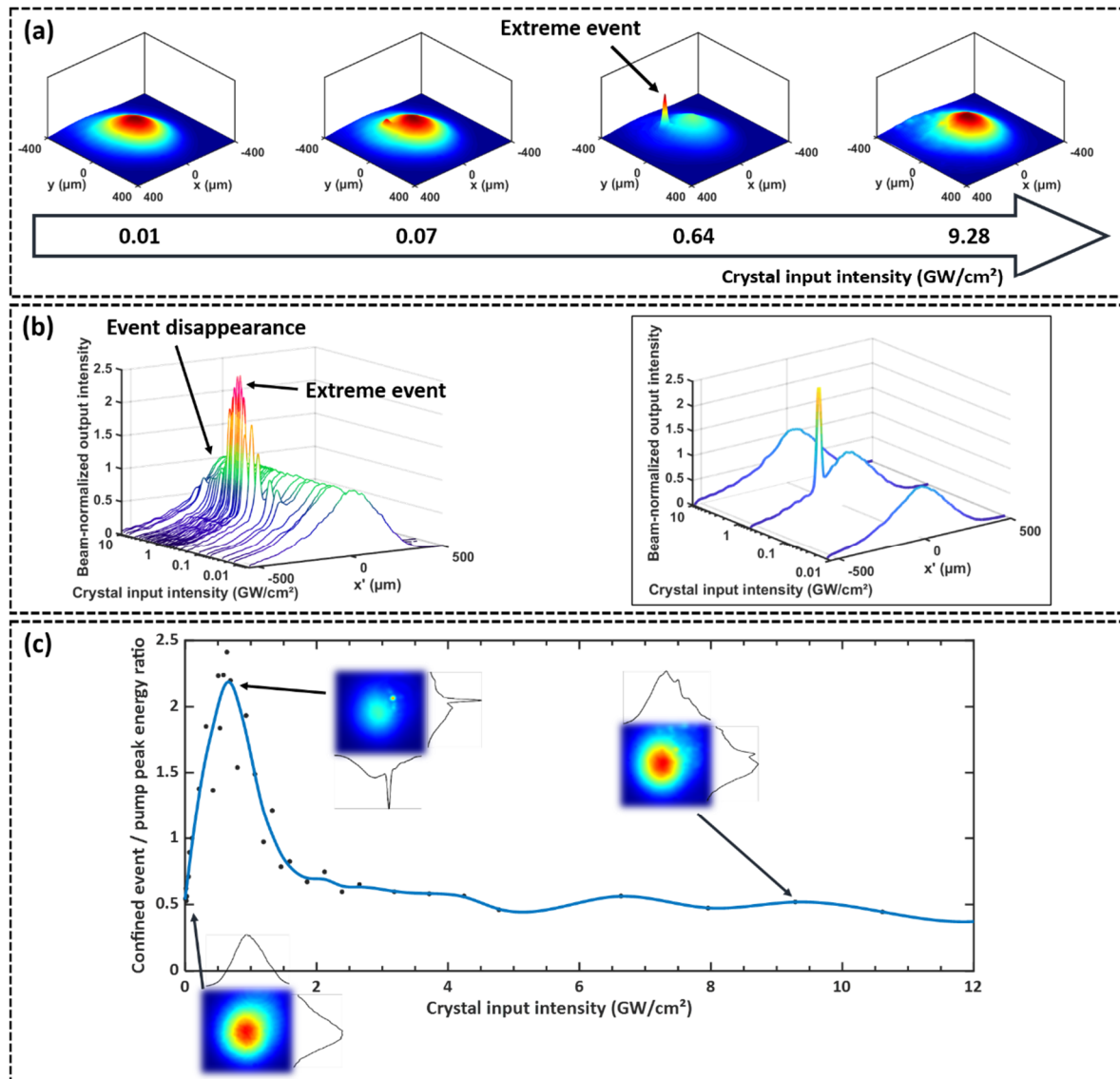


Figure 31: Appearance and disappearance of the FF self-trapped beam versus the injected pump intensity.

(a)-2D output beam evolution. **(b)**-Output profiles of the FF beam. **(c)**-Ratio of the local peak energy between the FF trapped beam and the remaining energy. Phase matching conditions, linear input SOP set close to 45°.

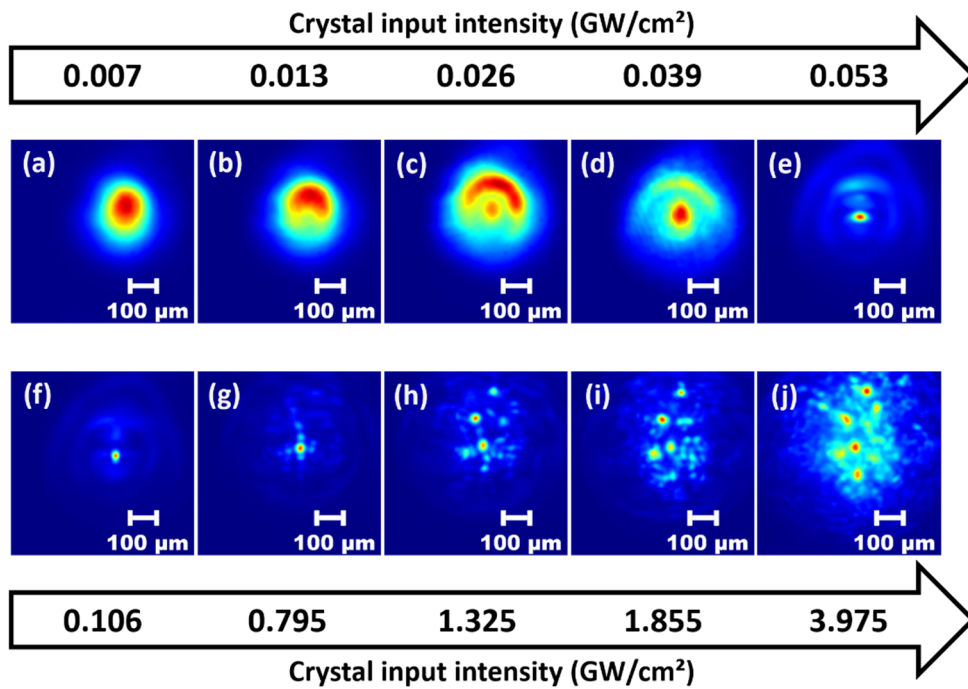


Figure 32: 2D representation of the SH beam evolution versus the input intensity. Phase matching conditions, linear input SOP set close to 45° . Images from (a) to (j) are for different input pump intensities.

The confined event I observed for an input pump intensity of 0.64 GW/cm^2 does not grow indefinitely when I increase the crystal input pump intensity. Indeed, as shown in Figure 31-(a) and (b), the event starts to disappear in KTP crystal when I increase the input pump intensity beyond 0.8 GW/cm^2 . The traces of the confined event existence are then almost invisible. Only a low residual spatial modulation remains visible on the FF beam. Thus, the output beam shape retrieves, at high intensity, its initial Gaussian profile.

The evolution of the SH beam follows the one of the FF. At 0.007 GW/cm^2 (see Figure 32-(a)), the SH beam has a Gaussian shape and is depleted at its center when the intensity increases to 0.013 GW/cm^2 (Figure 32-(b)). The spatial focusing starts then in the depleted part at 0.02 GW/cm^2 (Figure 32-(c)) and the Gaussian background disappears between 0.05 GW/cm^2 and 0.1 GW/cm^2 (Figure 32-(e-f)). Only a highly confined beam is visible for a pump intensity of 0.1 GW/cm^2 (Figure 32-(f)). By driving the intensity beyond 0.8 GW/cm^2 (Figure 32-(g-j)), the beam starts to split irregularly in the transverse plane, and the intensity distribution becomes chaotic after 1.3 GW/cm^2 (Figure 32-(h)), leading to a speckled pattern of highly focused beams at 1.8 GW/cm^2 (Figure 32-(i)). At 4 GW/cm^2 (Figure 32-(j)), the SH intensity is very high and the background energy increases, decreasing the contrast between the focused spots and their background.

Numerical Simulations:

Along my thesis, I have not developed a code to simulate the 2D transverse evolution of a trapped beam with quadratic nonlinearity. That work has been realized by Prof. Fabio Baronio from Brescia University. I report in this manuscript only one example of his simulations, using three-wave equations, with the purpose of demonstrating the potentiality to numerically retrieve the transient evolution of the self-trapped beam seen in my experiments.

The simulation included the two equations for the two polarization components of the FF beam and a third equation for the SH. The walk-off was included as well as the diffraction, the quadratic susceptibility and the phase mismatch. The time domain was ignored. Like in the experimental approach, the walk-off was set relative to the ordinary component, i.e. the reference wave. The numerical input condition was a Gaussian shaped beam with a diameter of $400\ \mu\text{m}$ (at $1/e^2$ of intensity), seeded by a small bump which as a spatial offset from the beam center.

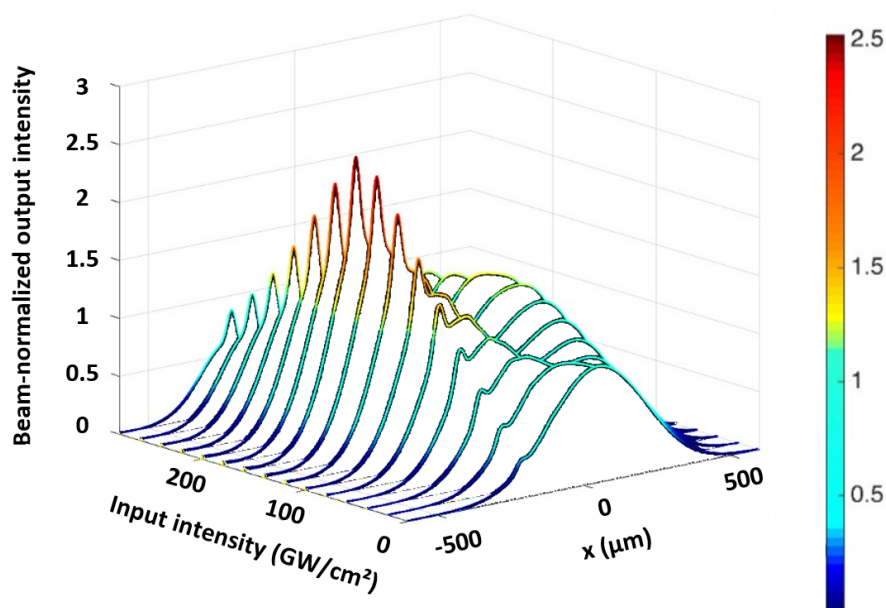


Figure 33: FF wave section evolution in function of the input intensity I_0 . Simulation along a nonlinear material propagation of 30 mm. Works realized by Fabio Baronio from the University of Brescia (phase matching conditions).

Figure 33 shows a collection of output beam shapes at the FF upon different input energies. We observe strong similarities between the present figure and the experimental results described in paragraph III.2.1 (Figure 31-(b)); in particular, the weak bump gives rise to a

trapped beam, clearly visible in the simulation for pump intensity of 0.1 GW/cm^2 and whose peak is around 2.5 times the maximum level of the residual pump.

Although there is a qualitative agreement between numerical and experimental results, we can notice some discrepancies: the self-trapped beam tends to vanish for a pump intensity of 0.2 GW/cm^2 in the simulation, while 0.8 GW/cm^2 are required in my experiments. In addition, in the simulation, the self-trapped beam does not disappear completely, whereas, in the experiments, it completely vanishes.

It is important to underline here that the temporal domain is not taken into account in the simulation, and this fact seems to play a strong role in the nonlinear dynamic. This part will be discussed in paragraph III.2.4 with a series of experimental results in time domain.

III.2.2. Evolution of the self-trapped beam versus the input polarization orientation

It is well known that spatial solitons obtained in type II KTP crystal are strongly dependent of the input polarization state (see Torner *et al.* in 1995 [10], Torruellas *et al.* in 1996 [11], Clausen and Torner in 1999 [12] and Carrasco *et al.* in 2003 [13]). Additionally, the spatial walk-off between waves plays a critical role, allowing the spatial soliton displacement with respect to the initial polarization orientation of the FF beam.

I then investigated the impact of the input linear SOP on the self-trapped beam. I first studied the polarization orientation in vicinity of the optimal angle to generate SH wave i. e. at 45° with respect to the principal axes (see Figure 34-(a)). In the Figure 30, I showed the self-trapped beam, but the SOP was not exactly at 45° .

When the angle is exactly set at 45° , two spatial self-trapped beams are observed, which correspond to a particular solution of the propagation [11]. Both self-trapped beams have the same diameter as the one obtained with another polarization orientation, on Figure 30 ($\sim 50 \mu\text{m}$ at $1/e^2$ in intensity), and they are separated of nearly $40 \mu\text{m}$ (see Figure 34-(b)). This position is very critical and unstable so that, for a weak energy unbalance between the two polarization components, only one self-trapped beam is obtained. The minimum unbalance leading to the extinction of the second self-trapped beam is estimated to 0.5° from the central position (45°). It is also interesting to note that, after the spatial switching, the self-trapped

beam slightly oscillates before reaching a stable position when moving the angle further than the central position at 45° .

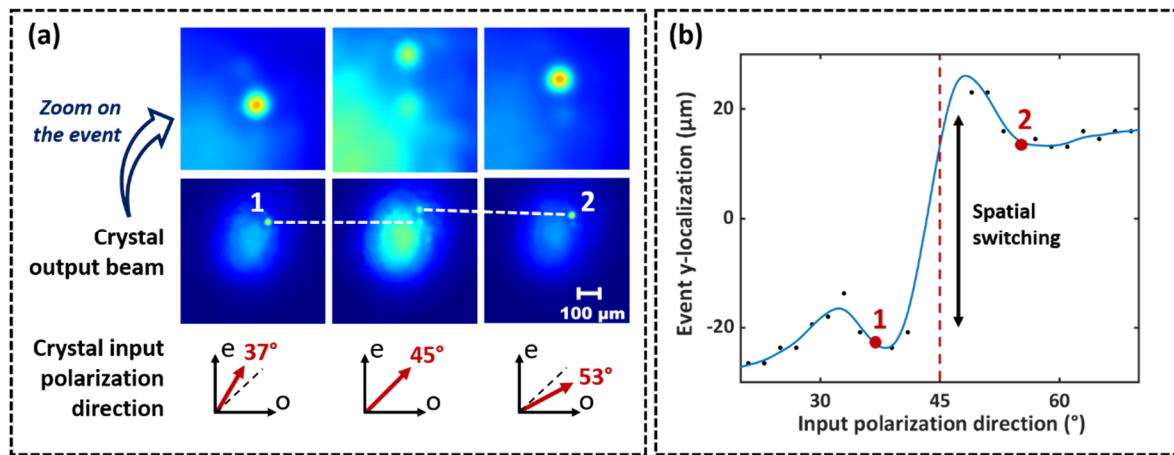


Figure 34: Position of the self-trapped beam versus the linear input SOP (input pump intensity: 0.66 GW/cm^2 and phase matching conditions). **(a)**-2D images of the output beam, for three different values of SOP. **(b)**-Evolution of the FF self-trapped beam position versus the linear input SOP; the blue curve is a guide for the eyes.

Beyond the position of the self-trapped beam, I also investigated its energy fraction. I plotted on Figure 35 the amount of trapped FF energy, after propagation in the crystal, in function of the linear input SOP and for a constant input energy.

To do that, I simulated a spatial filter of $50 \mu\text{m}$ of diameter, located around the trapped beam, and analyzed the ratio of power transmitted through this filter, compared to the total power (remaining pump + self-trapped beam).

For a polarization angle close to 45° , the FF energy has an equal repartition on each principal axis. In this case, the FF energy trapped in the confined beam seems to reach its minimum.

For other angles values, with respect to the middle position (45°), the energy contained in the trapped beam increases symmetrically for high and low angles. It reaches two maxima, close to 30° and 60° , before decreasing again.

At the angles required for a maximum trapped energy, the self-trapping is particularly stable and robust with respect to extern perturbations; in those cases the energy content is close to twice the one obtained when the polarization angle is at 45° (see Figure 35).

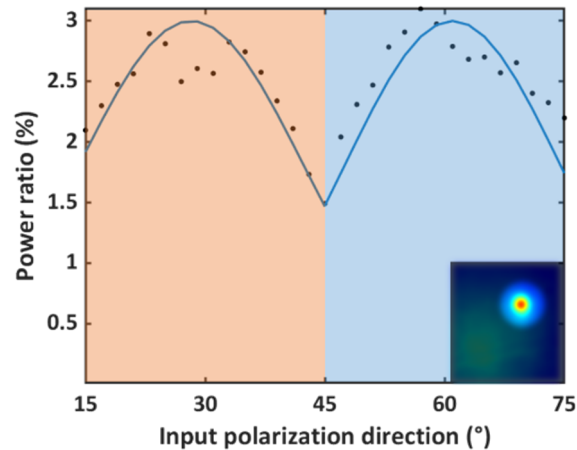


Figure 35: Power ratio between the energy in the confined beam area and the total beam energy, versus the linear input SOP. The input pump intensity is 0.66 GW/cm^2 . All these results have been obtained at phase matching conditions.

In addition to the energy fraction of the FF trapped beam, I also measured the energy on each polarization component by placing a Wollaston prism between the crystal and the camera. In this way, the Wollaston prism separates the two polarization components of the output beam due to an anisotropic refraction along the prism principal axes e or o. A summary of that study is schematically given on the Figure 36.

Each beam component is refracted by a specific angle and collected by the camera. Thus, at the FF (Figure 36, top insets), the image of the self-trapped beam is replicated twice along the horizontal axis. These images represent the e-polarization and the o-polarization respectively. A similar decomposition is obtained for the SH (Figure 36, bottom insets).

When the input polarization is unbalanced in favor of e or o axis (respectively linear input SOP = 37° or 53°), the polarization state of the self-trapped beam at the FF will follow the polarization state of the dominant input component. At the output of the Wollaston prism, I can visualize two horizontal FF spots with an unbalanced energetic content, which also confirms the nonlinear nature of the process. In the case of the SH beam, I always observed a single horizontal spot: this fact confirms that the SHG is of type II, with the SH polarized along the extraordinary crystal axis only.

In the particular case of a linear input SOP of 45° (Figure 36-(c)), the FF energy is equally divided along the e and o axis (same amount of energy along both e and o polarization states). Thus, for the same SOP, the SH is constituted of two vertical spots with e-polarization.

The spatial walk-off is driving the output location of the self-trapped beam at the FF and at the SH; the horizontal spatial walk-off is negligible, and only the vertical spatial walk-off is to be considered. The input beam intensity is 0.66 GW/cm^2 and the crystal is oriented to reach the exact phase matching.

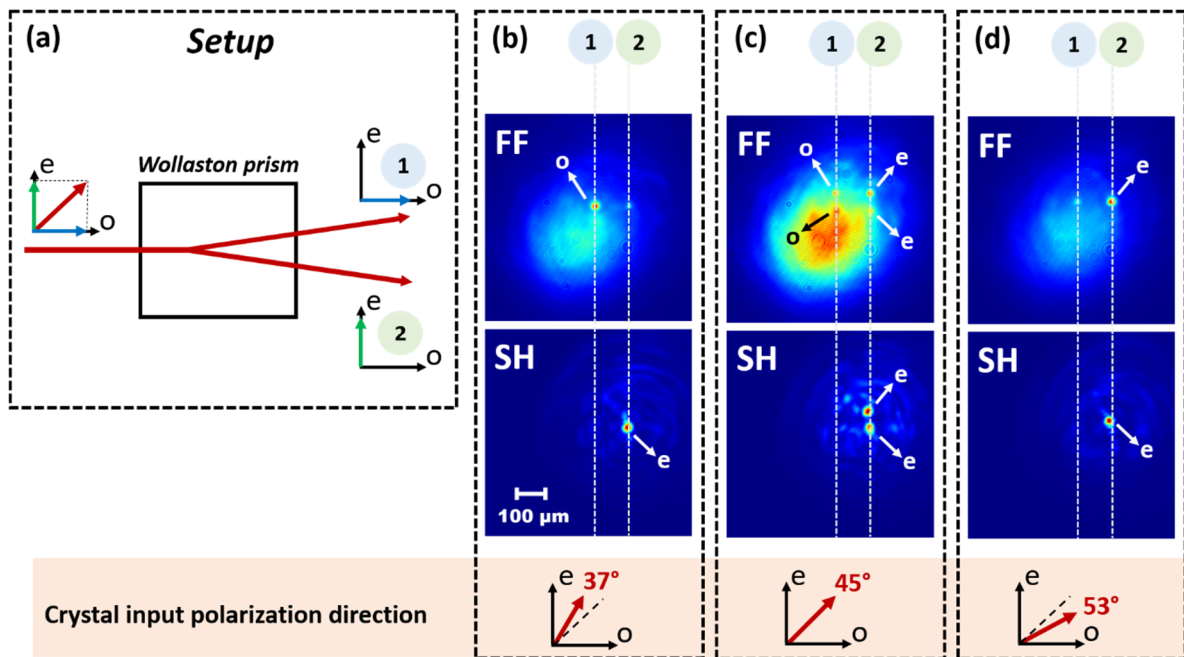


Figure 36: Polarization content of the self-trapped beam versus the linear input SOP. **(a)**-Schematic representation of the system used to realize the experiment; **(b-d)**-2-D spatial output images for three different polarization states and for both FF **(top)** and SH **(bottom)** beams (Intensity: 0.66 GW/cm^2 , phase matching conditions).

III.2.3. Evolution of the self-trapped beam versus the phase mismatch

The phase matching parameter, driving the SHG efficiency, necessarily has an impact on the nonlinear dynamics. To investigate the influence of that parameter, I varied the vertical crystal angle $\Delta\Phi$ (relative to the fastest axis) of the nonlinear crystal and recorded at each step the output images. Then, by overlapping all these images, I obtained a continuous evolution of the self-trapping effect as a function of the crystal angle (see Figure 37).

The main interest of this observation is that the self-trapping process, at 0.3 GW/cm^2 , is mainly obtained from a vertical crystal angle $\Delta\Phi$ of -1° to a vertical angle of 2° (max SHG is at $\Delta\Phi = 0$), i. e for a $-5\pi < \Delta kL < 10\pi$.

The range on which I obtained the spatial self-trapping is also directly dependent of the input intensity and can be reduced to the exact phase mismatch point when reaching the threshold process.

However, by changing both the input intensity and the crystal phase mismatch, I can obtain a more complex behavior, which favors the appearance of multiple spots, not randomly distributed in the output beam pattern. These results are presented in chapter V.

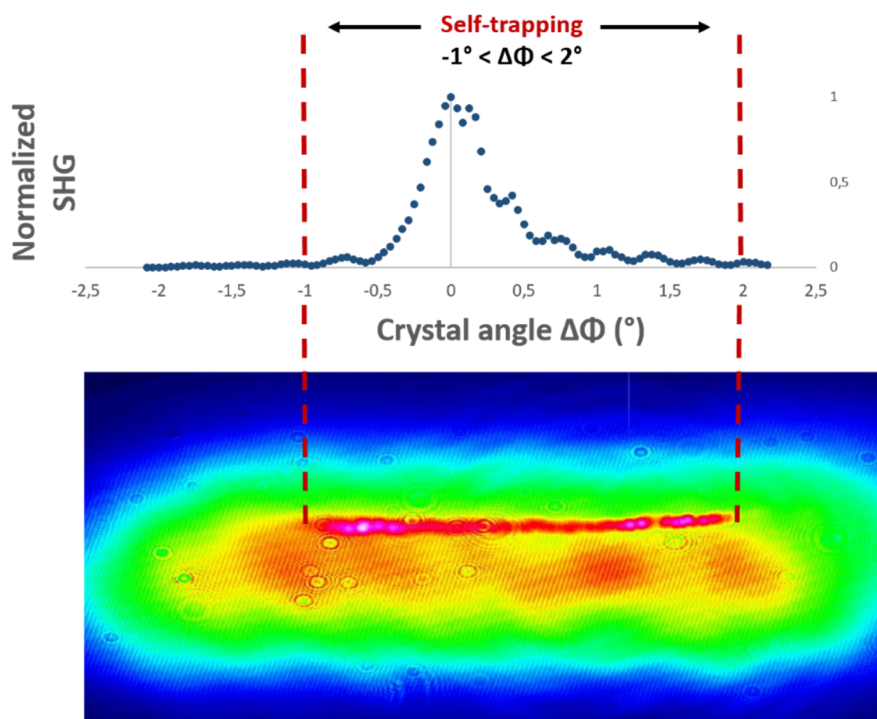


Figure 37: Output images of the FF beam versus the vertical angle $\Delta\Phi$ of the KTP crystal. **(top)**-SHG curve versus vertical crystal angle of the KTP, **(bottom)**-2D output spatial image of the beam at the end face of the crystal (input pump intensity = 0.3 GW/cm^2 , linear input SOP set close to 45°).

III.2.4. Evolution of the output temporal profile of the self-trapped beam

Because of the nonlinear nature of the process and the initial Gaussian pulse used for excitation, one can expect that the temporal domain should also be subject to distortions.

By using an intensity autocorrelator (EKSPILA AC1064) based on SHG, I investigated the temporal profile evolution of the trapped beam.

In order to select the energy confined in the self-trapped beam, I introduced a spatial filter between the crystal and the autocorrelator. So that, I only recorded the part of the beam modified by nonlinearity, independently to the remaining pump.

A half-wave plate and a band-pass filter (1064 nm +/- 10 nm) allowed to modify the input polarization introduced in the autocorrelator and to select the FF beam only.

The beam at the output of the crystal was collimated by a convergent lens for minimizing the spatial divergence and improving the signal to noise ratio when collecting the autocorrelation signal.

In the linear regime, and assuming a Gaussian profile of the autocorrelation, I deduced that the input pulse had a duration of 29 ps, equal to an autocorrelation trace of 41 ps, measured at Full Width Half Maximum in Intensity (FWHMI), as we can see on Figure 38 – input pulse profile.

A temporal compression is measured when the spatial self-trapped beam is present. The autocorrelation trace is then reduced from 41 ps to 24 ps (see Figure 38). This temporal compression is also observed for $\Delta kL = 5\pi$ and $\Delta kL = -9\pi$. (Figure 39 and Figure 40 respectively). We can also observe that the output profile of the trapped beam tends to suffer from temporal distortions, transforming the initial Gaussian autocorrelation profile into a quasi-triangular one.

At each phase mismatch value, the increase of the input intensity leads to a major pulse duration increase or a pulse breaking process. That temporal structuration appears when the intensity is sufficiently high to make the self-trapped beam vanish in the spatial domain. In that situation the temporal walk-off between the FF and the SH is no longer compensated, and this in turn may give birth to a temporal pulse broadening. The autocorrelation trace indicates the presence of at least two pulses separated by several tens of picoseconds (see Figure 38 - $\Delta kL = 0$ and Figure 39 - $\Delta kL = 5\pi$). The temporal pulse for $\Delta kL = -9\pi$ (Figure 40) broadens without clear pulse breaking effect, even if the autocorrelation trace exhibits large pedestals.

These observations tend to prove that, in spite of the retrieval of the output Gaussian profile in the spatial domain, the output beam remains significantly degraded in the temporal domain, after the nonlinear propagation; at least in the area where the trapping occurred.

It is also important to note that the pulse breaking process seems more pronounced for a positive phase mismatch ($\Delta kL = 5\pi$) assuming the same initial intensity. We can for example see a more modulated autocorrelation trace at 8 GW/cm² for $\Delta kL = 5\pi$, than the one at the same intensity and for $\Delta kL = -9\pi$.

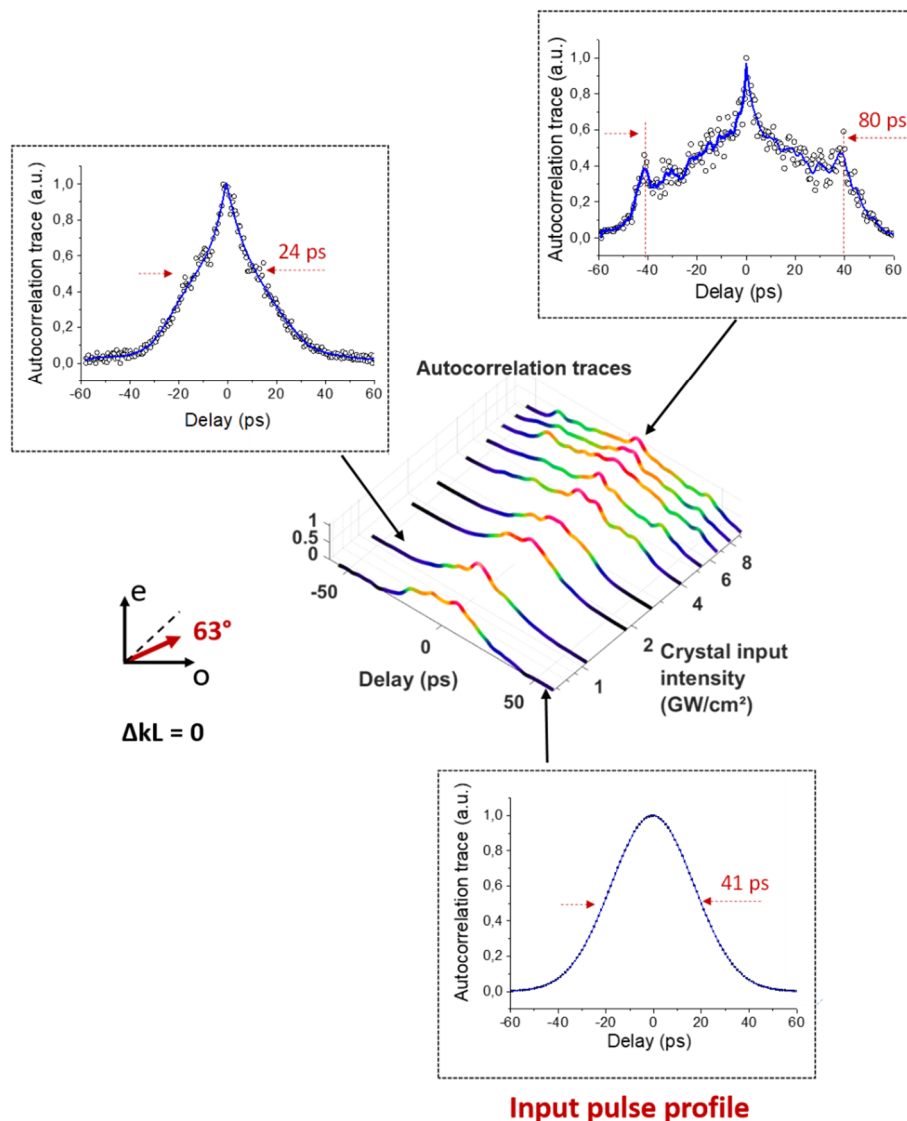


Figure 38: Experimental results of the spatial trapping influence on the temporal domain. Autocorrelation traces of the trapped beam versus the input intensity for $\Delta kL = 0$ (phase matching) and a linear input SOP = 63°.

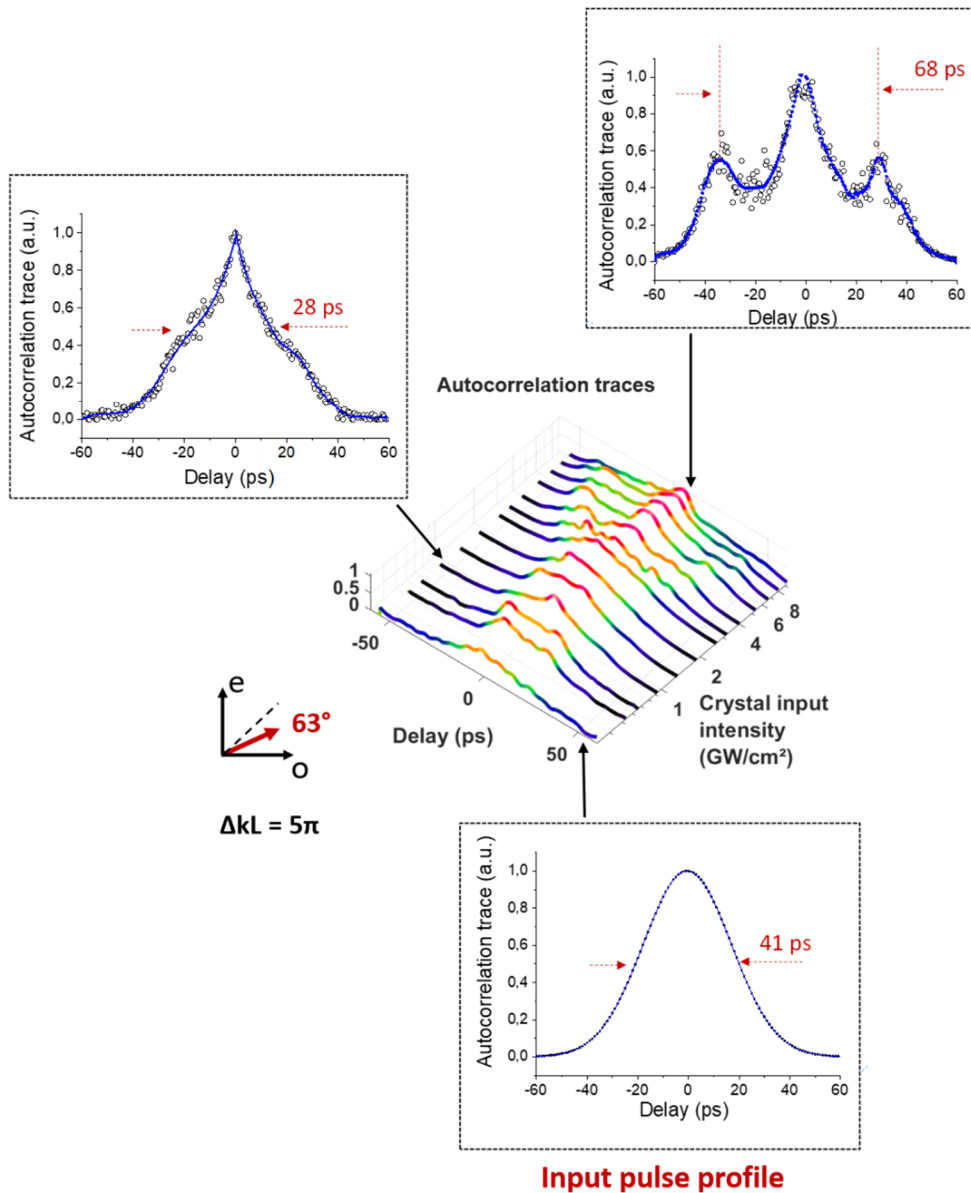


Figure 39: Experimental results of the spatial trapping impact on the temporal domain. Autocorrelation traces of the trapped beam versus the input intensity for $\Delta kL = 5\pi$ and a linear input SOP = 63°.

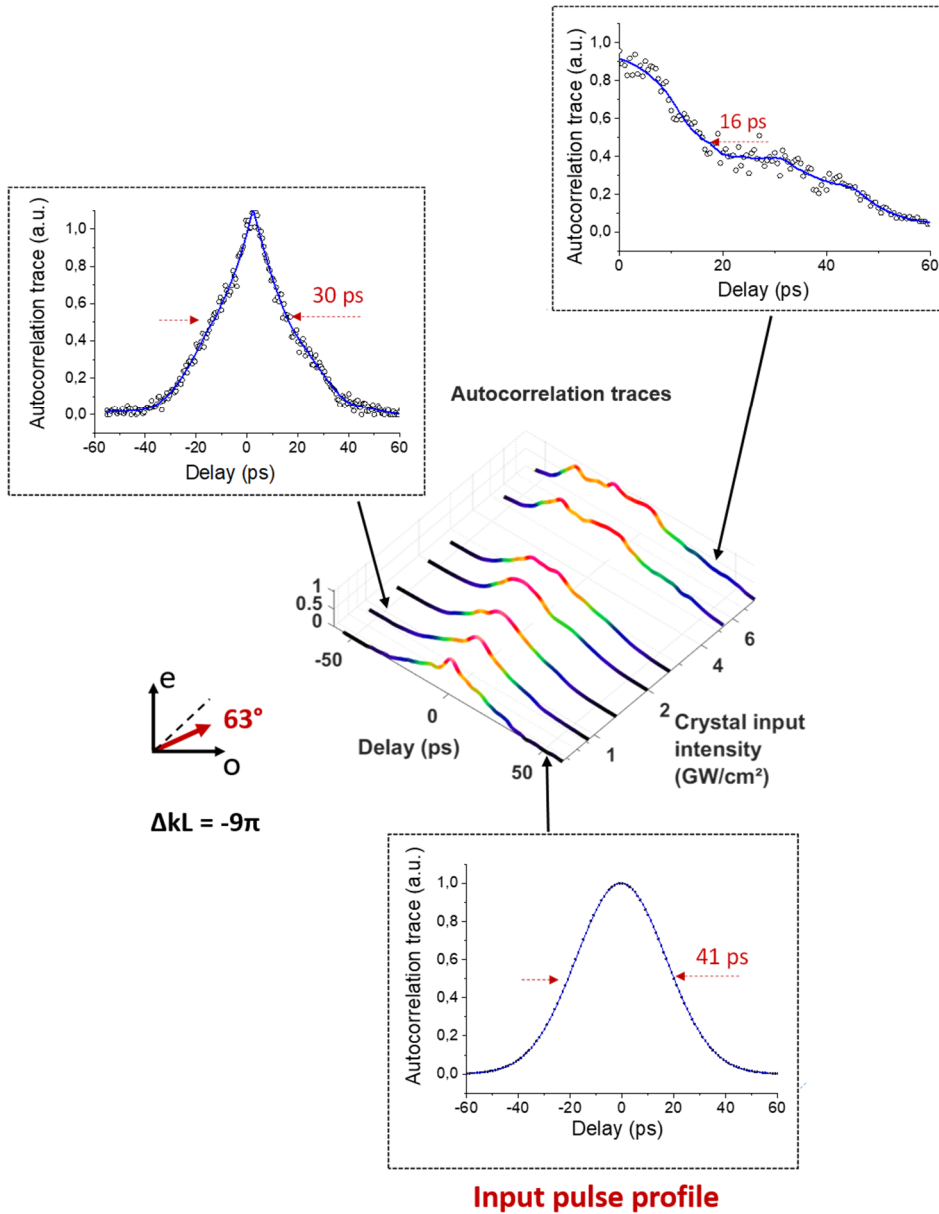


Figure 40: Experimental results of the spatial trapping impact on the temporal domain. Autocorrelation traces of the trapped beam versus the input intensity for $\Delta kL = -9\pi$ and a linear input SOP = 63° .

III.2.5. Spectral broadening and distortion of the self-trapped beam spectrum

The spectral shape of the trapped beam reflects the dynamics of the nonlinear process (see Figure 41).

At exact phase matching, the FF spectrum progressively broadens when the input intensity grows larger. Such tendency is asymmetric with respect to the central wavelength and it favors the longer (infrared) wavelengths. For very high pump intensity, when the spatial trapping

decay is observed, the FF broadening stops and eventually goes backward. Such reversed tendency in the spectral broadening, upon intensity, is mainly observed for $\Delta kL = 0$ or $\Delta kL = 9\pi$.

The SH spectrum exhibits the same asymmetric evolution, with lower broadening amplitude and toward the bluest wavelengths.

Therefore, the spectral reshaping amplitude remains higher for $\Delta kL = 9\pi$ where the spatial trapping efficiency is stronger. That spectral evolution is driven both by the nonlinear conversion and the temporal / spatial walk-offs between the FF and the SH beams.

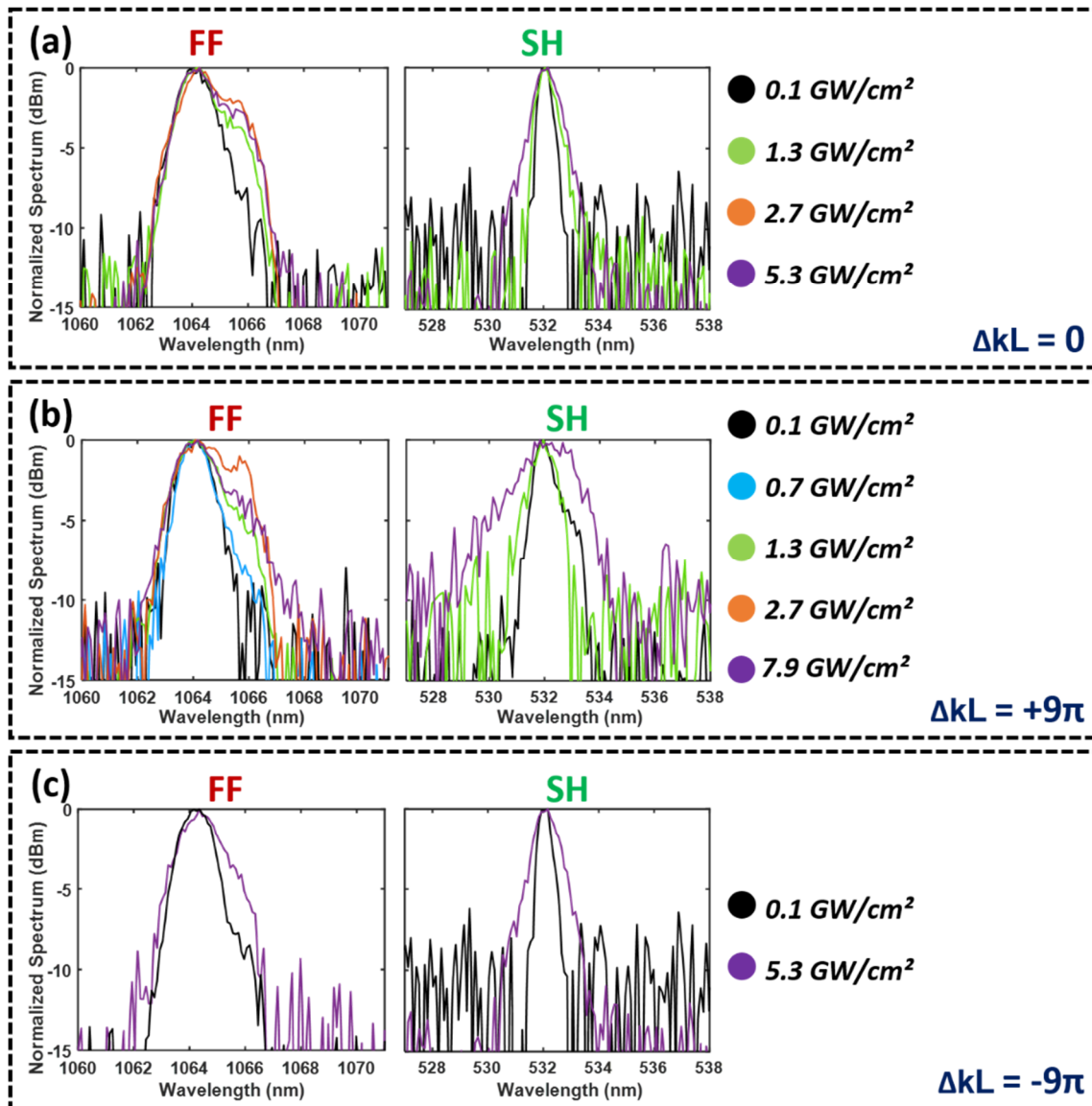


Figure 41: Output spectrum of the trapped beam versus the pump intensity, for a linear input SOP of 69° .

(a)- $\Delta kL = 0$. (b)- $\Delta kL = 9\pi$. (c)- $\Delta kL = -9\pi$.

III.3. Discussion and analysis about the nonlinear dynamics

After the theoretical prediction of quadratic soliton by Karamzin and Sokurokov in 1974 [14], Torruellas and coworkers (see ref [3]) realized the experimental demonstration in type II KTP crystal (as told in paragraph II.3.1). They used an infrared radiation at 1064 nm, which was focused on the input face of the nonlinear crystal with a diameter sufficiently small in order to obtain a progressive spatial broadening under the effect of the diffraction by propagation in the crystal. The initial beam used in their experiments had a Fresnel length five times smaller than the crystal length. By increasing the pump intensity, the diffraction was progressively compensated by the quadratic nonlinear process. In other words, the linear spatial phase evolution leading to spatial broadening was compensated by the nonlinear phase introduced by the cascading effect.

In my case, the input conditions are significantly different from the ones used in the Torruellas experiment [3]. I use a large collimated FF beam without any diffraction effect in nonlinear regime. By increasing the input intensity, a first self-focusing is obtained in the area where the three waves, i. e. two at the FF and one at the SH, are superimposed. The FF and the SH beams are then concentrated on a small spot, whose diameter is determined by the balance between the linear and nonlinear effects. It is difficult to establish a direct comparison with the case of a spatial soliton solution. The equilibrium between the diffraction and the nonlinearity is only observed at the end of the crystal whereas the first stage acts as a spatial focusing effect. We can also underline that this spatial stabilization is obtained for a large range of input intensity (from 0.1 GW/cm² to 0.8 GW/cm²) because of the saturation of the quadratic nonlinearity.

In 2011, Michaël Delqué and coworkers published results on quadratic spatial MI in type II KTP [9], as said on paragraph II.3.3. Their experiment was realized at the same wavelength than in my setup and by using similar crystal and input conditions i. e. with large collimated beam. They obtained several self-focused beams, randomly distributed on the total output beam surface. Each focused beam had a particular shape, showing concentric oscillations in its spatial spectrum. This fact was interpreted as the signature of a 2D MI (already studied by P. Pliszka in 1993 [5], S. Trillo in 1995 [6], J.F. Corney and O. Bang in 2001 [7] and R. Schiek in 2001 [8]). For higher input intensities, M. Delqué *et al.* [9] concluded that the nonlinear propagation process gave birth to multiple so-called quadratic solitons.

In my case, and in spite of different initial conditions, we do not observe a simple effect but a cascade of effects showing, in a first step, a 2D self-focusing process. It leads, in a second step, to one or more spatial self-trapped beams (two generated for a SOP = 45° and we will see later, on chapter V, the generation of more than three self-trapped beams). Moreover, no clear signature of MI has been observed in my experiments, similar to the one observed by M. Delqué *et al.* [9] (see Figure 24 on paragraph II.3.3). Nevertheless, we cannot exclude the effect of the spatial 2D MI in the first stage of our nonlinear dynamics. However, the area where the trapped beam appears is mainly determined by the spatial walk-off, which restricts the overlap between all the waves involved in the nonlinear process. In these conditions, the localization of the self-trapped beam seems to be mainly determined by the walk-off under the influence of the spatial MI.

For an input intensity higher than 0.8 GW/cm², the trapped beam I observed, that we can qualify of 2D soliton, starts progressively to decay while I increase the input intensity. Thus, for an intensity higher than 3 GW/cm², the initial FF Gaussian beam retrieves its initial shape without any evident traces left by the spatial self-focusing and the solitonic propagation. We can also observe in the self-trapped zone (FF beam) some slight modulations localized in vicinity of the focusing point (Figure 31 on paragraph III.2.1). It will be very difficult to characterize these remaining oscillations on the initial pump beam. This way, the analysis will be realized on the SH beam, which is much more affected by the nonlinear dynamics.

In this sense, it is also important to note that, after the appearance and disappearance in power of the soliton, the SH spatial shape shows large modulations that turn into spatial speckles, which will be more characterized in chapter IV. I will also demonstrate that this modulated SH beam could be spatially self-cleaned, changing a speckled beam into a uniform large beam.

In order to find the reason of the soliton disappearance, I plotted on Figure 42 the diameter of the elementary spot constituting the SH beam, upon the pump intensity. For the low conversion regime, the SH beam remains homogeneous and large. For pump intensity below 0.8 GW/cm², a soliton is observed. The diameter of the smallest spot constituting the SH is equal to the FF soliton diameter (30 μm-FWHM). For higher intensities, we can observe the SH speckle because of the nonlinear self-trapping jointed effect in presence of walk-off and MI. This spatial structuration, weakly encrusted on the FF and more deeply on the SH beam,

seems to change its size while introducing a modulation on the spatial soliton beam, which could cause its disappearance.

In other words, the spatial modulation obtained at very high intensity could compromise the mechanism of cascading and in turn the fate of the spatial soliton itself, dictating its disappearance.

The average size of the beams composing the SH speckle will be subject of investigations on the chapter IV, where I will study the speckled aspect of the SH beam.

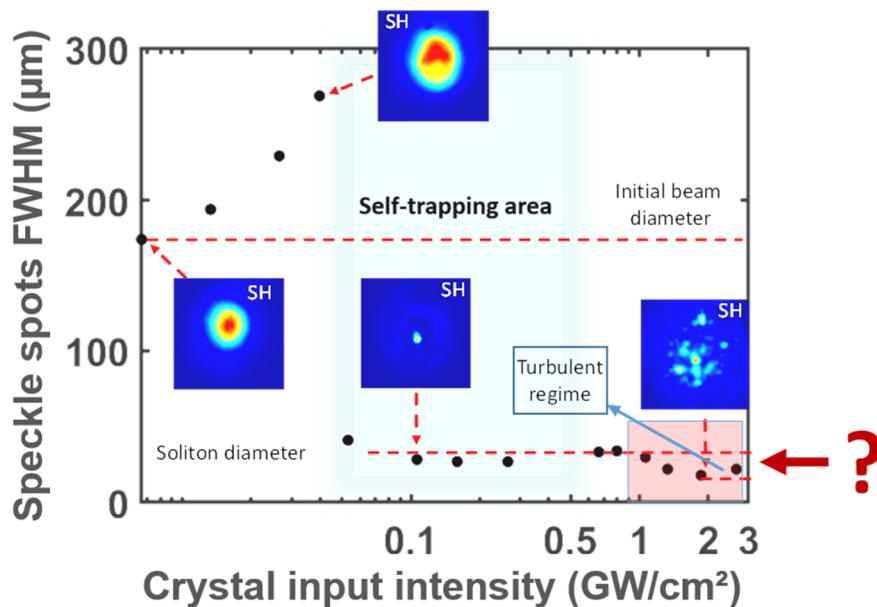


Figure 42: Spatial evolution of the SH beam versus the input intensity. The vertical axis reports the elementary spot diameter constituting it ($\Delta kL = 2\pi$ and linear input SOP $\sim 45^\circ$).

III.4. Similarity and differences with respect of the Peregrine soliton

The Peregrine soliton is a self-trapped beam, obtained on a non-zero background and which have been observed both in Kerr media (Kibler *et al.* in 2010 [15]) and quadratic crystal (Baronio in 2017 [16]). It possesses a mathematical solution in 1D only (see I.2.3 and II.3.3 for a more complete review on this soliton).

In my experiment, the process is in 2D, and I have no analytic solution as a reference. Additionally I never coupled a second beam to force the presence of a background, which would drastically change the initial conditions. However, in our quadratic process, the conversion toward the SH and the inverse process toward the FF has no full efficiency and this may in turn create a non-zero background composed of the untrapped FF energy. The 2D rogue event observed here (soliton appearance then disappearance) could be associated to this non-zero background presence. The present hypothesis needs further investigations and anyway does not simplify the problem of lack of a mathematical model for extreme waves in 2D.

I compared on the Figure 43 the shape of the Peregrine soliton, observed in an optical fiber by Kibler *et al.* in 2010 [15], with the shape of my self-trapped beam. The local minima clearly visible in Kibler's experiments (Figure 43-(a)) were equal to zero. In my case instead, the minimum values around my self-trapped beam (Figure 43-(b)) were equal to the background intensity (composed of the remaining pump). The eventual small intensity modulations, which could appear around my self-trapped beam, are hidden by the remaining pump. In order to remove this uncertainty, I also plotted the profile of the SH beam (Figure 43-(c)). Oscillations in vicinity of the trapped event are then clearly visible. From this simple observation we could also argue that, because of the intrinsic coupling between the SH and the FF beams, this modulation could exist on the FF beam but be shadowed by the non-zero background. In comparison, the profile of the Peregrine soliton in fiber (Figure 43-(a)) exhibits a clear modulation for absolute time values up to 0.5 ps.

B. Kibler *et al.* [15] observed a phase inversion at 0.5 ps, close to the soliton center. It breaks the intensity shape and leads to the soliton disappearance (Figure 43-(a)). In my experiments, the disappearance of the soliton could be explained by analyzing the SH beam, which decays in a speckle under the complex nonlinear conversion effect. The speckled shape of the SH is progressively transferred toward the FF wave. This induces strong variations in intensity and

changes the propagation conditions. Those conditions are then no more favorable to the soliton existence. The spatial transformation of the SH beam shape is also to consider in relation with the pulse breaking observed in time domain.

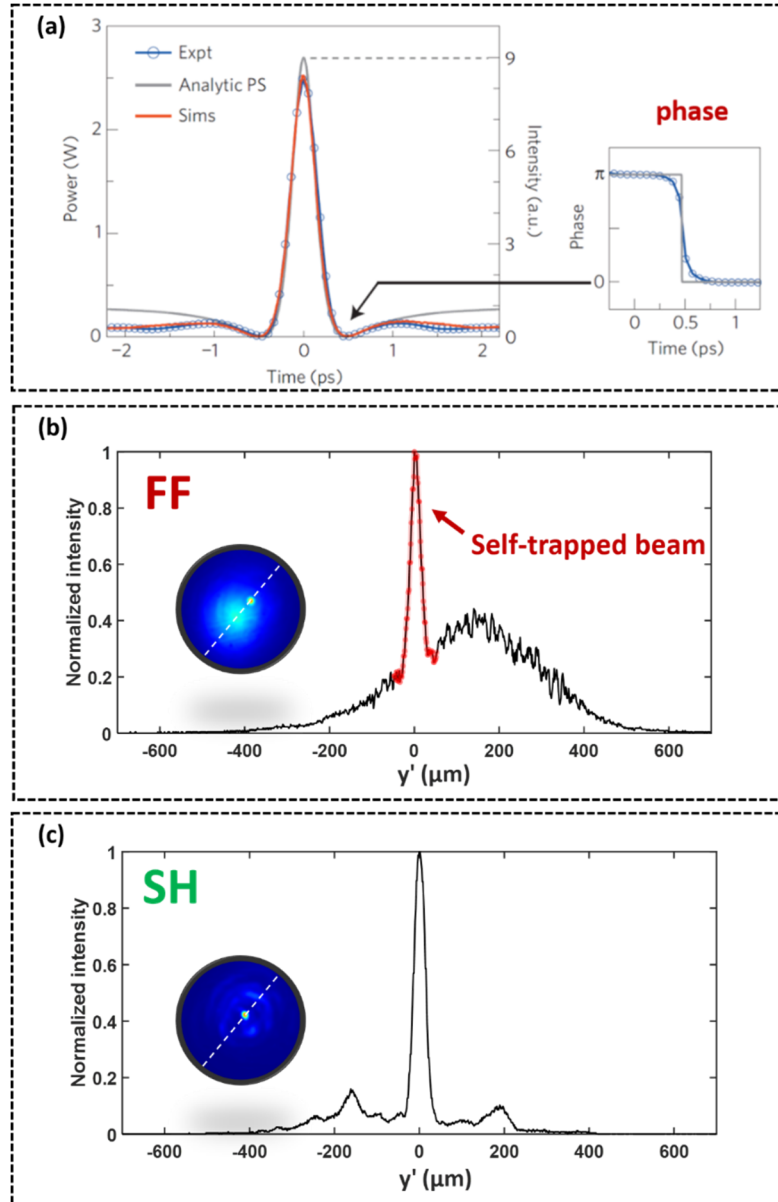


Figure 43: **(a)**-Temporal Peregrine soliton observation by Kibler *et al.* [15] in optical fibers. **(b)**-My observation of the spatial FF soliton. **(c)**-My observation of the SH trapped beam. In both **(b)** and **(c)**, the round insets are the images of the corresponding beams, out of the KTP, and the dashed line in those insets shows the sense of cut for the profile plotting. Phase matching conditions, linear input SOP = 53° and input pump intensity = 0.3 GW/cm^2 .

III.5. 2D extreme event in PPLN crystal

In order to know the exact impact of the spatial walk-off and the role of the nonlinear coefficient of the crystal, I repeated the same experiment in a PPLN crystal, whose spatial walk-off effect is negligible.

The experimental setup is similar to the one used previously. However, in order to fit with the size of the crystal, the input beam was reduced to 200 μm in diameter at $1/e^2$ in intensity.

The 15 mm long PPLN crystal is 4.5 times shorter than the corresponding Fresnel length of the incident beam. It guarantees a linear propagation without divergence along the crystal.

The nonlinear coefficient is four or five times higher than that of KTP crystal ($d_{\text{eff}} = 15 \text{ pm/V}$ for PPLN typically). Because of the quasi-phase-matching conditions, the SHG can be of type 0, with all the waves polarized along the extraordinary axis. Thus, no spatial walk-off is observed between the interacting waves.

Similarly to the experiments in KTP crystal, I progressively increased the incident pump intensity and I observed the same dynamics: a first self-focusing followed by a soliton propagation. The main difference with respect to the KTP is the position of the soliton, which appears, in the PPLN, at the exact center of the incident Gaussian beam, owing to the lack of spatial walk-off (see Figure 44).

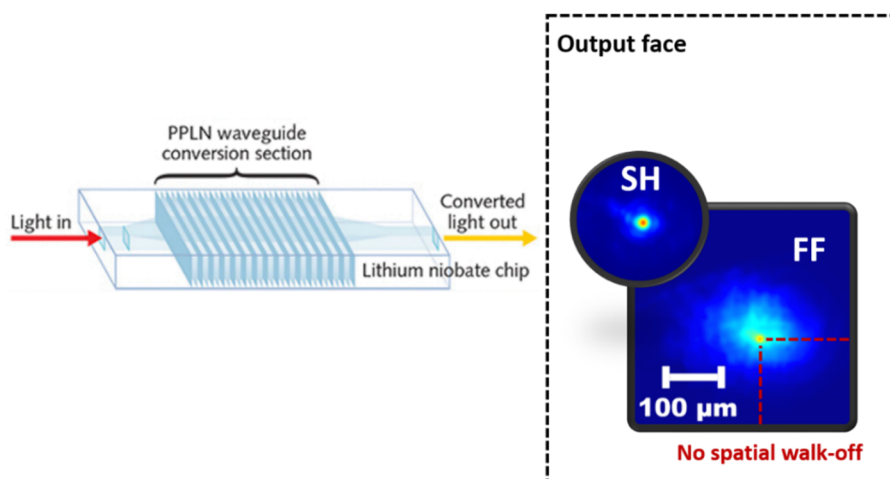


Figure 44: **Left**-Schematic of a PPLN crystal. **Right**-Spatial output soliton after propagation in the PPLN, excited by a collimated beam (positive phase mismatch i. e. crystal temperature = 21.5 $^{\circ}\text{C}$), and input pump intensity = 0.85 GW/cm^2). The linear input SOP is set parallel to the crystal extraordinary axis. The round inset image has the same scale than the square image.

I choose to show the output beam evolution in a PPLN crystal at room temperature (21.5 °C) i. e. for positive phase mismatch conditions, rather than at phase matching conditions (60 °C) because the results were better visible in the first condition. Nevertheless the soliton was also observed at phase matching.

The experimental data of ΔkL versus temperature are not sufficiently sampled to precisely calculate the value of the phase mismatch in multiple of π (see Figure 28-(b)), due to a low precision of the oven I used to heat the PPLN. I will then report the values of temperature and not the values of ΔkL .

At phase matching conditions, the intensity threshold for the quasi soliton is 0.1 GW/cm² in PPLN, which seems the same than in KTP, despite of a higher nonlinear coefficient. The pulse energy sensor I used (OPHIR PE10BB) was not enough precise for low energy levels. Thus, it is hard to compare precisely the soliton appearance threshold between the KTP and the PPLN.

The diameter of the soliton is very close to the one obtained in the KTP (~50 μm at $1/e^2$ of intensity). For a positive phase matching (21.5 °C), the soliton local intensity is 2 times higher than the top of the remaining pump (see Figure 45-(b)).

The same figure shows that the soliton starts disappearing for a pump intensity threshold of 1 GW/cm² (versus 0.8 GW/cm² in the KTP). As in the KTP, no traces on the FF soliton remain visible in the PPLN at high power (see Figure 45). Only the SH beam keeps track of the nonlinear evolution. The soliton in PPLN starts disappearing at a pump intensity higher than in KTP, despite of the PPLN higher nonlinearity. This suggests that the PPLN soliton would be more stable because of the absence of spatial walk-off in such medium.

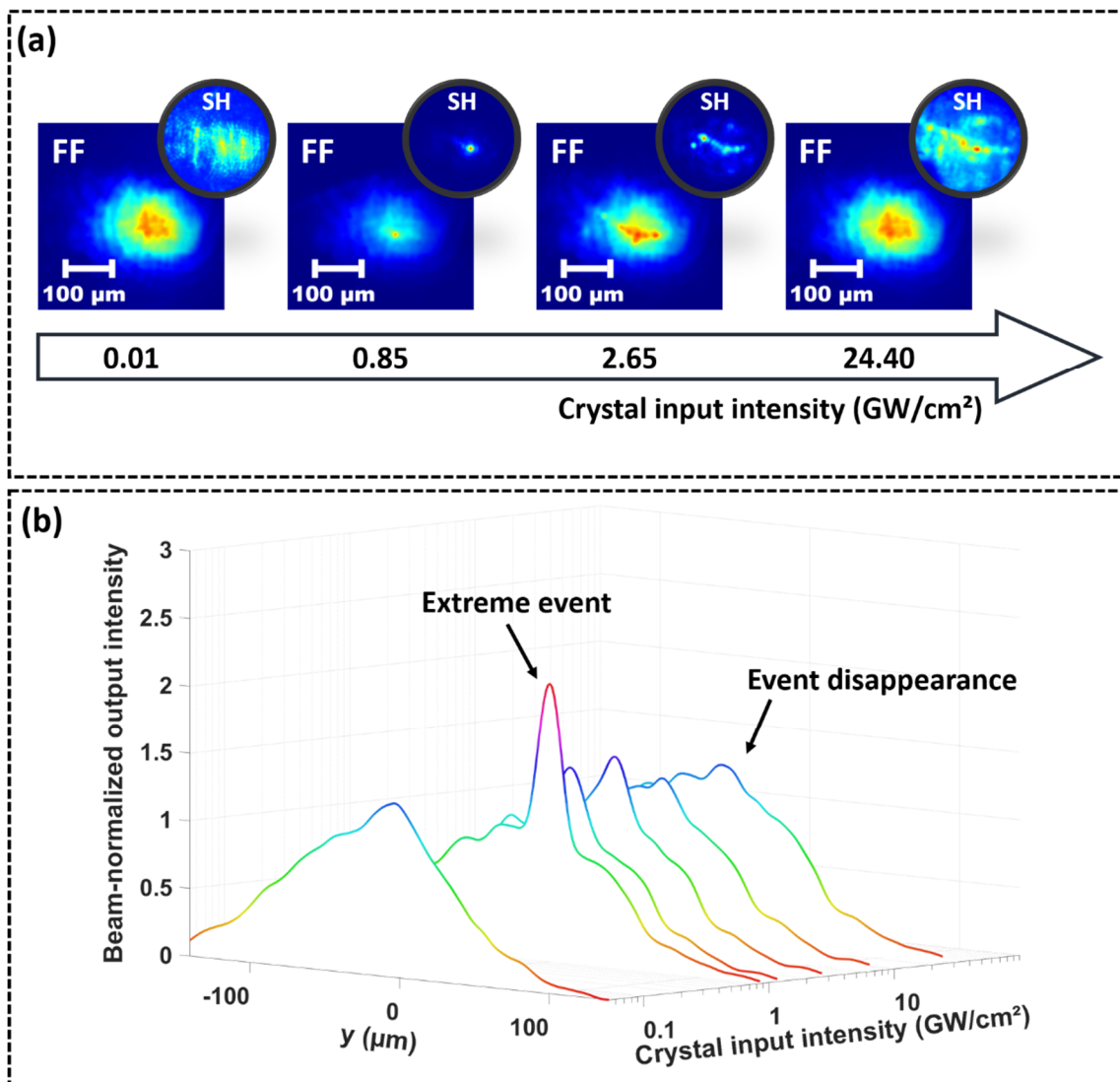


Figure 45: **(a)**-2D output beam images of the FF and SH beams at the end face of the PPLN versus the input pump intensity (the round inset images have the same scale than the square images). **(b)**-1D output profiles evolution of the FF beams versus the input pump intensity. The linear input SOP is set parallel to the crystal extraordinary axis. Positive phase mismatch configuration (21.5 °C).

Conclusion – Chapter III

In this chapter, I have discussed the appearance and disappearance of a 2D spatial soliton. This ephemeral extreme event has been obtained thanks to a large non-diffractive infrared beam, launched into KTP and PPLN crystals, cut for type II and type 0 SHG, respectively.

The soliton is sensitive to the initial conditions i. e. polarization state, input pump intensity, phase mismatch conditions. In both crystals, I was able to generate a focused and localized FF beam out of the crystal with a size 8 times smaller than the initial pump beam and with a local peak intensity reaching 2.4 times the one on top of the pump.

This spatial soliton remains unchanged upon propagation in the crystal for a moderate power while it vanishes for a higher intensity.

I also investigated the temporal and spectral profile evolution of the trapped beam. In the temporal domain I first identified a pulse compression followed by a pulse breaking process, appearing for similar pump intensity of the spatial event disappearance. In the spectral domain, a broadening around the FF and SH frequencies was obtained because of the nonlinear process.

I then discussed on the transient nature of that spatial self-trapping and compared its evolution with the one described with $\chi^{(3)}$ and $\chi^{(2)}$ susceptibilities respectively.

In all cases, our nonlinear wave seems significantly different from the Peregrine soliton even if we can underline similarities in its ephemeral behavior. The 2D nature of our process, observed at the exact phase matching, forbids any analytical description or simplification in the mathematical approach by using cascading approximation. The appearance of that event without any injected input background is also a huge difference with Peregrine soliton. The disappearance of my soliton is not completely understood even if I observed strong instabilities in the temporal domain at the disappearance power level. A theoretical paper written by A.V. Buryak *et al.* mention the finite range of existence of quadratic solitons in terms of power (hence intensity), but this time only for a high imbalance between the FF components [17], while my experiments also show disappearance for balanced FF's.

In the next chapter, I will discuss more precisely the spatial instabilities observed on the SH beam and determine a possible competition with temporal instabilities.

Bibliography – Chapter III

- [1] Solli, D. R., Ropers, C., Koonath, P., & Jalali, B. (2007). Optical rogue waves. *Nature*, 450(7172), 1054-1057.
- [2] Schiek, R., & Baronio, F. (2019). Spatial Akhmediev breathers and modulation instability growth-decay cycles in a quadratic optical medium. *Physical Review Research*, 1(3), 032036.
- [3] Torruellas, W. E., Wang, Z., Hagan, D. J., VanStryland, E. W., Stegeman, G. I., Torner, L., & Menyuk, C. R. (1995). Observation of two-dimensional spatial solitary waves in a quadratic medium. *Physical review letters*, 74(25), 5036.
- [4] Fuerst, R. A., Lawrence, B. L., Torruellas, W. E., & Stegeman, G. I. (1997). Beam reshaping by use of spatial solitons in the quadratic nonlinear medium KTP. *Optics letters*, 22(1), 19-21.
- [5] Pliszka, P., & Banerjee, P. P. (1993). Nonlinear transverse effects in second harmonic generation. *JOSA B*, 10(10), 1810-1819.
- [6] Trillo, S., & Ferro, P. (1995). Modulational instability in second harmonic generation. *Optics letters*, 20(5), 438-440.
- [7] Corney, J. F., & Bang, O. (2001). Modulational instability in periodic quadratic nonlinear materials. *Physical review letters*, 87(13), 133901.
- [8] Schiek, R., Fang, H., Malendevich, R., & Stegeman, G. I. (2001). Measurement of modulational instability gain of second-order nonlinear optical eigenmodes in a one-dimensional system. *Physical review letters*, 86(20), 4528.
- [9] Delqué, M., Fanjoux, G., Gorza, S. P., & Haelterman, M. (2011). Spontaneous 2D modulation instability in second harmonic generation process. *Optics Communications*, 284(5), 1401-1404.
- [10] Torner, L., Torruellas, W. E., Stegeman, G. I., & Menyuk, C. R. (1995). Beam steering by χ (2) trapping. *Optics letters*, 20(19), 1952-1954.
- [11] Torruellas, W. E., Assanto, G., Lawrence, B. L., Fuerst, R. A., & Stegeman, G. I. (1996). All-optical switching by spatial walk off compensation and solitary-wave locking. *Applied physics letters*, 68(11), 1449-1451.
- [12] Clausen, C. B., & Torner, L. (1999). Spatial switching of quadratic solitons in engineered quasi-phase-matched structures. *Optics letters*, 24(1), 7-9.
- [13] Carrasco, S., Polyakov, S., Kim, H., Jankovic, L., Stegeman, G. I., Torres, J. P., ... & Eger, D. (2003). Observation of multiple soliton generation mediated by amplification of asymmetries. *Physical Review E*, 67(4), 046616.
- [14] Karamzin, Y. N., & Sukhorukov, A. P. (1974). Nonlinear interaction of diffracted light beams in a medium with quadratic nonlinearity: mutual focusing of beams and limitation on the efficiency of optical frequency converters. *ZhETF Pisma Redaktsiiu*, 20, 734.
- [15] Kibler, B., Fatome, J., Finot, C., Millot, G., Dias, F., Genty, G., ... & Dudley, J. M. (2010). The Peregrine soliton in nonlinear fibre optics. *Nature Physics*, 6(10), 790-795.

- [16]Baronio, F. (2017). Akhmediev breathers and Peregrine solitary waves in a quadratic medium. *Optics letters*, 42(9), 1756-1759.
- [17]Buryak, A. V., Kivshar, Y. S., & Trillo, S. (1997). Parametric spatial solitary waves due to type II second-harmonic generation. *JOSA B*, 14(11), 3110-3118.

Chapter IV. Analysis of the spatial instabilities at the second harmonic

IV.1. Context

New mechanism of nonlinear extreme waves generation, with peculiar statistical properties, is of fundamental scientific interest, and could be used for technological applications as structured-illumination imaging, i. e. dynamic speckle illumination microscopy [1], super-resolution imaging [2], or pseudo-thermal light sources for high-order ghost imaging [3]. Similar structured light sources, and their applications, were discussed by Bender et al. in 2018 [4]. In the paper, they informed the reader of the interest for generating speckled beams, with statistics differing from a classical Rayleigh distribution (see Goodman *et al.* [5] for more information on such distributions). Nonlinear waves, including rogue waves, have also been recently proposed for computing reservoirs by Marcucci et al. in 2020 [6].

In my case, I demonstrated that a 2D soliton could spontaneously appear and disappear when using a strong collimated beam in a quadratic media. If the FF beam seems to be not so much affected by the disappearance of the soliton, the situation is completely different for the SH, which exhibits a speckled shape.

This SH speckle could be related with a wave breaking process, identified in the temporal domain. It could also be related to the disappearance of the soliton. I am presenting, in the present chapter, a complete study of the SH beam evolution upon the input intensity [7].

IV.2. Setup

In these works, I used the same optical bench as the one previously presented, in chapter III, for spatial observation of solitons (Figure 27). The experimental conditions are slightly different for the case of Figure 48, where the injected pump beam had an input diameter of $460\ \mu\text{m}$ ($1/e^2$) rather than $400\ \mu\text{m}$, and where the magnification of the output optical system was 7.5.

IV.3. Analyze of the speckle in KTP crystal

Because of the shallow nonlinear modulation on the FF beam, I preferred to analyze only the SH beam, which was much more affected by the nonlinear processes.

I recorded the shape of the output SH beam for different pump intensities. The results are shown in Figure 46. I set the crystal angle close to the phase matching condition ($\theta = 90^\circ$, $\Phi = 23.5^\circ + 0.33^\circ$), where the nonlinear regime is focusing.

At low input pump intensity (0.04 GW/cm^2) i. e. in the case of low depletion of the initial FF pump, the beam at the SH has a Gaussian profile with a diameter close to 0.7 time the one of the FF.

I observed, at 0.11 GW/cm^2 , a spatial self-focusing at the SH frequency (Figure 46-(a-c)): the beam diameter at $1/e^2$ in intensity decreases down to $50 \mu\text{m}$, which is the diameter of the FF soliton observed in chapter III.

By increasing the pump intensity beyond 0.8 GW/cm^2 , I observed the splitting of the SH beam into a pattern of randomly localized spots (Figure 46-(d-f)). Such intensity distribution is similar to the speckle beams commonly obtained with a diffusing plate; in my case, the speckle is obtained by means of a quadratic nonlinear dynamics. I can observe the speckle formation in a large range of phase mismatch values, i. e. from $\Delta kL = -9\pi$ to $\Delta kL = +9\pi$.

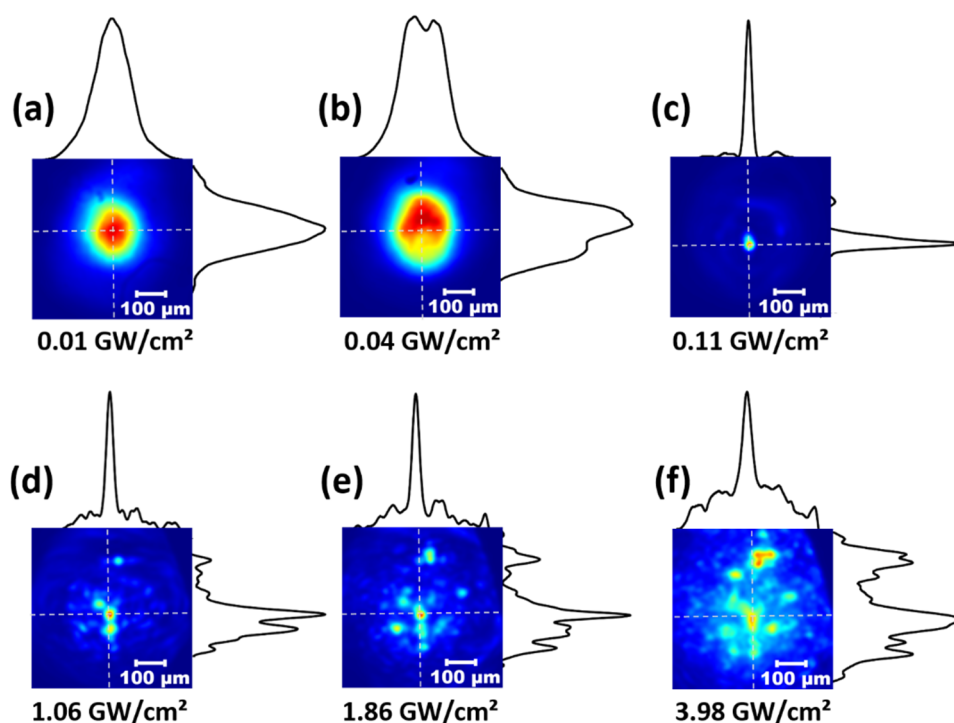


Figure 46: Image of the SH beam, after propagation in the KTP, versus the FF pump intensity. $\Delta kL = 2\pi$ and linear input SOP of 47° .

I managed to characterize the speckle statistical distribution in each image obtained with the camera. I calculated the scintillation index given by the following expression:

$$S_{SHG} = \frac{\langle I_{SHG}^2 \rangle - \langle I_{SHG} \rangle^2}{\langle I_{SHG} \rangle^2} \quad (4.1)$$

Where $\langle \rangle$ designates the average over each pixel samples of one image.

In the case of Rayleigh classical speckle patterns, obeying to Gaussian statistics, $S_{SHG} = 1$. In the case of the intensity speckles pattern in Figure 46, $S_{SHG} = 1.11$ for a pump intensity of 1.1 GW/cm² (Figure 46-(d)). The beam scintillation index dropped to $S_{SHG} = 0.74$ for an input pump intensity set higher than 1.9 GW/cm² (Figure 46-(e)).

On Figure 47, I illustrated the pixel intensity statistics at four different pump intensities (out of the six selected ones of Figure 46). At each level of pump intensity, the histogram of the SH beam intensity was reported in log and linear scales (square inset). In order of simplifying the comparison, the corresponding SH beams images are shown on round insets.

In Figure 47-(b-c), the dashed curves represent the negative-exponential Probability Density Function (PDF) $p(I)$ [5]:

$$p(I) = \frac{1}{\langle I \rangle} e^{-\frac{I}{\langle I \rangle}} \quad (4.2)$$

The four images displayed in the Figure 47 show consequences of the quadratic nonlinear conversion leading to SH speckle. In the particular case of a pump intensity of 1.1 GW/cm², the PDF (Figure 47-(b)) is very close to the one obtained for Rayleigh speckles pattern. The corresponding scintillation index also agrees accordingly, with a value close to 1. Figure 47-(d) instead, displays speckle PDFs very far from Rayleigh distribution, for a high pump intensity of 4 GW/cm².

These cases show how in principle the speckle statistics can change by simply changing the pump intensity. The PDF tails also give very important information on extreme spatial waves [8]. In my case, such waveforms are related to the high energy focused SH beam.

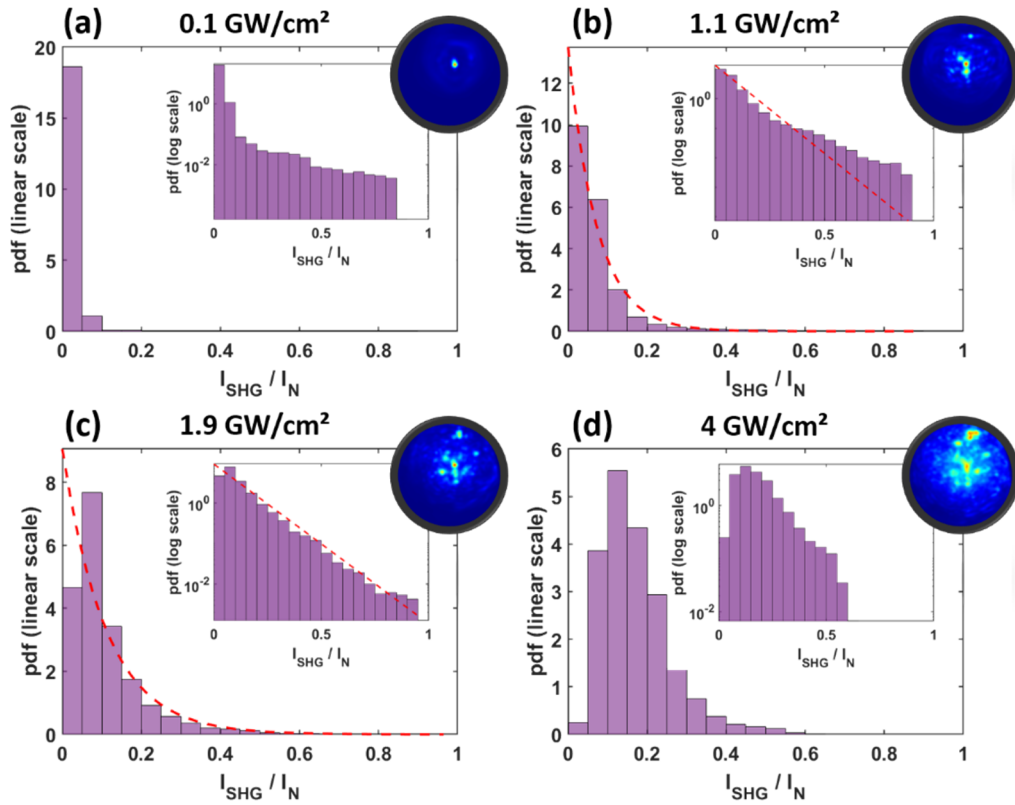


Figure 47: SH beams intensity levels, PDFs, obtained in KTP crystal at different input pump intensities. On those histograms, I normalized the intensity axis of the beams at the SH, according to the maximum allowed level of the 8-bit camera device ($I_{\text{SHG}} / I_{\text{N}}$). I avoided camera saturation by reducing the crystal output light intensity with a variable attenuator. For each value of pump intensity **(a-d)**, the attenuation was modified in front of the camera. $\Delta k_L = 2\pi$, input linear SOP = 47° .

Those statistics were made on multiple pixels but only on one image each time. In order to obtain more precise values, I recorded a set of 10000 images for the same initial conditions. Thus, the position of the spots light evolves slightly versus time, however, the beam pattern remains stable shot-to-shot. The main bright spots keep the same spatial localization. This demonstrates that the spatial speckle distribution remains unchanged for similar input excitation conditions, like in a linear scattering process.

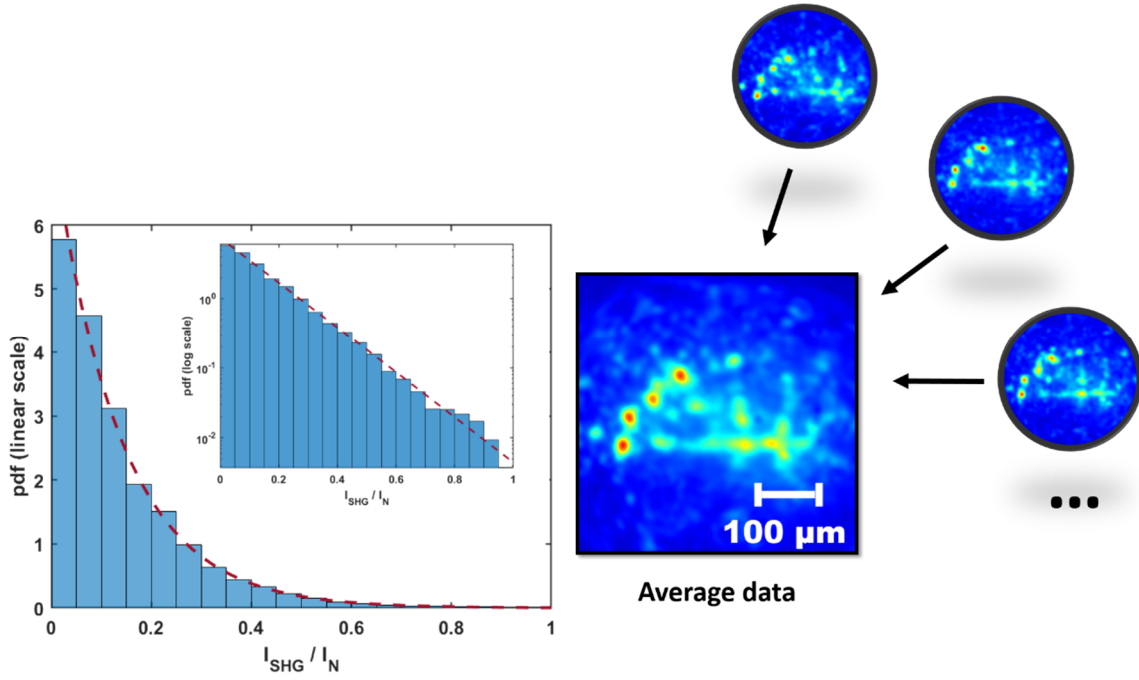


Figure 48: SH beam intensity level (average data of a set of 10000 laser shot), PDF, obtained in KTP crystal for a pump intensity of 3.6 GW/cm². On the histogram, I normalized the intensity axis of the average data beam at the SH frequency, according to the maximum allowed level of the 8-bit camera device. I avoided camera saturation by reducing crystal output light intensity with variable attenuator. Due to the important light density between the spots, a background compensation was used for PDF calculation. The linear input SOP remains unchanged, $\Delta kL = 3\pi$.

The Figure 48 shows that on a multiple data set, it is possible to observe a histogram very close to the analytical calculus from equation (4.2), meaning that the average of all of the output SH beams impacted instabilities is a quasi-perfect Rayleigh speckle, which is confirmed by the intensity distribution histogram of the 10000 beams average results.

In a purpose of measuring speckle spots size mean value, I calculated the intensity correlations of the images shown in Figure 46, for three different values of pump intensity (see Figure 49). Starting from the SH image distribution $I_{SHG}(x, y)$, with x and y the pixel images coordinates, I first used the intensity mean values to calculate its deviation: $\delta I_{SHG} = I_{SHG} - \langle I_{SHG} \rangle$. In a second step, the corresponding deterministic intensity correlation $C_i(\Delta x, \Delta y)$ was calculated.

$$C_i(\Delta x, \Delta y) = \iint_{-\infty}^{+\infty} \delta I_{SHG}(x, y) \delta I_{SHG}(x + \Delta x, y + \Delta y) dx dy \quad (4.3)$$

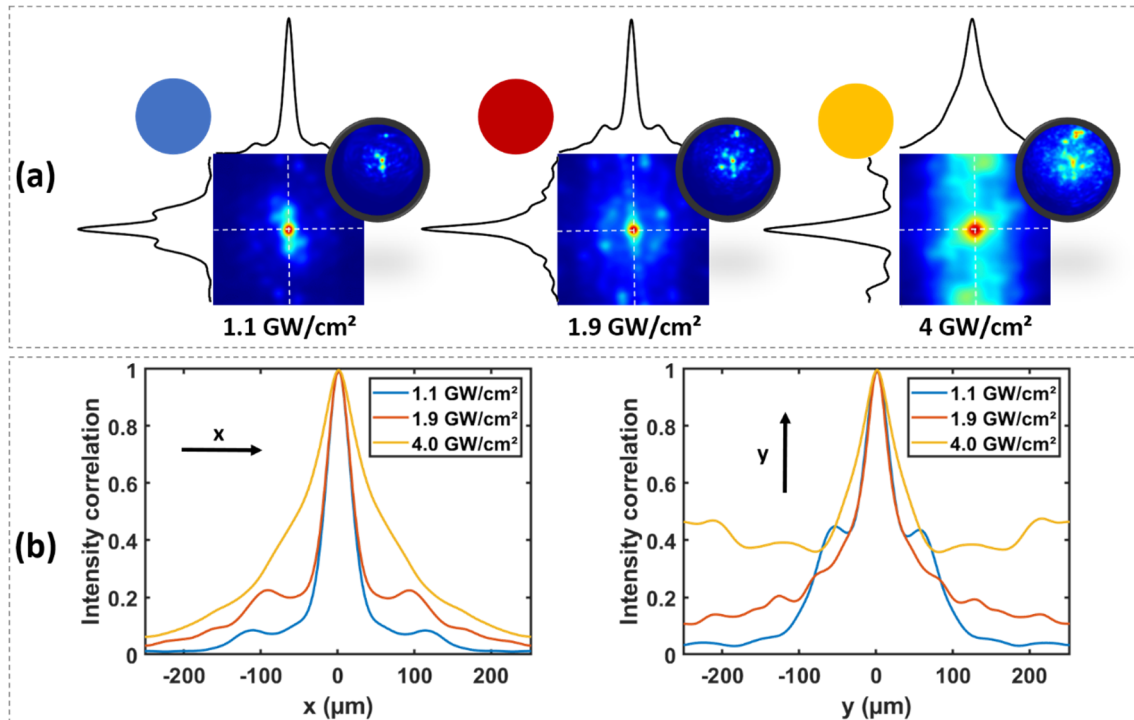


Figure 49: **(a)**-Intensity correlations C_I of the near-field SH images. **(b)**-Comparison of each intensity correlation spatial profiles, cut on x or on y transverse axes. $\Delta kL = 2\pi$ and linear input SOP of 47° .

Figure 49 curves reveal that the correlation, which is related to the elementary intensity spots which compose the speckle, remains nearly unchanged for a pump intensity variation from 1.1 GW/cm^2 to 1.9 GW/cm^2 , despite few differences in the PDFs. When I set the pump intensity to higher values, like 4 GW/cm^2 , the deterministic spatial intensity correlation shows that the size of the spots is continuously increasing with the input pump intensity.

Long-range correlation is also increasing, as the pump intensity grows larger. Indeed, at 4 GW/cm^2 , I noticed that the large pump intensity boosted the SH beam breakup. One could argue that, for high pump intensity, each filament filled the gap between each other, leading to the speckle contrast reduction.

This atypical evolution seems to anticipate that the initial SH speckle can progressively disappear under the nonlinear quadratic action, leading to a second nonlinear spatial reshaping able to counterbalance the speckle formation. In order to prove it, it would be necessary to increase further the pump power. However it was no longer possible since I reached the damage threshold of my KTP crystal. I decided then to carry out the same study in a PPLN, because of its higher nonlinear coefficient.

IV.4. Spatial speckle reshaping in PPLN crystal

In order to increase the nonlinearity response, I analyzed the SH speckle evolution, versus the pump intensity, by replacing the KTP crystal with a PPLN crystal. The damage threshold of the PPLN is estimated to be 5 times lower than the one of KTP [9].

The experimental observations are summarized in Figure 50, showing the evolution of the spatial SH shape while increasing the input FF pump intensity. In Figure 50-(a), the SH beam is totally dispersed into multiple spots for a pump intensity of 2.7 GW/cm^2 . The speckle distribution evolves while I increase the input pump intensity. For a pump intensity threshold of 16 GW/cm^2 , the SH speckle disappears: the SH beam spatial breakup is significantly reduced, increasing the SH beam brightness.

A confirmation of its evolution is obtained by measuring the SH spatial beam profile both in near and far fields for two different intensities (see Figure 50-(b-c), at 2.6 GW/cm^2 and 51 GW/cm^2 respectively).

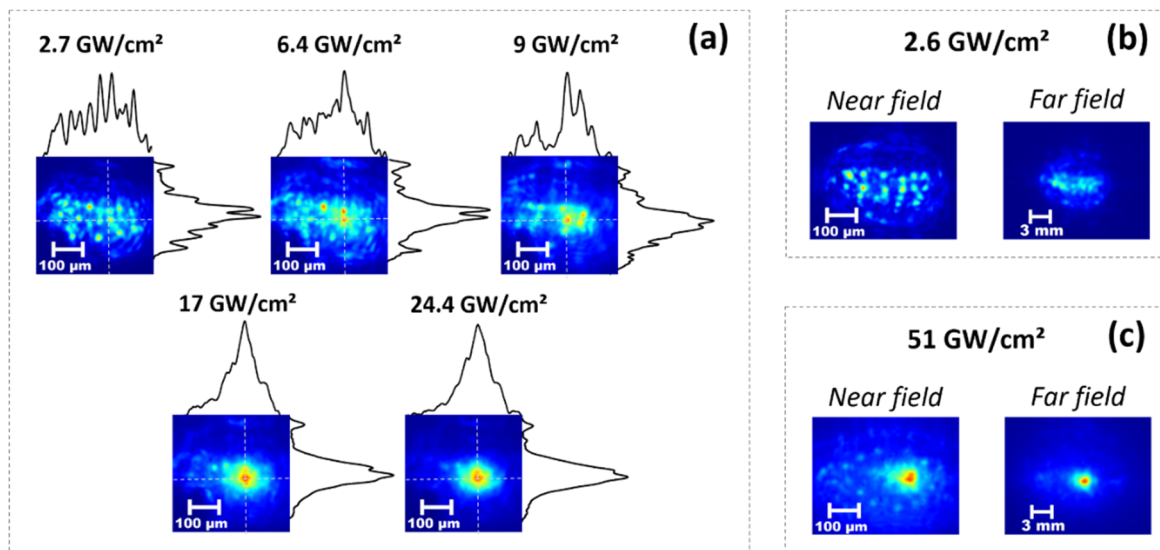


Figure 50: **(a)**-Near-field images of the PPLN output SH beam, for different values of pump intensity. Near and far fields of the SH for **(b)**-Pump intensity = 2.6 GW/cm^2 , **(c)**-Pump intensity = 51 GW/cm^2 . Such experimental results are at the phase matching conditions. The linear input SOP is set parallel to the crystal extraordinary axis.

It is also important to note that this SH beam reshaping, observed only in the PPLN crystal, is accompanied by a spectral broadening around the SH frequency, extending on more than 150 nm from the blue to the red wavelengths (see Figure 51). The newly generated colors

inherit the Gaussian shape of the FF pump, as we can see on Figure 51-(e). At the same time, the FF undergoes similar evolution with a spectral broadening between 900 nm and 1300 nm, in the best case, i. e. around 51 GW/cm² (see Figure 52).

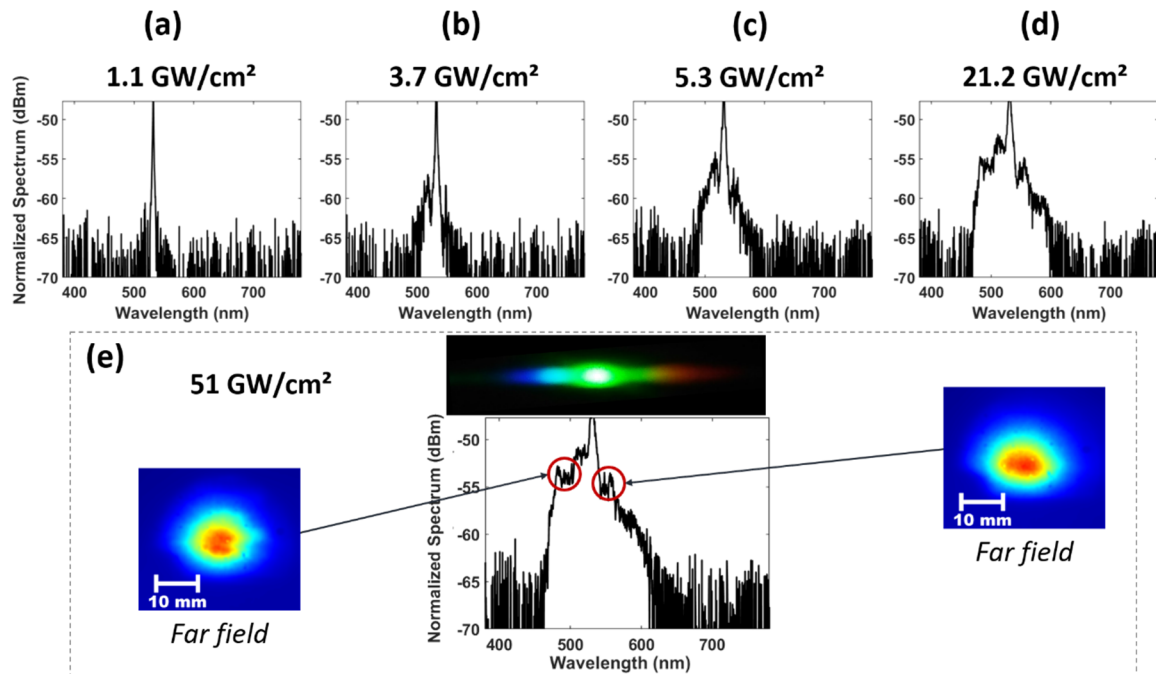


Figure 51: **(a-d)**-SH beams spectral evolution, for different pump intensity values. **(e)**-SH beam spectrum for an input pump intensity of 51 GW/cm² and corresponding beam images. Both insets are the far-field beam images at 500 nm (**left**) and 550 nm (**right**), respectively. Such experimental results are at the phase matching conditions. The linear input SOP is set parallel to the crystal extraordinary axis.

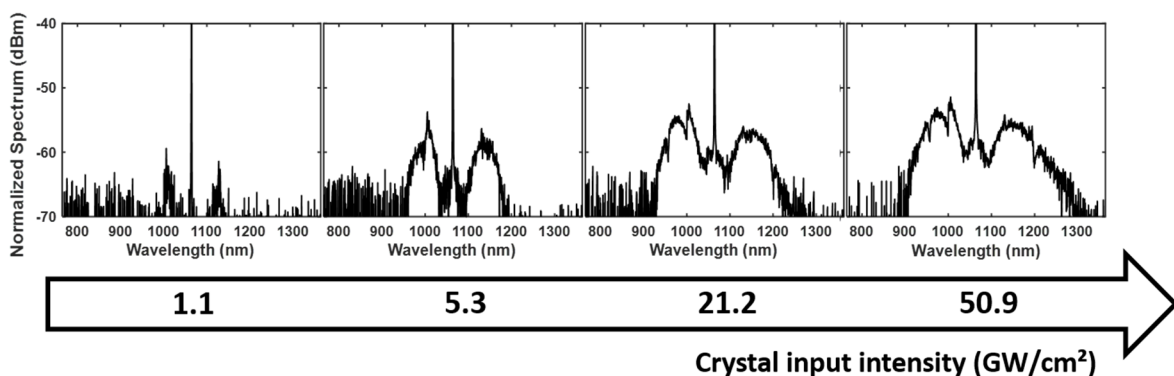


Figure 52: Spectral broadening evolution versus pump intensity, around the FF. Such experimental results are at the phase matching conditions. The linear input SOP is set parallel to the crystal extraordinary axis.

These results remind those obtained by Katarzyna Krupa *et al.* in the paper entitled *Polychromatic filament in quadratic media: spatial and spectral shaping of light in crystals* [10]. K. Krupa *et al.* explained the spectral broadening dynamic in the PPLN crystal by multiple conversions between the FF and the SH (see Figure 53). Indeed, while propagating in the crystal, the waves involved in the nonlinear three-wave mixing process exchange energy to each other. When the spectrum grows larger around the SH wavelength, a part of the energy of the newly generated colors will flow-back to the FF, but with a spectral shift. This leads to the particular spectral shape I obtained, around the FF, in Figure 52.

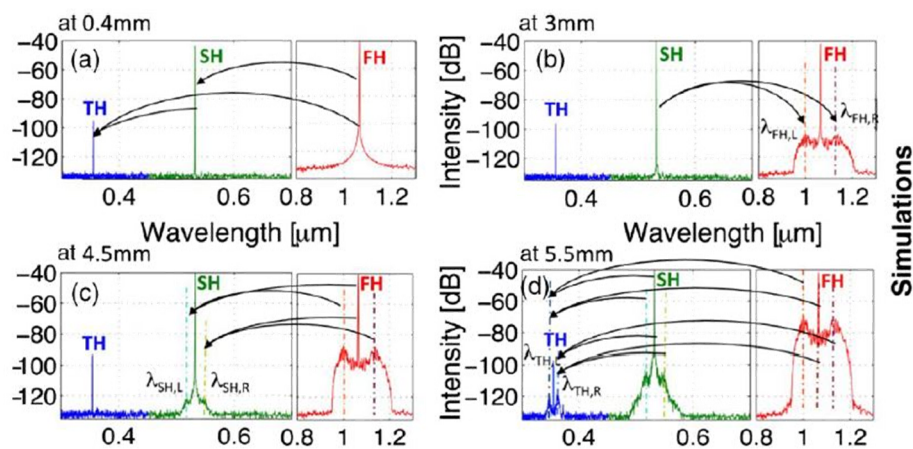


Figure 53: Numerical simulation of the spectral evolution along the propagation length of a PPLN crystal. L and R are respectively the anti-Stokes and the Stokes waves. Phase mismatch conditions ($\Delta kL = -3\pi$), and pump intensity = 1 GW/cm². This figure is extracted from Ref [10].

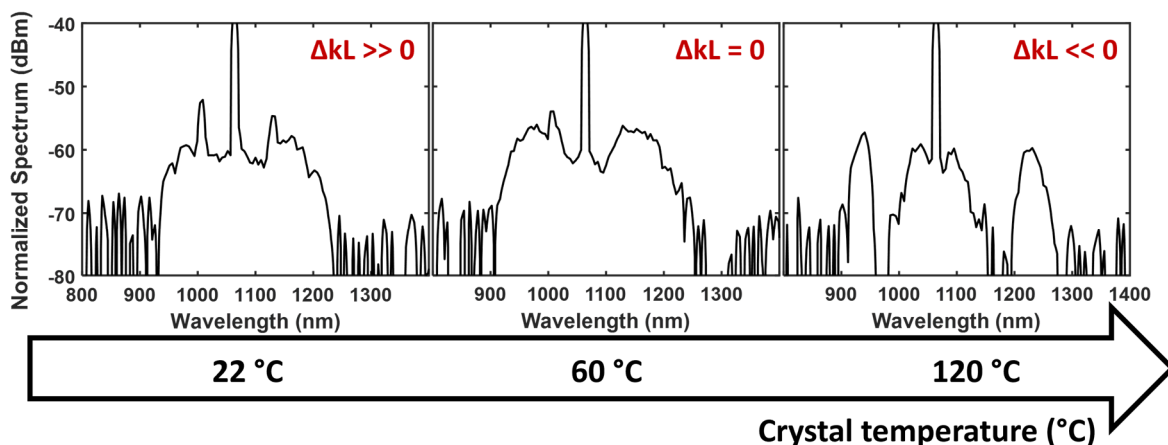


Figure 54: Beam spectral evolution, function of crystal temperature i. e. ΔkL . The pump intensity is of 24.4 GW/cm². The linear input SOP is set parallel to the crystal extraordinary axis.

As reported by Krupa *et al.* [10], the spectral broadening around the FF and the SH significantly evolves with the phase matching conditions, meaning that I can shape the output light spectrum, around the FF and the SH, by controlling the crystal temperature. In my experiments, I observed that the sidebands moved away from the FF while I increased the temperature of the PPLN (see Figure 54).

IV.5. Discussion

In my experiment, I observed that a SH Gaussian beam, generated from FF Gaussian pump, can be drastically reshaped into a speckle beam having characteristics similar to those generally observed at the output of a diffusing plate. However, such evolution is obtained under the influence of noise and because of spatial instabilities [11]. Such tendency of multi filamentation leading to a speckled output can be completely reversed by increasing the FF pump intensity and the material nonlinearity, leading to a spectacular quadratic spatial reshaping. The disappearance of the spatial instabilities seems to be due to a competition with temporal instabilities able to broaden both the FF and the SH beams [10].

If the cascading process between the FF and the SH is well known to induce a spatial phase in the transverse domain, this process is also possible in the time domain. It creates then a spectral broadening in the vicinity of the two bands. If these two effects appear separately in my experiment and seem to compete one with each other, they can also be obtained simultaneously as demonstrated by Krupa *et al.* [10]. In this case, the initial conditions were significantly different with an excitation of the crystal by a focused initial beam.

An explanation of the spectral broadening, which appears in parallel to the spatial beam cleanup, was made by Barviau *et al.* [12], considering the process of thermalization; since the entropy cannot decrease in a conservative system (for example a nonlinear crystal), the beam cleanup only happens if there is instabilities energy transfer from the spatial to the temporal domain, leading to:

- The diminishment of the energy in higher order light modes (the spatial instabilities decrease because their energy is transferred to temporal instabilities).
- The broadening of the spectrum (the temporal instabilities increase because they are receiving energy from spatial instabilities).

Conclusion – Chapter IV

To conclude, I showed in my experiments that a Gaussian SH beam, obtained from a non-diverging FF beam in a quadratic crystal, could be broken into many spots, creating then a speckled beam. By carrying out the statistical analysis of such waveforms, I showed that the statistical properties of the spatial spots were partly driven by the crystal input FF beam intensity level, as I kept the linear polarization and the crystal direction fixed with respect of the medium crystallographic neutral axes.

In addition to those interesting spatial light dynamics, it was also possible to observe a reorganization of the SH speckle as the pump intensity was increasing above a certain power threshold. This spatial quadratic beam cleaning was accompanied in parallel by a strong spectral broadening in the visible and infrared domains.

That complex spatiotemporal process could also be at the origin of the disappearance of the soliton previously obtained after self-focusing process. Indeed, a pulse breaking process has been clearly identified when the soliton starts to disappear. In these conditions, we think that the appearance and disappearance of extreme events, such as quadratic solitons, can be affected by spatiotemporal dynamics integrating competition between temporal and spatial instabilities.

We can also underline that the intensity coupled in the PPLN is higher than the one launched in the type II KTP crystal, in spite of the larger damage threshold for the KTP [9]. This could be due to the spectral broadening, obtained on the whole transparency windows, which acts as limiting peak power because of the pulse breaking phenomenon.

Such spectral dynamics finds interesting applications in all fields where new colors generation are required, as for example in developing new, very usable and all-purpose light sources for operations, ranging from multispectral LIDAR measurements to nonlinear fluorescence imaging. The spectral broadening obtained in the PPLN crystal has been used in my laboratory in collaboration with Sahar Wehbi for M-CARS experiments [13]. Additionally, nonlinear speckled beams can find important applications in fields requiring the control of light speckle, as in microscopy [14] or in all-optical computing (as a reservoir of light bits) [15].

Bibliography – Chapter IV

- [1] Ventalon, C., & Mertz, J. (2006). Dynamic speckle illumination microscopy with translated versus randomized speckle patterns. *Optics express*, 14(16), 7198-7209.
- [2] Oh, J. E., Cho, Y. W., Scarcelli, G., & Kim, Y. H. (2013). Sub-Rayleigh imaging via speckle illumination. *Optics letters*, 38(5), 682-684.
- [3] Zhang, E. F., Liu, W. T., & Chen, P. X. (2015). Ghost imaging with non-negative exponential speckle patterns. *Journal of Optics*, 17(8), 085602.
- [4] Bender, N., Yilmaz, H., Bromberg, Y., & Cao, H. (2018). Customizing speckle intensity statistics. *Optica* 5, 595–600.
- [5] Goodman, J. W. (1976). Statistical properties of speckle in monochromatic light (A). *Journal of the Optical Society of America (1917-1983)*, 66, 176.
- [6] Marcucci, G., Pierangeli, D., & Conti, C. (2020). Theory of neuromorphic computing by waves: machine learning by rogue waves, dispersive shocks, and solitons. *Physical Review Letters*, 125(9), 093901.
- [7] Jauberteau, R., Wehbi, S., Mansuryan, T., Krupa, K., Baronio, F., Wetzel, B., ... & Couderc, V. (2021). Boosting and Taming Wave Breakup in Second Harmonic Generation. *Frontiers in Physics*, 9, 106.
- [8] Pierangeli, D., Di Mei, F., Conti, C., Agranat, A. J., & DelRe, E. (2015). Spatial rogue waves in photorefractive ferroelectrics. *Physical review letters*, 115(9), 093901.
- [9] <https://www.covesion.com> and <http://www.mt-berlin.com>
- [10] Krupa, K., Labruyère, A., Tonello, A., Shalaby, B. M., Couderc, V., Baronio, F., & Aceves, A. B. (2015). Polychromatic filament in quadratic media: spatial and spectral shaping of light in crystals. *Optica*, 2(12), 1058-1064.
- [11] Fuerst, R. A., Baboiu, D. M., Lawrence, B., Torruellas, W. E., Stegeman, G. I., Trillo, S., & Wabnitz, S. (1997). Spatial modulational instability and multisolitonlike generation in a quadratically nonlinear optical medium. *Physical review letters*, 78(14), 2756.
- [12] Barviau, B., Kibler, B., Coen, S., & Picozzi, A. (2008). Toward a thermodynamic description of supercontinuum generation. *Optics letters*, 33(23), 2833-2835.
- [13] Wehbi, S., Mansuryan, T., Jauberteau, R., Tonello, A., & Krupa, K. Versatile supercontinuum generation by using χ (2) and χ (3) nonlinearities in PPLN crystal for direct multiplex CARS measurement. In *Proc. of SPIE Vol (Vol. 11770, pp. 1177017-1)*.
- [14] Pascucci, M., Ganesan, S., Tripathi, A., Katz, O., Emiliani, V., & Guillon, M. (2019). Compressive three-dimensional super-resolution microscopy with speckle-saturated fluorescence excitation. *Nature communications*, 10(1), 1-8.
- [15] Dong, J., Rafayelyan, M., Krzakala, F., & Gigan, S. (2019). Optical reservoir computing using multiple light scattering for chaotic systems prediction. *IEEE Journal of Selected Topics in Quantum Electronics*, 26(1), 1-12.

Chapter V. Generation of multiple spatial quadratic solitons

V.1. Spontaneous emission of multiple quadratic solitons

Beyond the spatial self-focusing, quadratic soliton propagation and spatiotemporal instabilities, all obtained at phase matching condition, I also observed another interesting effect at phase matching: a spatial switching for an exact energy splitting between the two principal axes of the KTP crystal (i. e. for a polarization angle of the input beam at exact 45°). This particular process has been reported in 1996 by Torruellas *et al.* [1]. However, by modifying the crystal angle, in order to be at phase mismatch conditions, I also observed the generation of multiple spatial solitons in KTP crystal.

The experimental setup used here is similar to the one used in the first experiment presented in chapter III. A KTP crystal is excited with a large collimated beam at 1064 nm and with pulses of 30 ps. The input peak power, polarization orientation and phase-mismatch are varied in the experiment.

The phase mismatch regime is highly favorable to the formation of multiple self-trapped beams, as quadratic solitons or extreme events. As shown in Figure 55, I obtained, in this regime, exactly the same behavior than the one obtained at the phase matching but this time in presence of a lower intensity threshold. In these conditions, the spatial self-trapping is observed at 0.05 GW/cm^2 rather than at 0.1 GW/cm^2 , as illustrated in the previous configuration (see chapter III, Figure 31). It is also important to note that, in those conditions (large positive phase mismatch), I am in the cascading regime, where the governing equations can be approximated by the NLSE (studied in chapter I) and a soliton can be described similarly to a Kerr soliton [2].

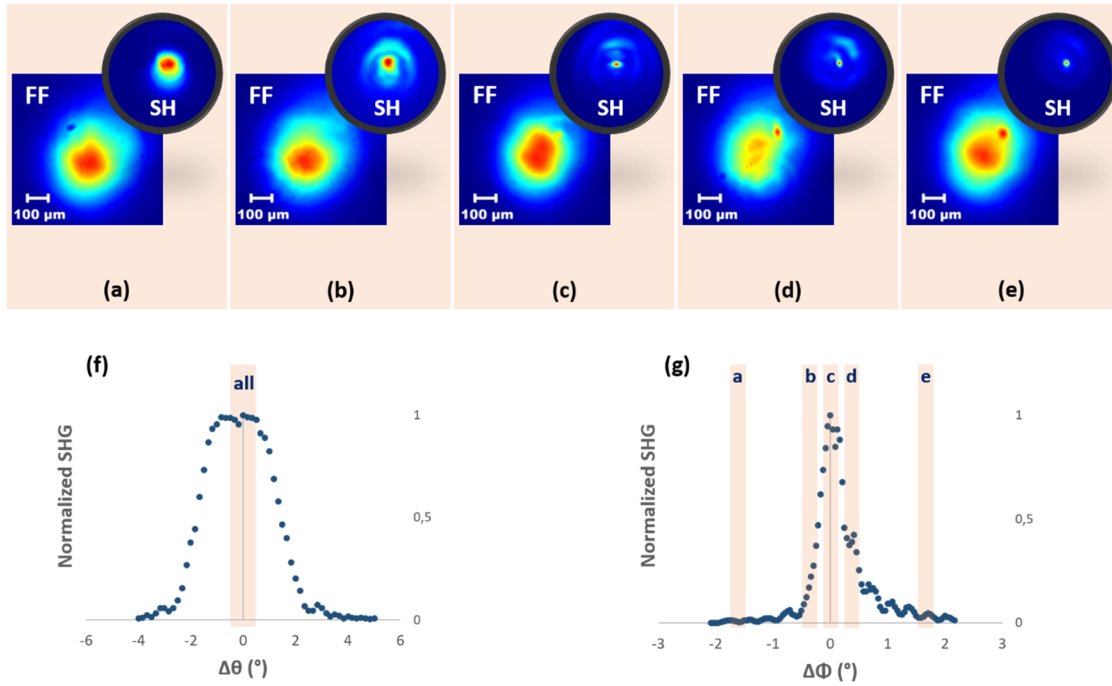


Figure 55: Profile of the output FF and SH beams versus the phase mismatch and for an input linear SOP of 47° and an input pump intensity of 0.05 GW/cm^2 . **(a)**- $\Delta\Phi = -1.67^\circ$ ($\Delta kL = -9\pi$); **(b)**- $\Delta\Phi = -0.33^\circ$, ($\Delta kL = -2\pi$); **(c)**- $\Delta\Phi = 0^\circ$ ($\Delta kL = 0$); **(d)**- $\Delta\Phi = 0.33^\circ$, ($\Delta kL = 2\pi$); **(e)**- $\Delta\Phi = 1.67^\circ$ ($\Delta kL = 9\pi$); **(f)**-Normalized SHG curve versus $\Delta\theta$; **(g)**-Normalized SHG curve versus $\Delta\Phi$.

In a second series of experiments, and keeping the previous input conditions ($\Delta kL = 9\pi$), I increased the input intensity and observed the appearance of multiple quadratic solitons. Those events share the same properties of the single soliton discussed in chapter III, that is they disappear for a very high input intensity. The diameter of these additional solitons is comparable to the single soliton case ($50 \mu\text{m}$ diameter at $1/e^2$). They appear simultaneously in opposite direction, around the central soliton (see Figure 56-(a)). The spatial separation between adjacent solitons is close to $33 \mu\text{m}$.

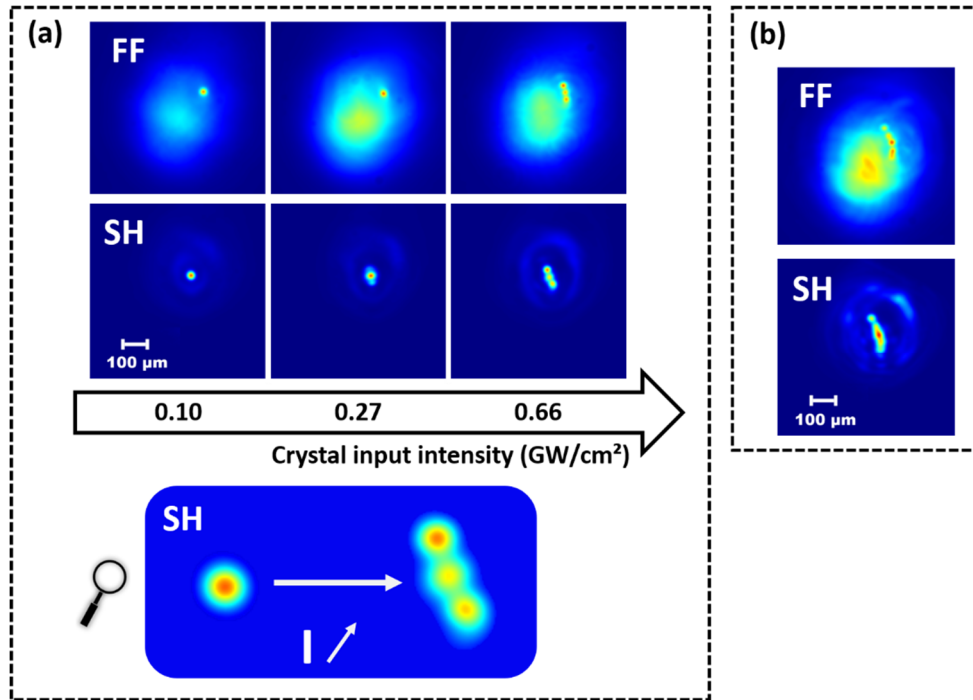


Figure 56: Multiple quadratic solitons observation. Images of the output FF and SH beams for three different input intensities, $\Delta kL = 9\pi$, input linear SOP at 47° . **(a)**-Evolution of the pump intensity from 0.1 to 0.66 GW/cm². **(b)**-Pump intensity = 1.1 GW/cm².

Because of the self-trapping effect, the three interacting waves are strongly modulated, creating in the SH a central bright spot surrounded by low energetic rings. Because of the spatial walk-off, and the spatial instability created by the trapped wave, an asymmetry is observed on the SH beam pattern. Thus, by increasing more the input intensity, for each soliton created, two additional satellite solitons appears, located at opposite positions (see Figure 56-(b)). It is important to note that, in my experiment, such chain of generation phenomena are not observed neither for phase matching, nor for negative phase mismatch.

Such intriguing process has been already observed by S. Carrasco et al. in 2003 [3] by using a periodically poled KTP crystal, close to the phase matching regime (see Figure 57-(a)). S. Carrasco et al. concluded that multiple solitons generation were mediated by the amplification of diffraction asymmetries and by anisotropy, potentially mixed with a possible presence of asymmetries in the input beam. The numerical simulations realized by Carrasco et al. [3] reproduce perfectly the nonlinear dynamics and the multiple solitons generation (see Figure 57-(b)). By increasing the pump intensity, a depletion around the center of the beam was

observed, followed by a high focusing/confinement and the appearance of rings created by the depletion.

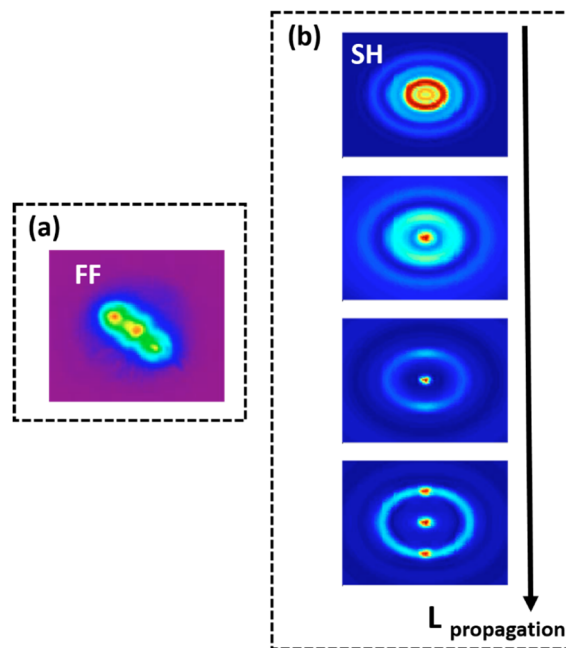


Figure 57: **(a)**-S. Carrasco experimental observations [3] at the output face of a bulk crystal (spatial 2D transverse material - 1064 nm). The input peak intensity is 23 GW/cm² **(b)**-S. Carrasco SH profiles simulations [3].

Beyond that natural multiple spatial self-trapping observation, I tried to control the phenomenon by using a periodically modulated input beam. I show this experiment in the next paragraph.

V.2. Appearance of multiple quadratic solitons by means of a spatially modulated input beam

I tried to create an artificial periodic input pattern of high intensity in order to produce multiple solitons. I used a Wollaston cube to transform a single Gaussian beam with linear polarization in two Gaussian beams perpendicularly polarized (see Figure 58-(a)). Thus, I superimposed them into the KTP crystal by means of a converging lens (10 cm) and a half-wave plate to manage the input polarization orientation. The beam x-diameter was of 400 μm (at $1/e^2$) and the modulation period visible on the output face of the crystal, which is set by the Wollaston angle (here 0.13°), was of 170 μm .

In the first case of Figure 58-(c) (output image number 1), the orientations of the input beams correspond to the principal axes of the crystal, thus no spatial interferences are observed in linear regime (see Figure 58-(b)). Moreover, the angle between the beams (due to the Wollaston prism) opposes the angle of the KTP spatial walk-off. The output beam exhibits then a circular Gaussian shape of $400\ \mu\text{m}$ of diameter ($1/e^2$).

On Figure 58-(c), image 3, I observe the output beam for a case in which the angle between the input beams is added with that of walk-off. Thus, the diameter measured on the vertical axis of the output beam is twice the diameter of the beam on Figure 58-(c), image 1.

Regarding the Figure 58-(c), images 2 and 4, the orientation of the input polarization is close to 45° . Thus, in each case, interferences are observed with either a maximum or a minimum in the central pattern.

In the experiments at high intensities, I used in turn the input conditions fixed on the second and fourth cases (image number 2 and 4 Figure 58-(c)), i. e. with interferences and a maximum/minimum in the center.

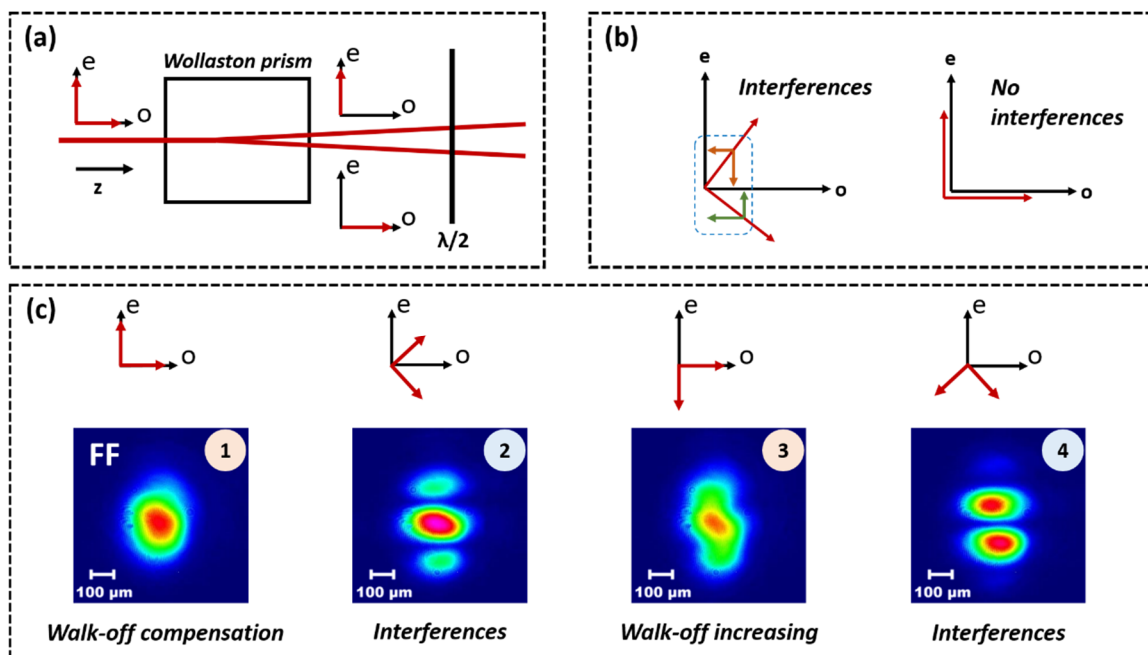


Figure 58: **(a)**-Experimental setup used to convert one beam in two with perpendicular polarization directions. **(b)**-Two different excitations of the crystal leading to spatial interferences and no interferences. **(c)**-Images of the output pattern for different linear input SOP orientation. Phase matching conditions and input pump intensity = $0.01\ \text{GW}/\text{cm}^2$.

The first set of experiment is obtained at exact phase matching and for a linear input SOP = 45° (see Figure 59). I observed the generation of several solitons, appearing in the upper right corner of the image because of the spatial walk-off. For some high intensity lobes, a pair of solitons seems to be generated. This is similar to the double soliton generation I obtained in chapter III, for the same input conditions (SOP = 45°).

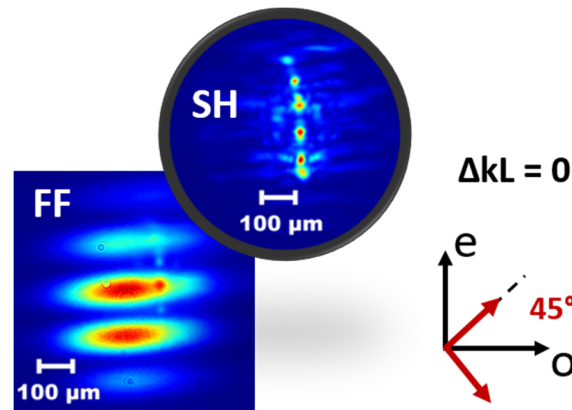


Figure 59: Soliton on a modulated pump. The FF and SH beams images are for an input pump intensity of 0.66 GW/cm². Phase matching conditions and linear input SOP = 45°.

We saw in chapter III that the soliton generation was improved when the linear input SOP was different from 45°, i. e. when there was an unbalance between the two orthogonally polarized FF components injected in the crystal. Thus, in order to facilitate the self-trapping and to keep high fringes contrast, I fixed the SOP to 59°. This way, I obtained a single soliton for each bright fringe (see Figure 60).

At 0.79 GW/cm², the soliton diameter is approximatively of 50 μm (at 1/e²), again very similar to the single soliton observed in chapter III.

The soliton starts disappearing at a pump intensity higher than 1 GW/cm² (Figure 60-(a)). Solitons generation seems to not obey to random instabilities but more precisely generated on a local high intensity where all the waves are superimposed. Their appearance and disappearance seem also driven by the same kind of mechanism discussed before.

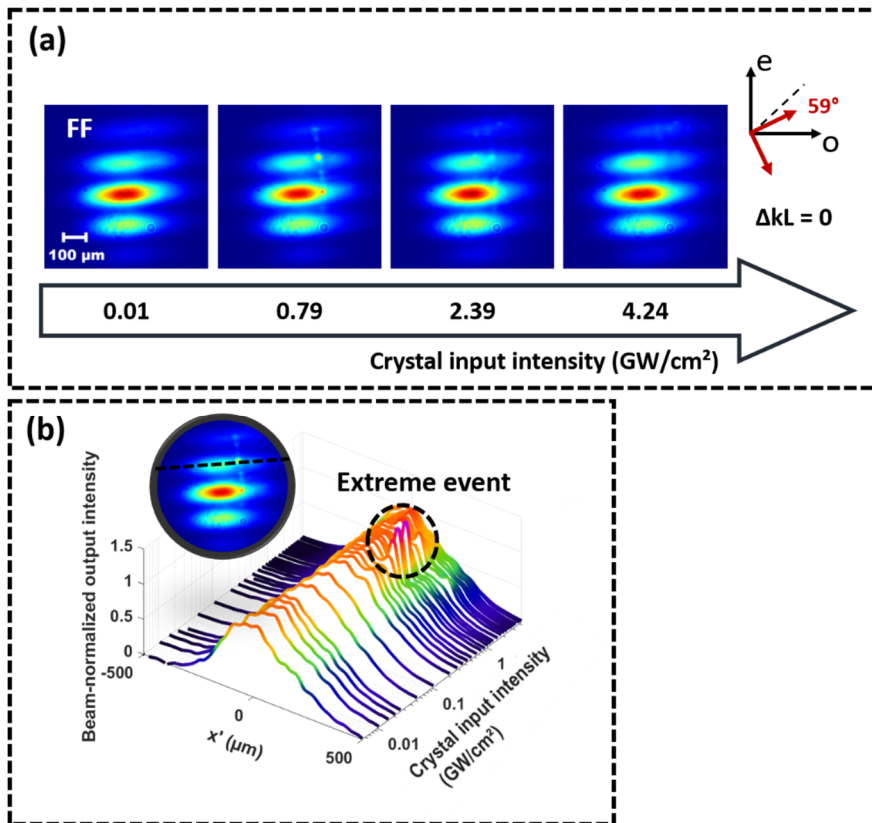


Figure 60: Solitons evolution, on a modulated pump, function of the pump intensity. **(a)**-FF beams images. **(b)**- Output profiles of the FF beam (I cut the lobe with the highest contrast between the pump and the soliton, see round inset). Phase matching conditions and linear input SOP = 59°.

In Figure 61, I compare some sample cases of input conditions leading to different numbers of soliton. Figure 61-(a) is for a SOP of 45° and at phase matching conditions, the waveform is then periodical along one transverse axis and composed of four spots. The balance between the input pump components (one orientated on e axis, the other on o axis) leads to two solitons on each local maxima of intensity.

For a SOP of 59° and also for exact phase matching conditions (Figure 61-(b)), only two spots appear. This observation follows then the same logic of the previous one and only one soliton is generated on each local maxima of intensity.

The process evolves with notable differences when the SOP is of 59° and for a high phase mismatch (Figure 61-(c)). In this case, solitons are generated along the two transverse axes and composed of three spots. One for the less energetic fringe and three for the higher one.

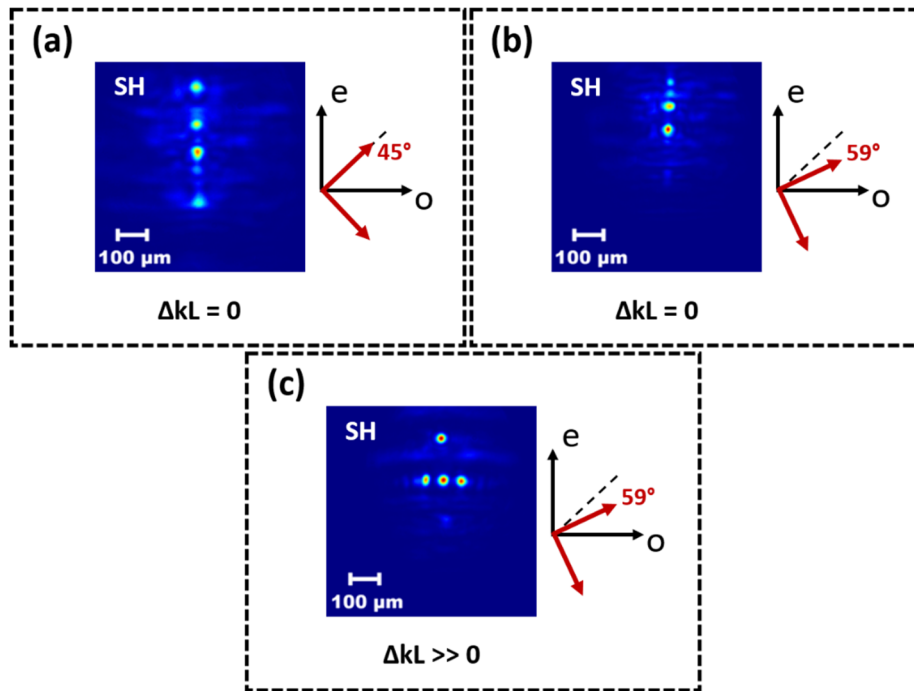


Figure 61: Solitons at the SH for a pump intensity of 0.53 GW/cm². **(a)**-Phase matching and linear input SOP = 45°. **(b)**-Phase matching and linear input SOP = 59°. **(c)**-High positive phase mismatch and linear input SOP = 59°.

V.3. Discussion

By using properly chosen conditions, I tried to demonstrate that the appearance of solitons is not exclusively guided by random instabilities, but could be induced by shaping the initial beam intensity and by considering the spatial walk-off, which may shift the soliton location.

Additionally, the appearance of a soliton can create spatial modulations mainly on the SH wave, forcing additional trapped beams to appear at the exact position where the maxima of modulation are obtained. In other words, we could talk about 2D deterministic MI driven by the soliton creation. First results on that behavior were published in 1997 by A. Fuerst *et al.*[4].

It is also evident that the best conditions for solitons generation are in cascading regime and with unbalanced intensities between e and o axes.

Conclusion – Chapter V

In this chapter, I demonstrate that 2D multiple solitons may appear with a determinist arrangement. In each case, the initial conditions, i. e. the phase mismatch and the polarization orientation, play a significant role.

The solitons location seems directly related to the modulation introduced on the SH by the first event appearing in the transverse beam profile. That first event is no more induced by random MI but appears on a maximum of intensity, in the area where the three waves can have a non-zero overlap.

It is also evident that the use of a modulated initial beam imposes the area where the solitons have to appear. The use of large beam, with a step intensity repartition, in a nonlinear crystal without spatial walk-off, would give different solutions and new nonlinear dynamics.

However, whatever the number of solitonic events generated in my experiments, they all disappear systematically for a strong enough pump power. Competition with temporal instabilities seems to be the main cause of that collapsing process.

Bibliography – Chapter V

- [1] Torruellas, W. E., Assanto, G., Lawrence, B. L., Fuerst, R. A., & Stegeman, G. I. (1996). All-optical switching by spatial walkoff compensation and solitary-wave locking. *Applied physics letters*, 68(11), 1449-1451.
- [2] Torruellas, W. E., Wang, Z., Hagan, D. J., VanStryland, E. W., Stegeman, G. I., Torner, L., & Menyuk, C. R. (1995). Observation of two-dimensional spatial solitary waves in a quadratic medium. *Physical review letters*, 74(25), 5036.
- [3] Carrasco, S., Polyakov, S., Kim, H., Jankovic, L., Stegeman, G. I., Torres, J. P., ... & Eger, D. (2003). Observation of multiple soliton generation mediated by amplification of asymmetries. *Physical Review E*, 67(4), 046616.
- [4] Fuerst, R. A., Baboiu, D. M., Lawrence, B., Torruellas, W. E., Stegeman, G. I., Trillo, S., & Wabnitz, S. (1997). Spatial modulational instability and multisolitonlike generation in a quadratically nonlinear optical medium. *Physical review letters*, 78(14), 2756.

Chapter VI. Applications

VI.1. Ultrafast pulse reshaping by using the 2D transient soliton

It is well known that any nonlinear dynamics appearing in the spatial or in the temporal domain can be used for nonlinear reshaping of high intensity waves. In my case, and even if the concept is not completely new, I realized a temporal reshaping on a modulated pulse showing a large pedestal. Because of its nonlinear nature, the spatial soliton can be exploited to make an ultrafast saturable absorber (see references [1] and [2]), which open the way to realize an ultrafast temporal pulse reshaping [3] [4] [5] [6].

With a standard soliton, the nonlinear transmission, obtained through a spatial filter around the soliton, exhibits a sigmoid profile. By using the ephemeral soliton instead, the transmission diminishes above a pump intensity threshold (super-Gaussian transmission curve), bringing novelties for temporal filtering in a given range of intensity, and the possibility to affect, not only the low energetic part of the temporal pulse, but also the highest energy pulse components.

VI.1.1. Emulation of the temporal filtering

In order to predict the beam reshaping efficiency by using my KTP crystal, I simulated the transmission of a Gaussian temporal pulse, followed by another smaller pulse (5 times smaller than the first Gaussian pulse). This second pulse, in my application idea, was playing the role of a parasite beam I wanted to remove.

In order to plot the nonlinear transmission, I used all the experimental setup that I developed all along my work (see Figure 27 on paragraph III.1.1). I used different camera images of the FF beam in function of the pump intensity, and by calculating the energy transmitted in a small part of the image, where the soliton appears, I deduced a simplified transmission curve, fitting the transmissions data. The spatial filtering that I introduced had $40\ \mu\text{m}$ of diameter at $1/e^2$.

In Figure 62-(a), the transmission curve is ascending between 0 and $0.2\ \text{GW}/\text{cm}^2$ i. e. the intensity span for which the soliton appears and grows. The transmission curve is constant between $0.2\ \text{GW}/\text{cm}^2$ and $0.8\ \text{GW}/\text{cm}^2$, i. e. those intensities for which the soliton is stable. For intensities higher than $0.8\ \text{GW}/\text{cm}^2$, the transmission in the filtered area reduces until the

pump reaches 1.3 GW/cm^2 , where the soliton disappears and the transmission is then constant. For this reason, the intensity of the temporal pulse must be lower than 0.8 GW/cm^2 to obtain a pulse reshaping.

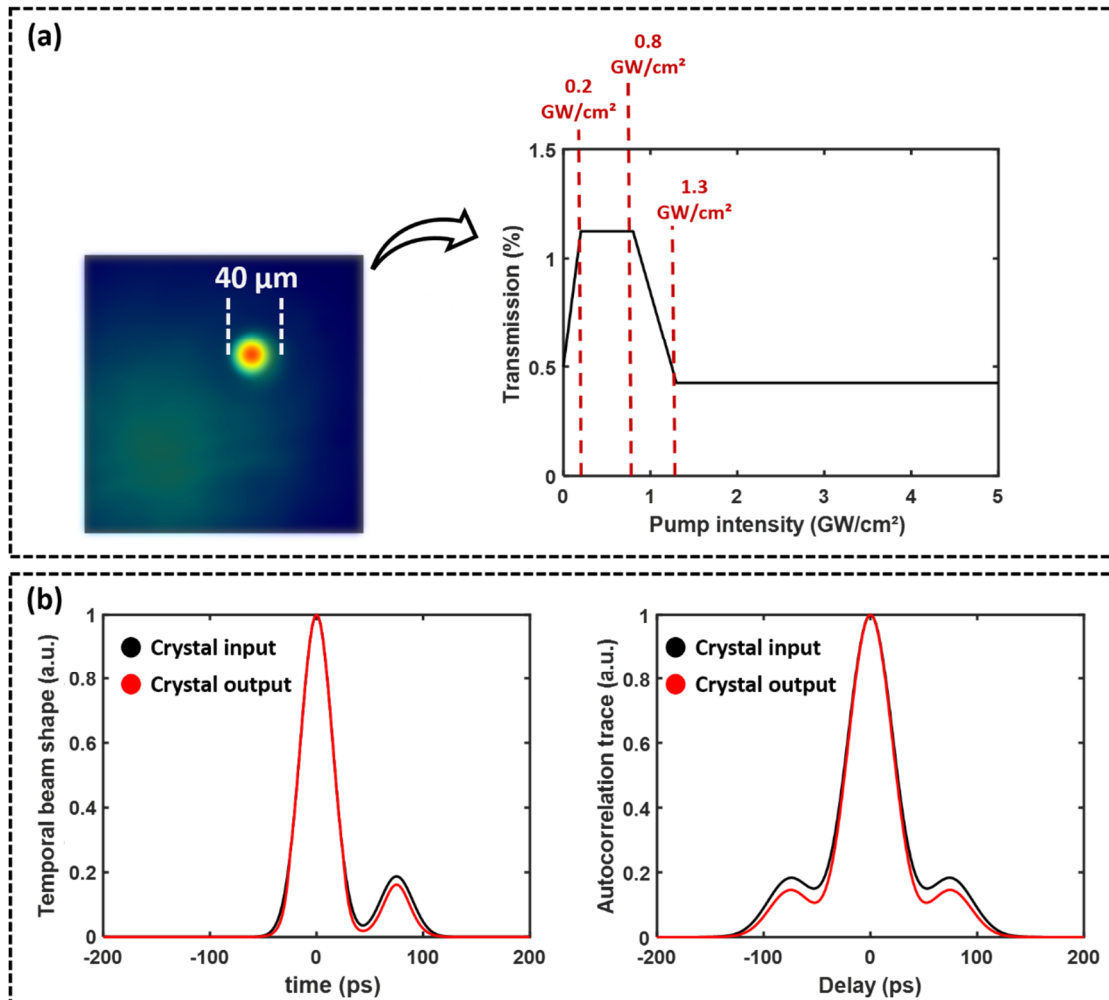


Figure 62: **(a)**-Nonlinear transmission curve obtained by filtering the self-trapped beam with a hole of $40 \mu\text{m}$ of diameter. **(b)**-(Left curve) temporal pulse profiles before and after the temporal filtering; (Right curve) corresponding autocorrelation traces of the two pulses. The figures are obtained at phase matching conditions, with a linear input SOP of 47° .

VI.1.2. Pulse reshaping setup

I reproduced this temporal waveform (one main pulse and one smaller parasite pulse) in my experimental bench by using a module developed by Tigran Mansuryan (see Figure 63 for the schematic). The purpose of this module is to separate the initial pulse in two, by using a Michelson interferometer realized with a polarizer cube. Each pulse propagates through different optical paths before recombination. The control of the power ratio between the two pulses is made possible by a first half-wave plate **(A)** and two quarter plates placed on one arm of the interferometer **(B)**. A delay line controls the time separating the two pulses **(B)**. A single polarization for the two pulses is then selected by means of a last polarizer and a half wave plate **(C)** before coupling in the nonlinear crystal.

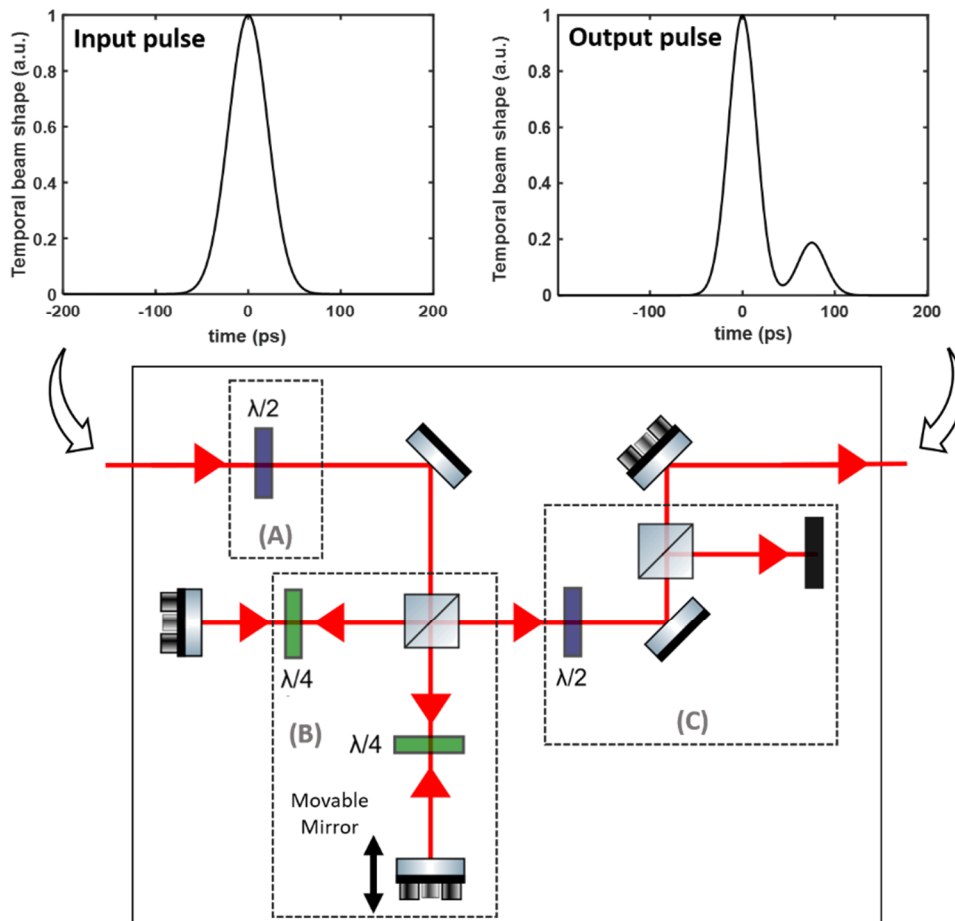


Figure 63: Experimental module used to shape the incident pulse.

VI.1.3. Pulse reshaping observations

I injected the distorted pulse into the nonlinear crystal with an intensity of 0.7 GW/cm^2 (i. e. a safe intensity zone to get a stable event, before the soliton energy starts to diminish). After a spatial filtering of the soliton image with an iris, I observed the reduction of the parasitic second pulse on the autocorrelation trace. The size of the second pulse is reduced by 4 during the reshaping process (Figure 64). The main pulse width is also reduced, from 43 ps to 27 ps (FWHM) on the autocorrelation trace.

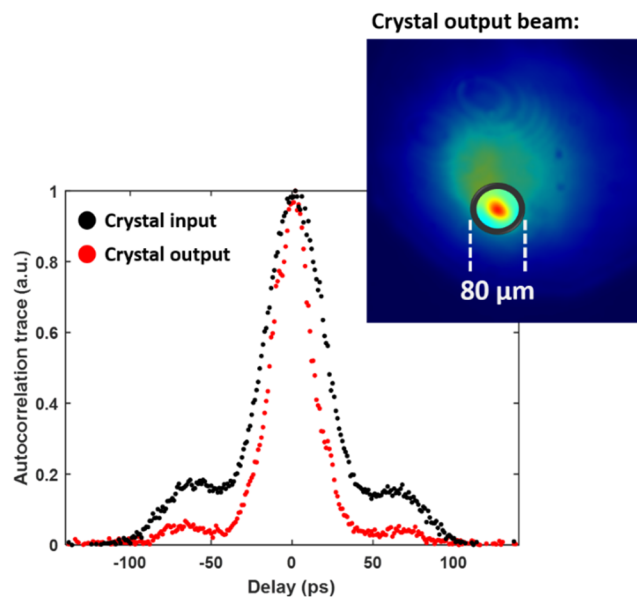


Figure 64: Pulse reshaping observation, by spatially filtering the soliton with a hole (diameter at $1/e^2 = 80 \mu\text{m}$). Calculated pulse profiles from the recorded autocorrelation traces. The pump intensity is equal to 0.7 GW/cm^2 , the linear input SOP is 53° and the crystal is at phase matching conditions.

I report the evolution of the pulse reshaping versus the input pump intensity in Figure 65-(a). For an input intensity of 0.7 GW/cm^2 , at the phase matching position, the amplitude ratio between the main and the parasitic pulse passes from 0.2 to 0.05. The reshaping affects also the pulse duration: the central pulse is also reduced by a factor of 1.6 in width (autocorrelation trace width-FWHM). At 1.5 GW/cm^2 the parasitic pulse reduction is quasi similar to what I obtained at 0.7 GW/cm^2 . The main difference is visible on the central pulse duration, which is reduced by factor 3, and some distortion occurs on the pulse pedestal. For a higher input intensity, a strong pulse breaking effect is observed and the temporal reshaping is no more observable.

It is important to note that even if we can design a quasi super-Gaussian nonlinear transparent curve by using the total spatial evolution of the trapped beam, the spatio-temporal nature of the phenomenon do not allow to exploit the transmission curve beyond 0.8 GW/cm^2 . Indeed, for high intensity values, the temporal pulse breaking starts being the dominant process that modulates the pulse and suppresses the trapped beam existence.

Similar behavior is obtained versus ΔkL (see Figure 65-(b)). The optimum temporal filtering is obtained at exact phase matching with a pump intensity of 0.7 GW/cm^2 while for negative and positive ΔkL , the reshaping is less efficient.

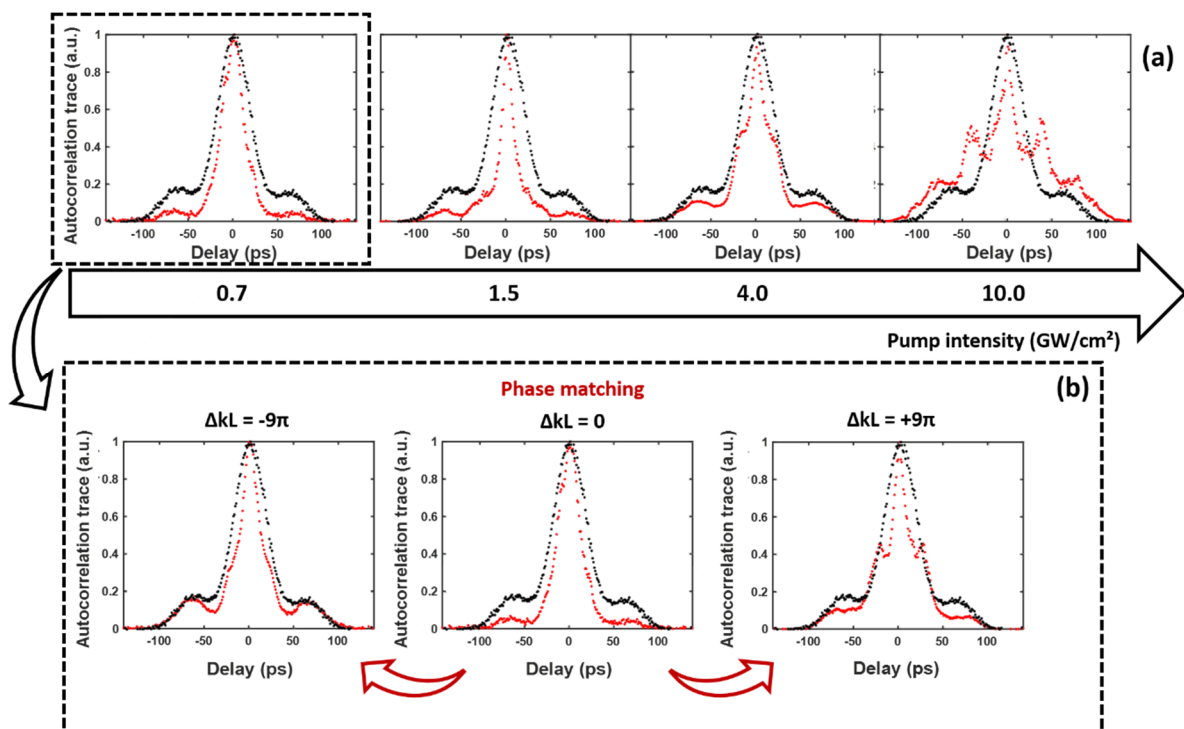


Figure 65: Analyze of the pulse reshaping effect for different input pump intensities and phase mismatch conditions. The input linear SOP is 53° . **Black curves:** input pulses, **Red curves:** output pulses. **(a)**-Pulse reshaping evolution, versus the pump intensity and at phase matching conditions. **(b)**-Pulse reshaping evolution, versus the phase mismatch ($\Delta kL = +9\pi$ and $\Delta kL = -9\pi$) or phase matching conditions ($\Delta kL = 0$) for an input pump intensity of 0.7 GW/cm^2 .

Ultrafast pulse reshaping was not the only useful application of the works I realized in various quadratic crystals. We will see on the following lines another application for improvement of vibrational microscopy setup.

VI.2. PPLN generated supercontinuum for a delay line free M-CARS

VI.2.1. Context

Coherent Anti-Stokes Raman Scattering or CARS microscopy has advanced our ability to identify the structure of matter, especially biological samples at the molecular level. It allows the analyses of a sample without labeling, using laser source to excite molecules through its vibrational modes, and then collecting the anti-Stokes Raman scattering response of the analyzed sample (see paragraph I.3.2.1 for more information on Raman effect).

In a 1974 study, R.F. Begley *et al.* [9] demonstrated the advantages of the CARS process, compared to the incoherent Raman spectroscopy, illustrated by a 10^5 improvement of conversion efficiency as well as a spatial and spectral discrimination and a low light average power without the use of markers. Hence, a first implementation of the CARS process in microscopy was made by Duncan *et al.* 8 years later [10].

This development made CARS a widespread technique for vibrational imaging of biological samples without labels, as the emitted signal is shifted, compared to the Pump and Stokes waves, towards wavelengths between 750 nm - 997 nm, thus avoiding superposition with an auto-fluorescent signal [11] [12]. In addition, CARS has been used for the analysis of lipids in cells by looking at the signature of the CH₂ vibration in particular to identify cancer cells [11] [13] [14].

The *Multiplex Coherent anti-Stokes Raman Scattering* (M-CARS) is a recent spectroscopy technique based on the use of a very wide spectral band [15] to excite simultaneously all the vibrational modes of a sample. The many advantages of the M-CARS make it a reference technique in vibrational spectroscopy for the study of chemical and biological samples. Tiffany Guerenne-Del Ben used M-CARS microscopy to analyze the content of lipid in cells, using the vibrational signature of methylene (CH₂) [16].

M-CARS microspectroscopy shows significant efficiency in the biomedical field as it is selective, non-destructive and allows to probe simultaneously all the vibrational modes. Developing a simple imaging method combining all the modalities and allowing the collection of a maximum of molecular information is a technological and instrumental challenge at present days.

The technique is based on the use of two excitation waves: a first one, monochromatic and of high power, which will play the role of the pump wave, and a second one, covering a wide spectral range, which is the Stokes wave. Unlike the classical CARS spectra, which are usually defined on a narrower spectral range, the M-CARS exhibits a spectrum that can cover a spectral range of 4000 cm^{-1} . This allows the simultaneous analysis of several different anti-Stokes signals, where the use of tunable sources would be necessary for a classical CARS system.

The generation of supercontinuum was usually done through a Photonic-Crystal Fiber (PCF) by the joint effects of chromatic dispersion and nonlinearities including the Kerr and Raman effects (see ref. [17] [18] for more information). Moreover, in this configuration, the M-CARS requires placing a delay line in the path of the pump to synchronize it with the Stokes wave on the sample.

We present in this part of the thesis a new supercontinuum source that can be implemented in the M-CARS system without delay line, by using the supercontinuum generation at the output of a PPLN as a Stokes wave. This way, the pump and the Stokes waves are directly synchronized on the sample, after propagation in the quadratic nonlinear crystal. This method will be validated through the imaging of polystyrene beads and cellulose fibers.

The use of the M-CARS technique was the main biomedical application linked to my works on extreme spatial events and spectral broadening generation in quadratic crystals. The following works (based on the supercontinuum generation I studied in the PPLN crystal during my thesis) are part of those realized by Sahar Wehbi in the context of her thesis. These fructuous works, in which I am co-author, have been published in reference [19].

VI.2.2. Setup

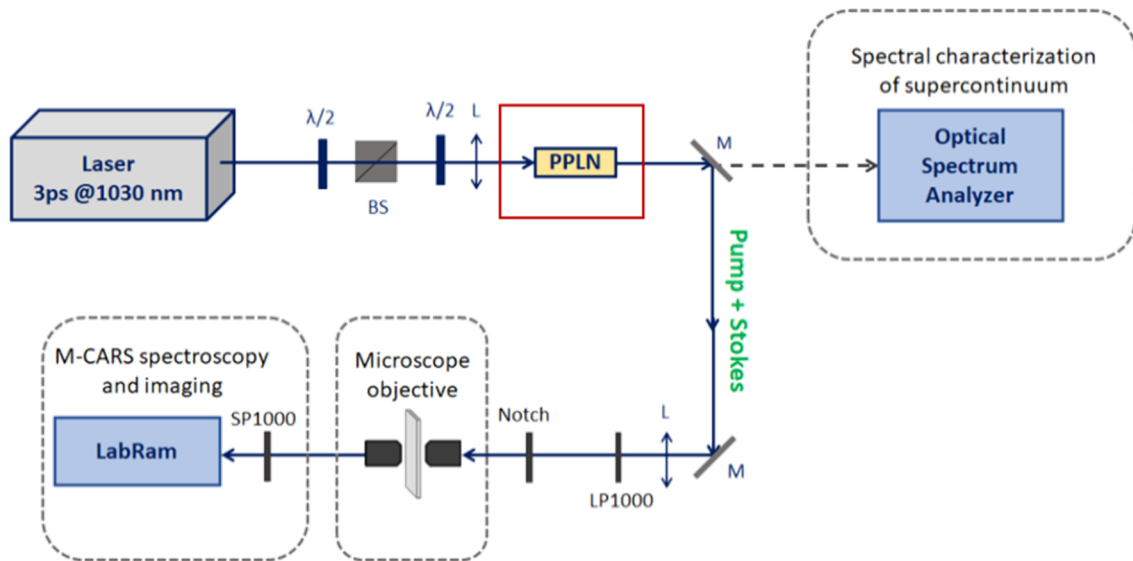


Figure 66: M-CARS experimental setup, with a PPLN and without delay line, realized by S. Wehbi *et al.* at XLIM laboratory [19]. $\lambda/2$: half-wave plate, **BS**: polarizing beam splitter, **L**: lens, **M**: mirror, **SP1000**: short-pass filter (<1000 nm), **LP1000**: long-pass filter (>1000 nm).

Figure 66 represents the experimental setup realized by Sahar Wehbi and Tigran Mansuryan, for the generation of the supercontinuum in order to perform the M-CARS measurements.

A 20 mm long PPLN crystal is pumped by a laser with a wavelength of 1030 nm, 3 ps of pulse duration, and repetition rate of 30 kHz.

Then, two half-wave plates and a polarized beam splitter cube are placed before the crystal to control the energy and polarization of the optical beam.

The optical beam is then focused in the PPLN crystal, with a linear input SOP optimized for a broadband spectrum generation in the PPLN. The Pump and Stokes waves are coupled into the crystal, which is in a phase mismatch configuration (its temperature is of 100 °C), in the cascading regime. The short length of the crystal (20 mm) allows to limit the dispersion and to keep these two waves temporally synchronized at the output of the crystal.

The generated PPLN supercontinuum is separated along two optical paths. The first path is used to analyze the PPLN supercontinuum spectrum by an Ando spectrum analyzer. The second path is used to send the collimated beam through different filters to the sample.

To perform M-CARS measurements in the picosecond regime, the generated supercontinuum is collimated and then delivered to a 1000 nm long-pass filter that eliminates the visible part of the supercontinuum to avoid its superposition with the emitted Anti-Stokes wave (between 750 nm and 997 nm).

The slightly tilted Notch 1064 nm is used to reduce the spectral width of the pump and then to improve the spectral resolution of M-CARS measurements.

Then, the beam is focused on the sample with a 60x microscope objective. The emitted M-CARS signal is collected by another 60x microscope objective.

As the emitted Anti-Stokes waves of interest (between -3200 cm^{-1} and -500 cm^{-1}) corresponds to wavelengths between 729 nm and 997 nm, a 1000 nm short-pass is placed to filter the signal before its transmission to the spectrometer LabRam.

With a broadband NIR Stokes wave generated by the supercontinuum out of the PPLN, filtered by the high-pass filter (see Figure 67), images of polystyrene beads (20 μm -diameter) and cellulose fibers were realized around the identified respective vibrational modes.

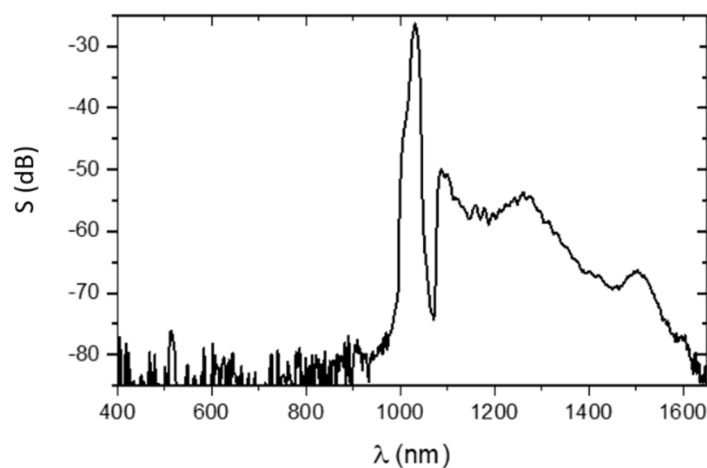


Figure 67: Spectrum of the Stokes beam (PPLN supercontinuum + long-pass filter at 1000 nm) before injection in the sample.

VI.2.3. Delay line free M-CARS microscopy: experimental imaging

VI.2.3.1. M-CARS image of polystyrene beads

First, the polystyrene Raman spectrum was measured with the M-CARS setup, launching an injected optical power of 1.5 mW to avoid burning the bead. For that power, the beam at the output of the PPLN is Gaussian. Clear images of the polystyrene beads were observed, by using a CCD camera coupled to the spectrometer; a vibrational signal was collected at the output of the sample, from which the M-CARS spectral image was constructed. Figure 68-(a) and Figure 68-(b) show respectively the white light image of polystyrene beads and the corresponding M-CARS image.

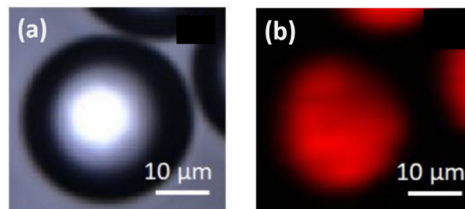


Figure 68: M-CARS images of polystyrene beads by S. Wehbi *et al.* [19]. **(a)**-Bright field image. **(b)**-M-CARS image for a Raman shift of 3055 cm^{-1} , extracted of M-CARS data.

VI.2.3.2. M-CARS image of cellulose fibers

M-CARS microscopy was performed on cellulose fibers, present in paper sheet. Figure 69-(a) and Figure 69-(b) exhibit respectively the white light and M-CARS images of the cellulose fiber present in the paper sheet. To identify the vibrational mode in the cellulose fibers, measurements established by Raman spectroscopy were found in a paper written by Alves *et al.* in 2016 [20].

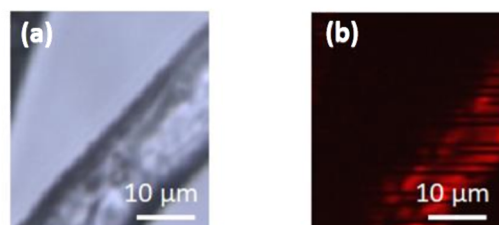


Figure 69: M-CARS images of cellulose fibers by S. Wehbi *et al.* [19]. **(a)**-Bright field image. **(b)**-M-CARS image for a Raman shift of 2896 cm^{-1} , extracted of M-CARS data.

Conclusion – Chapter VI

All-optical ultrafast temporal reshaping: I have realized a practical implementation with an ultrafast temporal reshaping by using the ephemeral soliton in type II KTP crystal. The nonlinear behavior obtained in the spatial domain is different than the one obtained for a simple soliton beam since the event disappearance does not affect so much the spatial shape of the FF beam. The transmission curve that I obtained with the spatial evolution of the trapped beam exhibits a super Gaussian profile instead of the sigmoidal evolution seen in the case of a standard soliton [6]. I succeeded to demonstrate a temporal reshaping of a noisy pulse composed of a main one and a parasitic second pulse. Reduction of more than 75% has been obtained on the second pulse. However, by changing the initial conditions, I clearly identified the limitation of the system, which are due to the temporal pulse breaking effects for higher intensities. In these conditions, my temporal reshaping possesses no more new characteristics than the temporal filtering already published in several papers by using quadratic solitons generation [4] [6]. However, such ingenious temporal remodeling could find applications in telecommunication engineering field, where the debit or rate of optical pulses on a short time span is very critical for high data transfers [7] [8].

PPLN supercontinuum for a delay line free M-CARS: We showed here that a delay line free M-CARS system could be implemented by replacing the PCF by a PPLN crystal for a broadband Stokes wave generation. Due to their short length, crystals allow the pump wave and the Stokes wave to be directly synchronized at its output and then on the sample to analyze. The spectral profile obtained is related to the optical non-linearity in the medium. Indeed, the spectrum out of the PPLN crystal is highly tunable by the phase matching conditions depending on its temperature (see chapter IV for more information). A broadband supercontinuum was obtained for a PPLN in large phase mismatch conditions (cascading regime). The efficiency of this M-CARS microscope was validated through the imaging of polystyrene beads and cellulose fibers around the identified vibration modes.

The results I show in this applicative chapter prove the efficiency of quadratic crystals to realize M-CARS microscopy for biomedical applications, as well as ultrafast pulse reshapers, without the need of electronical devices, for telecom applications.

Bibliography – Chapter VI

- [1] Haus, H. A. (1975). Theory of mode locking with a fast saturable absorber. *Journal of Applied Physics*, 46(7), 3049-3058.
- [2] Bao, Q., Zhang, H., Wang, Y., Ni, Z., Yan, Y., Shen, Z. X., ... & Tang, D. Y. (2009). Atomic-layer graphene as a saturable absorber for ultrafast pulsed lasers. *Advanced Functional Materials*, 19(19), 3077-3083.
- [3] Fsaifes, I., Cordette, S., Tonello, A., Couderc, V., Lepers, C., Ware, C., ... & Buy-Lesvigne, C. (2010). Nonlinear pulse reshaping with highly birefringent photonic crystal fiber for OCDMA receivers. *IEEE Photonics Technology Letters*, 22(18), 1367-1369.
- [4] Simos, C., Couderc, V., & Barthélémy, A. (2002). Temporal reshaping of optical pulses using quadratic spatial soliton generation and spatial filtering. *IEEE Photonics Technology Letters*, 14(5), 636-638.
- [5] Dautre, F., Couderc, V., & Pagnoux, D. (2009, June). Laser pulse reshaping by means of nonlinear effects in a low birefringence optical fiber. In *The European Conference on Lasers and Electro-Optics* (p. CD6_4). Optical Society of America.
- [6] PIOGER, P. H. (2004). Thèse en cotutelle de thèse (Doctoral dissertation, Università di Brescia).
- [7] Parmigiani, F., Petropoulos, P., Ibsen, M., & Richardson, D. J. (2006). All-optical pulse reshaping and retiming systems incorporating pulse shaping fiber Bragg grating. *Journal of Lightwave Technology*, 24(1), 357.
- [8] Yu, H. Y., Mahgerefteh, D., Cho, P. S., & Goldhar, J. (1999). Improved transmission of chirped signals from semiconductor optical devices by pulse reshaping using a fiber Bragg grating filter. *Journal of lightwave technology*, 17(5), 898.
- [9] Begley, R. F., Harvey, A. B., & Byer, R. L. (1974). Coherent anti-Stokes Raman spectroscopy. *Applied Physics Letters*, 25(7), 387-390.
- [10] Duncan, M. D., Reintjes, J., & Manuccia, T. J. (1982). Scanning coherent anti-Stokes Raman microscope. *Optics letters*, 7(8), 350-352.
- [11] Rodriguez, L. G., Lockett, S. J., & Holtom, G. R. (2006). Coherent anti-stokes Raman scattering microscopy: A biological review. *Cytometry Part A: The Journal of the International Society for Analytical Cytology*, 69(8), 779-791.
- [12] Brustlein, S., Ferrand, P., Walther, N., Brasselet, S., Rigneault, H., Billaudeau, C., & Marguet, D. D. (2011). Optical parametric oscillator-based light source for coherent Raman scattering microscopy: practical overview. *Journal of biomedical optics*, 16(2), 021106.
- [13] Cheng, J. X., Jia, Y. K., Zheng, G., & Xie, X. S. (2002). Laser-scanning coherent anti-Stokes Raman scattering microscopy and applications to cell biology. *Biophysical journal*, 83(1), 502-509.
- [14] Mitra, R., Chao, O., Urasaki, Y., Goodman, O. B., & Le, T. T. (2012). Detection of lipid-rich prostate circulating tumour cells with coherent anti-Stokes Raman scattering microscopy. *BMC cancer*, 12(1), 1-9.

- [15]Okuno, M., Kano, H., Leproux, P., Couderc, V., & Hamaguchi, H. O. (2008). Ultrabroadband multiplex CARS microspectroscopy and imaging using a subnanosecond supercontinuum light source in the deep near infrared. *Optics letters*, 33(9), 923-925.
- [16]Guereenne-Del Ben, T., Rajaofara, Z., Couderc, V., Sol, V., Kano, H., Leproux, P., & Petit, J. M. (2019). Multiplex coherent anti-Stokes Raman scattering highlights state of chromatin condensation in CH region. *Scientific reports*, 9(1), 1-10.
- [17]Agrawal, G. P. (2000). Nonlinear fiber optics. In *Nonlinear Science at the Dawn of the 21st Century* (pp. 195-211). Springer, Berlin, Heidelberg.
- [18]Singh, S., & Singh, N. (2007). Nonlinear effects in optical fibers: origin, management and applications. *progress in Electromagnetics Research*, 73, 249-275.
- [19]Wehbi, S., Mansuryan, T., Jauberteau, R., Tonello, A., & Krupa, K. Versatile supercontinuum generation by using $\chi(2)$ and $\chi(3)$ nonlinearities in PPLN crystal for direct multiplex CARS measurement. In *Proc. of SPIE Vol (Vol. 11770, pp. 1177017-1)*.
- [20]Alves, A. P. P., de Oliveira, L. P., Castro, A. A., Neumann, R., de Oliveira, L. F., Edwards, H. G., & Sant'Ana, A. C. (2016). The structure of different cellulosic fibres characterized by Raman spectroscopy. *Vibrational Spectroscopy*, 86, 324-330.

General conclusion

In **chapter I**, I introduced the concept of optical soliton from their first observation to their last evolution in many domains of physics. I described several soliton families and their possible interactions. In a second step, I introduced the NLSE and I presented the MI process on which phenomenon growing on these instabilities can be analytically described: this way, I described the Peregrine soliton, the Akhmediev and the Kuznetsov-Ma breathers, which are known to exist only in one transverse dimension. Such solutions are used to understand the rogue waves, appearing and collapsing without leaving a trace. I finish this chapter by describing the special case of silica fibers and its dominant Kerr and Raman nonlinearities, leading to optical solitons formation.

In **chapter II**, I introduced the quadratic nonlinearity with the three-wave mixing process and presented several nonlinear crystals based on different phase matching processes as type I, type II and type 0. Thereafter, I made a review on quadratic solitons, also called bicolor solitons, on specific solitonic interactions, and on quadratic MI, widely observed and reported along the last 30 years.

In **chapter III**, I introduced my works on the quadratic soliton propagation, generated in particular conditions, i. e. by using a non-diffractive Gaussian beam launched in bulk KTP and PPLN. The initial conditions that I used were far from the ones used in already published works where the Fresnel length of the input beam is 2 to 6 times shorter than the crystal length. In my conditions, I observed a 2D ephemeral spatial soliton, which appeared and disappeared while increasing monotonically the input intensity. Its behavior mimicked a transient 2D rogue event, as the ones observed in water waves. I studied this nonlinear process with respect to all the parameters involved in the propagation i. e. the input pump intensity, the phase matching condition and the polarization orientation. I underlined that this soliton collapsed because of complex spatiotemporal instabilities, taking place at a high input intensity.

In **chapter IV**, I also investigated on a nonlinear speckle shape printed on the SH beam by the quadratic nonlinearity and the periodic energy exchange between the FF and SH beams. Thus, I concluded this chapter by demonstrating that the SH complex speckle formation, generated by the temporal pulse breaking, could be self-cleaned in a Gaussian transverse beam and at the same time it could extend the spectral width of the two waves involved in the process.

In **chapter V**, I presented a special case: the multiple generation of quadratic solitons. I demonstrated that, under my experimental conditions, the localization of the solitons was due to the highest intensities in the transverse beam with a strong impact of the spatial walk-off. I also underlined how multiple solitons could be obtained because of the SH modulation in the cascading process.

Finally, in **chapter VI**, I used the quadratic soliton generation to realize an all-optical ultrafast temporal reshaping of picosecond pulses. This principle of temporal reshaping is based on the propagation of a self-trapped beam associated with its spatial filtering at the end of the propagation. A reshaping and compression of a noisy pulse has been shown in conditions allowing the propagation of the soliton. Reshaping was optimal for an illumination value slightly lower than the value for which the soliton starts to disappear.

Today, the main limitation to the use of quadratic spatial solitons for ultrafast beam shaping operations, as well as for supercontinuum generation, remains the power densities required for their excitation, despite the existing configurations (PPLN plane guide for example). The use of more efficient nonlinear materials would allow a new interest for spatial solitons.

However, the results of spectral broadening I obtained during my thesis were used by Sahar Wehbi to create a nonlinear delay line free M-CARS microscope.

Thank you Alexander Franzen for the Inkscape library, that I used in order to draw the optical setups in this thesis report.

Publications

Publications in Journals and Proceeding papers

Niang, A., Couderc, V., Tonello, A., Krupa, K., Addisu, M., **Jauberteau, R.**, ... & Wabnitz, S. (2019, May). Self-cleaning on a higher order mode in Ytterbium-doped multimode fiber with parabolic profile. In *2019 Conference on Lasers and Electro-Optics (CLEO)* (pp. 1-2). IEEE.

https://doi.org/10.1364/CLEO_SI.2019.STh4L.1

Jauberteau, R., Tonello, A., Baronio, F., Krupa, K., Mllot, G., Wetzel, B., ... & Couderc, V. (2020, May). Observation of 2D spatiotemporal rogue events in a quadratic nonlinear medium. In *CLEO: Science and Innovations* (pp. JTU2F-18). Optical Society of America.

https://doi.org/10.1364/CLEO_AT.2020.JTu2F.18

Jima, M. A., Deliancourt, E., **Jauberteau, R.**, Leventoux, Y., Niang, A., Krupa, K., ... & Couderc, V. (2021, May). Spatial Beam Evolution in Nonlinear Multimode Fibers. In *CLEO: Science and Innovations* (pp. SM1F-3). Optical Society of America.

https://doi.org/10.1364/CLEO_SI.2021.SM1F.3

Jauberteau, R., Wehbi, S., Mansuryan, T., Krupa, K., Baronio, F., Wetzel, B., ... & Couderc, V. (2021). Boosting and Taming Wave Breakup in Second Harmonic Generation. *Frontiers in Physics*, *9*, 106.

<https://doi.org/10.3389/fphy.2021.640025>

Wehbi, S., Mansuryan, T., **Jauberteau, R.**,... & Couderc, V. Versatile supercontinuum generation by using χ (2) and χ (3) nonlinearities in PPLN crystal for direct multiplex CARS measurement. In *Proc. of SPIE Vol* (Vol. 11770, pp. 1177017-1).

<https://doi.org/10.1117/12.2589155>

One article on the ephemeral soliton in the process of being reviewed:

Jauberteau, R., Wehbi, S., Mansuryan, T., Tonello, A., Baronio, F., Krupa, K., Wetzel, B., Wabnitz, S., & Couderc, V. (2021). Twin Spotlight Beam Generation in Quadratic Crystals.

Congresses Communications

June / 2019: *Waves Côte d'Azur*, Nice, France - Poster session.

July / 2019: *JNOG*, Paris, France – Speaker.

May / 2020: *CLEO US*, San Jose, California, USA - Poster session.

June / 2021: *CLEO EU*, Munich, Germany - Speaker.

Événements extrêmes dans les milieux quadratiques : application à l'imagerie non linéaire

Résumé : L'objectif de mes travaux était la réalisation d'un banc d'étude expérimental sur les propagations quadratiques pouvant mener à un piégeage mutuel (spatial et temporel) des faisceaux aux fréquences fondamentale et seconde harmonique. L'originalité de ces recherches a été de démontrer, pour la première fois, l'apparition et la disparition d'un ou de plusieurs événements extrêmes de type solitons spatiaux quadratiques 2D en fonction de l'élévation monotone de la puissance initiale. Ces phénomènes non linéaires spatiaux sont accompagnés d'un élargissement spectral ainsi que d'une compression temporelle suivie d'une détérioration de l'impulsion initiale. Deux applications ont été réalisées, l'une sur le remodelage temporel ultrarapide d'impulsions brèves, l'autre sur l'utilisation du spectre large pour démontrer une imagerie CARS Multiplex.

Mots-clés : non linéarité optique, mélange à trois ondes, solitons

Eventi estremi in mezzi quadratici: applicazione all'imaging non lineare

Riassunto : L'obiettivo del mio lavoro è stato quello di realizzare un banco di studio sperimentale sulle propagazioni quadratiche che possono portare all'intrappolamento reciproco (spaziale e temporale) di fasci a frequenze fondamentali e di seconda armonica. L'originalità di questa ricerca è stata quella di dimostrare, per la prima volta, la comparsa e la scomparsa di uno o più eventi estremi: a solitoni spaziali quadratici 2D, in funzione di un incremento della potenza iniziale. I fenomeni spaziali non lineari sono accompagnati da allargamento spettrale e compressione temporale e sono seguiti da un deterioramento dell'impulso. Sono state eseguite due applicazioni, una sul rimodellamento temporale a impulsi brevi ultraveloci, l'altra sull'uso dell'ampio spettro per dimostrare l'imaging CARS Multiplex.

Keywords: non linearità ottica, miscelazione a tre onde, solitoni

**Université de Limoges, CNRS, XLIM, UMR 7252, 123 avenue Albert Thomas – 87060
Limoges, France**

**Università degli studi di Brescia, Dipartimento di Ingegneria dell'Informazione, Technology
for Health, Via Branze 38 - 25123 Brescia, Italia**

